The Mixed Potential Integral Equation for New Multilayered Structures Including Conductive Sheets: Analytical and Numerical Techniques

THÈSE N^{O} 6093 (2014)

PRÉSENTÉE LE 24 FÉVRIER 2014
À LA FACULTÉ DES SCIENCES ET TECHNIQUES DE L'INGÉNIEUR
LABORATOIRE D'ÉLECTROMAGNÉTISME ET ACOUSTIQUE
PROGRAMME DOCTORAL EN GÉNIE ÉLECTRIQUE

ÉCOLE POLYTECHNIQUE FÉDÉRALE DE LAUSANNE

POUR L'OBTENTION DU GRADE DE DOCTEUR ÈS SCIENCES

PAR

Ioannis KOUFOGIANNIS

acceptée sur proposition du jury:

Prof. J.-Ph. Thiran, président du jury
Prof. J. R. Mosig, Dr M. Mattes, directeurs de thèse
Prof. A. Alvarez Melcón, rapporteur
Prof. Y. Hao, rapporteur
Prof. F. Rachidi-Haeri, rapporteur

ÉCOLE POLYTECHNIQUE
FÉDÉRALE DE LAUSANNE

Suisse
2014

> Αιέν αριστεύειν καί υπείροχον έμμεναι άλλων,
> μηδέ γένος πατέρων αισχυνέμεν.
>
> *(Homer, Iliad Z.208)*

Abstract

Multilayered structures that include very thin conductive sheets have recently been technologically available and are receiving increased scientific interest within the Electromagnetic (EM) community. These conductive sheets can either be very thin compared to the operating wavelength or even mono-atomically thick like in the case of graphene layers. In all the cases, its presence embedded within a multilayered structure represents a new EM challenge, since the standard computational EM solvers do not necessarily include these sheets in their definition of a stretched multilayered structure.

One of the most suitable techniques for the EM modeling of multilayered structures is the Integral Equation technique solved with Method of Moments (IE-MoM) and more specifically the Mixed Potential Integral Equation (MPIE) formulation due to the lower order singularities in the kernels of the resulting integrals. The cornerstone of any IE formulation are the multilayered Green Functions (GFs), which are traditionally derived in the dual or spectral domain and later transformed back, through Sommerfeld integrals, to the primary or spatial domain.

Within this thesis, a general algorithm for formulating the GFs in the spectral domain for arbitrary multilayered structures including conductive sheets is developed. The conductive sheets are efficiently taken into account as surface boundary conditions rather than as thin lossy layers. The proposed technique is able to handle sheets with either scalar or tensorial conductivity, the last one being the case when 2-D sheets like graphene are both electrically and magnetically biased. Exact analytical expressions for the spectral domain GFs for the EM fields and their vector and scalar potentials are obtained.

In order to transform the GFs back to the spatial domain, a novel numerical technique based on the Double Exponential (DE) quadrature rule is proposed. It is enhanced with an efficient error estimator and consequently the Sommerfeld integrals can be evaluated faster than with the reference methods and in an error controllable manner up to machine precision.

Finally, as an additional proof of the usefulness and numerical versatility of the DE algorithm, the thesis addresses also the numerical evaluation of the multidimensional reaction integrals that serve as entries in the MoM matrix. For this purpose, a multidimensional version of the DE quadrature rule is developed and optimized in order to increase the efficiency of this numerical integration. For the first time, results up to machine precision are provided within very competitive time frame for cases where the observation domains share common points with the source ones or are located at their close proximity.

Keywords: Computational Electromagnetics, Integral Equations, MPIE, multilayered structures, conductive sheets, graphene, Green functions, Sommerfeld integrals, Double Exponential quadrature rule, reaction integrals, Method of Moments, singular integrals.

Résumé

Les milieux stratifiés comprenants de très fines couches conductrices sont une technologie récente et émergente, qui présente un intérêt croissant pour les chercheurs en Electromagnétisme (EM). Les couches conductrices sont très fines devant les longueurs d'ondes considérées, jusqu'à devenir monoatomiques dans le cas du graphène. Leurs présence au sein des milieux stratifiés représente dès lors un nouveau défi en matière de programmation, car les outils de résolution de problèmes EM standards n'incluent pas forcément la définition de tels objets dans leurs bases de données respectives.

L'une des méthodes les plus adaptées pour la modélisation EM des milieux stratifiés est la résolution d'Equations Intégrales (IE) à l'aide de la Méthode des Moments (MoM); l'Equation Intégrale à Potentiels Mélangés (MPIE) est une formulation particulièrement utile, car elle aboutit à des intégrales dont les noyaux présentent des singularités d'ordre relativement faibles. La clef de voute de toutes les formulations IE reste les Fonctions de Green (GF), qui sont établies habituellement dans le domaine spectral (ou "dual") et ramenées via des intégrales de Sommerfeld dans le domaine spatial.

Tout au long de cette thèse, on développe un algorithme général pour formuler les GF dans le domaine spectral, pour un milieu stratifié quelconque et en présence de couches conductrices. Ces dernières sont prises en compte de manière efficace sous forme de conditions aux limites surfaciques, plutôt que d'être vues comme de fines couches résistives. Les méthodes proposées fonctionnent aussi bien pour des conductivités scalaires que pour des conductivités tensorielles, ce qui arrive par exemple dans le cas de feuilles de graphène polarisées par des champs électriques et magnétiques. Des expressions analytiques rigoureuses sont obtenues pour les champs EM dans le domaine fréquentiel, ainsi que pour les potentiels scalaires et vecteurs.

Afin de retourner dans le domaine spatial, une méthode d'intégration numérique récente dite de "l'Exponentielle Double (DE)" est proposée. Elle est améliorée à l'aide d'un estimateur d'erreur efficace, ce qui permet d'évaluer les intégrales de Sommerfeld plus rapidement qu'avec les méthodes usuelles, et ce avec une précision limitée seulement par celle de l'ordinateur employé.

Pour terminer, on démontre l'utilité et la polyvalence de cette méthode d'intégration en évaluant les intégrales de réaction multidimensionelles qui permettent de construire la matrice MoM; une version multidimensionelle de l'algorithme DE est développée et optimisée spécifiquement dans ce but. Pour la première fois, on est en mesure de donner des résultats aussi précis que l'ordinateur utilisé le permette, dans des temps compétitifs par rapport aux méthodes habituelles, à condition que les domaines d'observations restent dans un voisinage proche de celui des sources.

Mots-clefs: Méthodes numériques appliquées à l'électromagnétisme, Equations Intégrales, MPIE, milieux stratifiés, Feuilles conductrices, Graphène, Fonctions de Green, Intégrales de Sommerfeld, Exponentielle Double, Intégrales de Réaction, Méthodes des Moments, Intégrales singulières.

Kurzfassung

Mehrschichtige Strukturen mit dünnen, elektrisch leitenden Übergängen zwischen den Lagen haben ein riesiges Potential für elektromagnetische Anwendungen. Diese leitenden Grenzflächen sind sehr dünn im Vergleich zur Wellenlänge oder bestehen wie im Fall von Graphen nur aus einer einzigen Atomschicht. Die Flächen stellen deshalb eine Herausforderung in der Modellierung und Simulation derartiger Strukturen dar.

Eine der gebräuchlichsten Methoden zur Simulation dieser Strukturen sind Integralgleichungen, die mit Hilfe des Momentenverfahrens effizient gelöst werden können. Von besonderer Bedeutung sind dabei auf Skalar- und Vektorpotential basierende Integralgleichungen, da ihr Kern nur eine schwache Singularität aufweist. Die dabei involvierten Greenschen Funktionen können äußerst effektiv im Spektralbereich berechnet und durch ein Sommerfeldintegral in den Ursprungsbereich, d. h. Ortsraum zurücktransformiert werden.

Im Rahmen dieser Dissertation wurde ein vielseitig einsetzbarer Algorithmus zur Simulation besagter Strukturen entwickelt. Dabei werden die leitenden Grenzflächen als Randbedingungen und nicht als verlustbehaftete Schichten modelliert. Ihre Leitfähigkeit kann sowohl skalar als auch tensoriell sein, wobei letzterer Fall vor allem in Graphen-Anwendungen vorkommt. Greensche Funktionen für elektrisches und magnetisches Feld als auch Skalar- und Vektorpotential werden damit berechnet.

Für die Rücktransformation der Greenschen Funktionen in den Ortsbereich kommt eine neues numerisches Integrationsverfahren zur Anwendung, das sogenannte doppelte Exponentialverfahren* (DE-Verfahren). Das originale DE-Verfahren wurde um eine Fehlerabschätzung erweitert. Das erlaubt die numerische Berechnung von Integralen mit einem vorgegebenen Fehler. Damit können die auftretenden Sommerfeldintegrale im Vergleich zu anderen Methoden schneller und effektiver berechnet werden, während gleichzeitig ein bestimmter Fehler garantiert werden kann. Außerdem erlaubt das DE-Verfahren die numerische Berechnung von Integralen mit Maschinengenauigkeit.

Die numerische Auswertung von mehrdimensionalen Momentenintegralen (MoM-Integrale) mit Hilfe des DE-Verfahrens wurde ebenfalls untersucht und die DE-Quadratur für diesen Fall optimiert. Dadurch können MoM-Integrale auch in Fällen mit Maschinengenauigkeit berechnet werden, in denen Quell- und Beobachterbereich im Momentenverfahren sehr dicht beieinander liegen oder sogar gemeinsame Punkte haben. In diesen Fällen nämlich nehmen die höheren Ableitungen der zu integrierenden Funktionen sehr bzw. unendliche große Werte an, weshalb klassische Quadraturverfahren, wie z. B. Gauß-Legendre, nur eine begrenzte Genauigkeit erreichen können.

Keywords: Numerische Feldberechnungsverfahren, Integralgleichungen, MPIE, Mehrschichtige Strukturen, elektrisch leitenden Übergängen, Graphen, Greenschen Funktionen, Sommerfeldintegral, doppelte Exponentialverfahren, Momentenintegrale, Momentenintegrale, singuläre Integrale.

---

[*] engl. double exponential quadrature

Περίληψη

Πολυστρωματικές διατάξεις που περιλαμβάνουν πολύ λεπτά αγώγιμα στρώματα έχουν πρόσφατα γίνει τεχνολογικά διαθέσιμες προσελκύοντας το ενδιαφέρον των Ηλεκτρομαγνητικών εφαρμογών τους. Τα πάχος των αγώγιμων στρωμάτων μπορεί να είναι είτε πολύ μικρό - συγκρινόμενο με το μήκος κύματος της διεγειρόμενης ακτινοβολίας - είτε ακόμη και μονοατομικό όπως στην περίπτωση φύλλων γραφενίου. Σε κάθε περιπτώση, η παρουσία των αγώγιμων στρωμάτων στην πολυστρωματική δομή αποτελεί μια νέα πρόκληση μιας και η κλασική προσέγγιση της ηλεκτρομαγνητικής μοντελοποίησης των πολυστρωματικών διατάξεων δεν μπορεί να τα λάβει υπόψιν.

Μια από τις καταλληλότερες τεχνικές για την ηλεκτρομαγνητική μοντελοποίηση των πολυστρωματικών διατάξεων είναι οι ολοκληρωτικές εξισώσεις και συγκεκριμένα η μέθοδος των μικτών δυναμικών συνδυασμένη με τη μέθοδο των ροπών. Ακρογωνιαίος λίθος κάθε τεχνικής ολοκληρωτικών εξισώσεων είναι η συνάρτηση Green, η οποία είθισται να υπολογίζεται στο φασματικό πεδίο και να μετασχηματίζεται στο χωρικό πεδίο μέσω των ολοκληρωμάτων Sommerfeld.

Στα πλαίσια της παρούσας διατριβής αναπτύχθηκε ένας αλγόριθμος για τον προσδιορισμό των συναρτήσεων Green σε τυχαίες πολυστρωματικές διατάξεις με αγώγιμα φύλλα. Τα αγώγιμα φύλλα λαμβάνονται υπόψιν εφαρμόζοντας κατάλληλες οριακές συνθήκες και όχι σαν λεπτά διηλεκτρικά στρώματα με απώλειες. Η προτεινόμενη μέθοδος μπορεί να εφαρμοστεί σε αγώγιμα φύλλα τόσο βαθμωτής όσο και διανυσματικής αγωγιμότητας. Η τελευταία περίπτωση συναντάται όταν διδιάστατα αγώγιμα φύλλα όπως το γραφένιο υπόκεινται ταυτόχρονα σε ηλεκτρικές και μαγνητικές διεγέρσεις. Παρουσιάζονται αναλυτικές εκφράσεις των συναρτήσεων Green στο φασματικό πεδίο τόσο σε επίπεδο ηλεκτρομαγνητικών πεδίων όσο και σε επίπεδο μικτών δυναμικών.

Ο μετασχηματισμός των Green από το φασματικό πεδίο στο χωρικό γίνεται με μια πρωτότυπη αριθμητική μέθοδο η οποία βασίζεται σε ολοκληρωτικούς κανόνες διπλών εκθετικών*. Οι κανόνες αυτοί διανθίζονται με αποτελεσματικούς εκτιμητές αριθμητικών σφαλμάτων με αποτέλεσμα τα ολοκληρώματα Sommerfeld να μπορούν να υπολογιστούν γρηγορότερα από ό,τι με τις υπάρχουσες μεθόδους. Επιπλέον, οι υπολογισμοί γίνονται με έναν απόλυτα ελεγχόμενο τρόπο όσον αφορά την ακρίβεια επιτυγχάνοντας μέχρι και τη μέγιστη δυνατή ακρίβεια που μπορεί να μας προσφέρει η υπολογιστική μηχανή που χρησιμοποιούμε.

Τέλος, ο ολοκληρωτικός κανόνας των διπλών εκθετικών χρησιμοποιείται και στην αριθμητική ολοκλήρωση των πολυδιάστατων ολοκληρωμάτων αλληλεπίδρασης που αποτελούν στοιχεία του πίνακα της μεθόδου των ροπών. Για το σκοπό αυτό αναπτύχθηκε μια πολυδιάσταστη έκδοση του ολοκληρωτικού κανόνα και βελτιστοποιήθηκε ώστε να αυξηθεί η απόδοση των αριθμητικών υπολογισμών. Για πρώτη φορά γίνονται διαθέσιμα αποτελέσματα με τη μέγιστη δυνατή ακρίβεια για περιπτώσεις όπου τα χωρία πηγής και παρατήρησης εδράζονται πολύ κοντά το ένα στο άλλο.

Λέξεις κλειδιά: Αριθμητικές μέθοδοι για προβλήματα ηλεκτρομαγνητισμού, ολοκληρωτικές εξισώσεις, μικτά δυναμικά, πολυστρωματικά μέσα, αγώγιμα στρώματα, γραφένιο, συναρτήσεις Green, ολοκληρώματα Sommerfeld, ολοκληρωτικοί κανόνες διπλών εκθετικών, ολοκληρώματα αλληλεπίδρασης, μέθοδος των ροπών, ιδιάζοντα ολοκληρώματα.

---

* αγγλ. double exponential quadrature

Acknowledgements

First of all, my gratitude goes to my thesis advisor and co-advisor, Prof. Juan R. Mosig and Dr. Michael Mattes, respectively, for providing me with the opportunity to join the Laboratory of Electromagnetics and Acoustics (LEMA) at EPFL in order to pursue this Ph.D. work. Juan's scientific advices and guidance, the fruitful meetings with nice ideas and very positive altitude characterize these years. Michael's deep knowledge, his willingness to help and discuss anytime, his youth soul and mind under the grey hair form a personality that I am extremely glad to have met and collaborated with him.

I need also to acknowledge Prof. Alejandro Alvarez Melcón , Prof. Yang Hao, Prof. Fahrad Rachidi-Haeri and Prof. Jean-Philippe Thiran for being so kind to serve as members of my committee judging the current work and constructively commenting on it. Additionally, Prof. Anja Skrivervik, Jean-François Zürcher and Eulalia Durussel for always keeping an eye on me and being there in order to discuss and solve any issue rising throughout all these years at LEMA.

I am very thankful to Thanos Polimeridis who paved my way in LEMA's corridors and introduced me in the singular integration scientific community. He enlightened me through all the discussions and thoughts we shared. The very first one, though, that introduced me at EPFL was Prof. Jean-Pierre Hubaux. His kind invitation served as a strong personal motivation to commit myself at the École Polytechnique and I am grateful for this.

My involvement in industrial projects let me broaden my knowledge and experience further away than the campus of Ecublens. Many many thanks for this to Holger Karstensen, Kuno Wettstein and Nikolaus Fichtner from Huber+Suhner AG, Gerald Kress from ETHZ, David Raboso from ESA and Nik Chavannes, Pedro Crespo and Francisco Nunez from SPEAG AG.

Back to base, LEMA's excellence is not limited only in electromagnetics. It extends to its people who create a unique family atmosphere. With Francesco Merli, Edén Sorolla, Apostolos Sounas, Jovanche Trajkovikj and Sebastian Gomez-Diaz we shared great moments, personal thoughts, even unpleasant events forming a very strong and valuable friendship. Roberto Torres, Benji Fuchs, Sergio Lopez, Marco Letizia and Gabriele Rosati definitely belong to the excellent hard-core LEMA team that I met when I joined the lab. The LEMA's ladies, Joanna, Gabriela, Madda, Maria, Laleh and Ruzica and guys Vick, Marc, Erio, Rafal, Nuno, Pietro, Anton, Michele, Baptiste, Eduardo, Tomislav, Yiannis Jr., Fred and Julien thanks to all of you for the excellent time we spent these years!

I shouldn't forget commemorating on the Greek friends with whom we founded the Association des étudiants Grecs de Lausanne: Aristeidis, Loukia, Konstantinos and Matt with the encouragement of Dimitris Kiritsis. And of course all the other friends: Alex, Teo, Christian, Polydefkis, Pavlos, Manos, Eirina being a few of them, who are closely linked to my excellent vaudoises memories. Besides, Evi deserves a special note for standing next to me all these years.

Finally, I would like to acknowledge my brother Fragkiskos and give him my warmest wishes. He spent some time at EPFL before deciding to cross the Atlantic and find the adequate environment for his brilliant scientific mind and his multidisciplinary character at University of Pennsylvania.

All these, including the thesis itself, would have been impossible without my mother's strong dedication in raising us - who continues tireless to struggle in order to support us - and my father's charismatic personality and his unconditional love - who would have been definitely very proud if reading this manuscript. To them I dedicate this thesis!

Γιάννης

Table of Contents

1 Introduction **1**
- 1.1 Objectives 2
- 1.2 Outline 3

2 State of the Art **5**
- 2.1 Integral Equations in Multilayered Structures 7
- 2.2 Numerical Techniques for Sommerfeld Integrals 8
- 2.3 Numerical Techniques for Reaction Integrals 9

3 Potentials and Integral Equations: a Reminder **11**
- 3.1 Integral Equation approach 11
- 3.2 Vector and Scalar Potentials 12
- 3.3 Mixed Potential Integral Equation 14
  - 3.3.1 Method of Moments 14

4 EM Modeling of Multilayered Structures **17**
- 4.1 Maxwell Equations for Multilayered Structures 18
- 4.2 Spectral Domain Transformation & Sommerfeld Integrals 19
- 4.3 Spectral Domain Green Functions 20
  - 4.3.1 Electric and Magnetic Field Green Functions 21
  - 4.3.2 Electric and Magnetic Dipole Excitations 22
  - 4.3.3 Spectral Domain Vector and Scalar Potential Green Functions 23
  - 4.3.4 Propagator Matrix and Terminating Conditions 24
- 4.4 Multilayered Structures with Thin Conductive Interfaces 30
  - 4.4.1 Interface with scalar conductivity 31
  - 4.4.2 Interface with tensorial conductivity 32
  - 4.4.3 Connecting 3D conductivity to 2D conductivity 34
  - 4.4.4 Mixed Potentials in the presence of conductive interfaces 37
  - 4.4.5 Derivation of the Mixed Potentials GFs 40
- 4.5 Examples with high technological impact 40

4.5.1 Single conductive sheet . . . 41
4.5.2 Grounded slabs . . . 56
4.6 Conclusion . . . 59

5 Double Exponential (DE) Quadrature Rule 61
5.1 Numerical Integration . . . 61
5.2 Interpolatory quadratures and singular integrals . . . 62
5.3 Developing the DE transformation . . . 64
5.3.1 Performance and implementation of DE quadrature rules . . . 69
5.3.2 Adaptive DE quadrature rules . . . 72
5.3.3 DE quadratures for other types of integrals . . . 73
5.4 Conclusion . . . 75

6 Numerical Evaluation of Sommerfeld Integrals 77
6.1 Typical behavior of a Sommerfeld Integral . . . 78
6.2 First part of the Sommerfeld Integral . . . 79
6.2.1 Surface wave poles including plasmons . . . 81
6.2.2 Branch point singularity . . . 82
6.2.3 Particularities in the Double Exponential quadrature rule . . . 83
6.3 Tail of the Sommerfeld Integral . . . 84
6.4 Error Estimation . . . 85
6.4.1 Error Estimation for the first part of the Sommerfeld Integral . . . 86
6.4.2 Error Estimation for the tail of the Sommerfeld Integral . . . 87
6.5 Numerical Results . . . 88
6.5.1 Electric dipole in free space . . . 88
6.5.2 Dielectric slab . . . 92
6.5.3 Graphene sheet . . . 95
6.6 Conclusion . . . 97

7 Reaction Integrals in Surface Integral Equations 99
7.1 Weakly Singular Integrals . . . 100
7.2 Outer Integral . . . 102
7.2.1 Cartesian Product Rules . . . 102
7.2.2 DE performance . . . 103
7.2.3 Improvements in DE quadratures . . . 105
7.3 Numerical Results . . . 108
7.4 Conclusion . . . 111

8 Conclusions and Future Work **113**
8.1 Thesis assessment 113
8.2 Perspectives 114

Bibliography **115**

List of Figures **129**

List of Tables **133**

CV **135**

Publications **137**

1 Introduction

Technological advances introduce new applications and designs throughout the entire engineering community. Specifically, radio-frequency and microwave components have been greatly evolved within the recent years leading to more integrated, more precisely manufactured and far more sophisticated designs. The extremely small scale and the sensitivity of the prototypes increase fabrication costs and hinder their post-manufacturing fine tuning in order to overcome design, material and assembling tolerances. Consequently, the detailed and accurate prediction of their performance through numerical simulations is of outmost importance. The request for advanced numerical modeling is increased even more in novel scientific areas, where certain phenomena are only partially understood. Computer-aided simulations can provide further insight and contribute in the development of new products that can improve the living and health standards, reduce the costs and energy consumption or even materialize ideas never applied before.

The concept of antennas and microwave components based on multilayered structures is not new. Patch antennas and transmission lines integrated on or inside multilayered substrates have been widely used in the past due to their low cost, low profile and integrity with electronic circuits [1]. Therefore numerical techniques for their efficient Electromagnetic (EM) modeling have been proposed and implemented [2].

Recent advances in fabrication techniques and novel materials outdate the performance of the classical numerical tools and the need to adapt them in order to accommodate the new designs is evident. In more details, integration of electric circuits and feeding networks within the antenna results in structures with numerous layers, each one with different properties while all of them influencing the EM performance of the microwave components. Additionally, metallic interfaces may also be introduced in some specific applications, e.g. local field enhancement or plasmon propagation.

The introduction, though, of either very thin in terms of wavelength or even mono-atomically thick conductive sheets becomes a bottleneck for the current simulation tools. Traditionally, they were treated as bulky layers with losses. An example of a microwave component with very thin conductive layers is the solar antenna [3], a concept combining planar antennas with solar panels on the limited surface of satellites. The antenna is topped by the special conductive layers of the solar panel whose thickness is extremely small compared to the operating wavelength. The presence of the solar panel affects the performance of the antenna and only through a very precise and careful EM modeling an efficient solar antenna could be designed.

Concerning the infinitesimally thin conductive sheets, the most representative example is graphene, a true 2-D conductive material recently isolated through exfoliation of graphite [4]. The impact of graphene in the scientific community is quite impressive, justified by its unique properties, i.e. electron's high mobility, easy configurability, extreme strength etc. Due to the negative part of its conductivity within the THz range, it can support modes that are extremely confined on its surface, the so called plasmon modes [5]. Plasmon modes were already known in optical frequencies as the dielectric-metal interface can support them [6]. However, with graphene, plasmon modes can be supported and observed in lower frequencies, in the range of THz. Promising applications include bio-sensing [7], energy harvesting [8, 9], reconfigurable nano-antennas [10, 11] to mention a few.

1.1 Objectives

It becomes evident that efficient EM modeling of structures with extremely thin conductive sheets is of high importance, becoming the main objective of the thesis. The developed EM technique should be general enough, being able to take into account arbitrary number of layers and conductive sheets. Moreover, the conductivity values that the technique is able to handle should remain general, including even tensorial expressions.

Among the different Computational ElectroMagnetics (CEM) methods available, the Integral Equation method based on Method of Moments (IE-MoM) and more precisely the Mixed Potential Integral Equation (MPIE) formulation is chosen as the most appropriate one for the multilayered problems including conductive sheets previously discussed. Since the Green Functions (GFs) are the main ingredients in all the Integral Equation method based on Method of Moments (IE-MoM) formulations, the first objective here will be to develop a systematic analytical approach to compute them, especially the ones associated to the vector and scalar potentials.

Another objective is to develop a robust numerical technique for the evaluation of these GFs in the spatial domain. The danger of the propagation and amplification of numerical errors during the whole computation call for the calculation of GFs with the utmost accuracy. Therefore, reaching machine precision accuracy is not a luxury but a mandatory condition in many problems.

Furthermore, the reaction integrals, that are the entries of the MoM matrix, usually acquire plenty of computational resources due to their multi-dimensional nature. Their kernels, being singular when source and observation points coincide, downgrade the performance of the existing numerical techniques and their ability for providing accurate enough results. Development of new methods and improvements on the existing ones will definitely have an impact on the performance of CEM codes.

Having filled the MoM matrix with accurate entries, general purpose iterative solvers can be used in order to retrieve the EM fields everywhere in the multilayered structure. Further discussions on this topic go beyond the objectives of this thesis and we can safely rely on the already developed implementations available in MPIEs.

Finally, it is worth mentioning that the proposed methods should remain applicable even in absence of conductive sheets maintaing superior performance when compared to the reference techniques.

1.2 Outline

This section summarizes the contents of the chapters of the thesis and links them together in the framework of Mixed Potential Integral Equation(MPIE) for multilayered structures.

Chapter 2 serves as a short review of the existing Computational Electromagnetic (CEM) methods commenting on their recent advances towards new applications and more complicated EM problems. The Finite Differences (FD) method, the Finite Elements (FEM) method and the Integral Equation based on Method of Moments (IE-MoM) are specially considered. Due to the focus of the thesis on planar multilayered structures, the IE-MoM method is chosen as the mathematical framework because it serves in the most appropriate way their EM modeling. Additionally, the state of the art techniques for the three main topics of the thesis are presented: GF derivation of multilayered structures that include conductive sheets, numerical integration of Sommerfeld integrals and numerical evaluation of the MoM reaction integrals.

Chapter 3 presents the mathematical background of an IE-MoM code and the specific details of MPIE are provided. It serves as a roadmap towards the complete solution of the EM problem and as a platform to indicate the specific analytical and numerical techniques discussed in the next chapters.

Chapter 4 provides a general methodology for deriving the spectral domain GFs of general planar multilayered structures that include one or more conductive sheets. Special care is taken in order to handle sheets with tensorial conductivity. Modern structures that include graphene layers under electric and magnetic biases can be accurately simulated. Moreover, GFs for the vector and scalar potentials are developed, serving as the first step for using the efficient, due to its lower order singular integrals, MPIE. Multilayered structures of high technological interest are presented and analyzed.

Chapter 5 introduces a very powerful numerical integration technique, the Double Exponential (DE) rule. The basic properties and its efficiency for evaluating integrals with endpoint singularities are presented. It will be extensively used and optimized for the numerical handling of the Sommerfeld integrals and the MoM reaction integrals presented in the following chapters.

Chapter 6 deals with the transformation that connects spectral and spatial domain GFs resulting in the so-called Sommerfeld integrals. The spectral domain GFs, either for the EM fields or for the mixed potentials, including the ones developed in Chapter 4, serve as an input to the novel technique that is presented. This technique is based on an efficient numerical integration of the Sommerfeld integrals on the real axis using the Double Exponential (DE) and Weighted Averages (WA) algorithms. Error estimation of the numerical integration guarantees results of the desired, predefined, accuracy, which at the cost of a moderated increase of computational resources can even reach numerically exact values. The proposed technique is also able to handle surface plasmon modes, which at THz frequencies can be supported on structures with graphene sheets. Examples in the end of the chapter confirm the performance of the technique.

Chapter 7 serves as the next step in an IE-MoM code following the derivation of the spatial domain GFs. One of the most common choices in MoM techniques include a triangular discretization, a choice of divergence conforming basis functions and a Galerkin testing procedure. Under these conditions, the reaction integrals that fill the entries of the MoM matrix are 4-D integrals with singular kernels, in case of MPIE formulation the singularity is of order R^{-1} (weakly singular) while for other IE formulations, e.g. EFIE, CFIE etc., the singularity is of higher order. This chapter focuses on the integration of the outer 2-D surface integral. Although the singular behavior of the kernel has been alleviated through the proper treatment of the inner 2-D integration, the derivatives of this potential integral become unbounded in case that source and observation domains share common points or are relatively close the one to the other. A novel numerical technique, based on the DE rule, is used. In order to improve the performance of the algorithm the DE rule is properly parameterized and optimized.

Chapter 8 summarizes the concluding remarks and proposes future research directions within the topics covered throughout the thesis.

The following diagram visualizes the structure of the thesis, while the original contributions are highlighted with the red fonts:

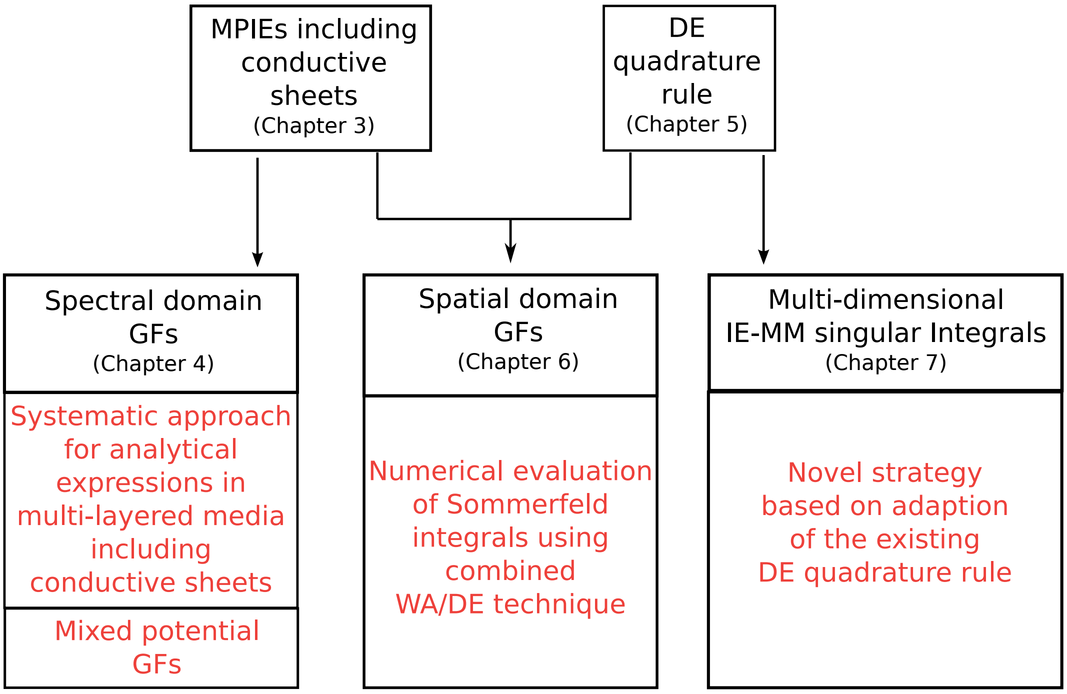
MPIEs including conductive sheets (Chapter 3)
DE quadrature rule (Chapter 5)
Spectral domain GFs (Chapter 4)
Systematic approach for analytical expressions in multi-layered media including conductive sheets
Mixed potential GFs
Spatial domain GFs (Chapter 6)
Numerical evaluation of Sommerfeld integrals using combined WA/DE technique
Multi-dimensional IE-MM singular Integrals (Chapter 7)
Novel strategy based on adaption of the existing DE quadrature rule

Figure 1.1: Thesis's contents and original contributions (in red) in a nutshell.

2 State of the Art

Computational Electromagnetics (CEM) has received increasing attention over the last decades in an effort to design competitive and robust electromagnetic components for a broad range of applications, e.g. radar imaging, wireless and optical communications, RF/microwave guidance and filtering to name only but a few. The development of new materials, the improvements in fabrication techniques, the tendency to higher frequencies and finally the wider influence of electromagnetic based applications in other sciences call for more competitive, more efficient and more interdisciplinary approach to the development of numerical methods, keeping the scientific interest in CEM continuously high.

All the CEM methods are based on the solution of the same set of integro-differential equations, i.e. Maxwell's equations by applying the relevant boundary conditions and excitation. Due to the inherent complexity of the equations and the rarely canonical geometries of the designs, most of the EM problems have to be analyzed numerically and therefore many different CEM methods have been developed for various applications.

One of the first methods that was developed is the Finite Differences (FD) method [12]. More popular within the time domain framework, resulting in the Finite Differences Time Domain (FDTD) scheme, it still serves as an excellent candidate due to its combined generality and simplicity. It can relatively easy to handle dispersive materials [13], metamaterials [14] as well as Gaussian and pulsed signals [15]. Recently, it has received an additional boost due to its convenient implementation on Graphics Processing Units (GPUs) [16], which increases the computational resources available, reduces the solution time and paves the way to extremely large or detailed EM problems. One of the main drawbacks of the method remains the unbounded domain that has to be discretized and terminated with artificial boundary conditions in order to fulfil the radiation condition at infinity [17]. Space and time steps must satisfy the Courant-Friedrichs-Lewy (CFL) condition otherwise the time integration is likely to be unstable [18]. The CFL condition is very strong and especially if thin films or wires are present, the required time step will become very short leading to extremely long simulation times. Finally, curved geometries are difficult to be included in the naturally chosen rectangular grid of FDTD [19]. As expected, researchers have proposed plenty of solutions in order to to alleviate each one of such drawbacks, always at the cost of sacrificing at some extend the great simplicity of the method.

Another wide family in CEM is the Finite Elements Method (FEM). It was initially introduced in [20] while an extensive historical overview of FEM tailored to EM problems can be found in [21]. It is based on the minimization of some functional that can be related to physical considerations like the minimum energy criterium etc [22]. Their solution domain can be easily discretized in elements of convenient size and shape, e.g. bricks, prisms, pyramids with straight or curved faces to name only but a few. FEM is quite popular also in neighboring EM societies and multi-physics codes for coupling EM, thermal or stress problems have been successfully developed [23]. Finally, new generation FEM, like the discontinuous Galerkin schemes [24], incorporate the philosophy of domain decomposition for solving extremely large problems [25]. Drawbacks of the method include the appropriate termination of the computational domain in radiating structures, the ill-conditioning of the related matrices in cases of multiscale problems [26] and the increased number of unknowns as the whole solution domain needs to be discretized [22].

Alternatively to FD and FEM, the non-homogeneous solution of the differential form of Maxwell's equation can be used as a basis for a numerical method. This solution, called Green Function (GF), satisfies the boundary conditions of the problem and includes the impulse response of the structure under a Dirac δ excitation [27]. Using the superposition principle and the convolution of the GF with an arbitrary function, the EM solution of the specific problem can be derived. The choice of the arbitrary function and its discretizetion through the procedure of the Method of Moments (MoM) [28], leads to the Integral Equations (IE) technique formed in [29]. Based on equivalence principles, incident fields and scattered ones by the equivalent sources are properly matched on selected surface boundaries [30]. One of the advantages of this method is that only the area of the equivalent sources needs to be discretized instead of the whole volume within which the EM fields exist, resulting in a lower amount of unknowns. The price to pay is that the resulting matrices are not any more sparse as in the case of FD and FEM methods but they are fully populated. Moreover, IEs methods require advanced mathematical treatment firstly in order to derive the appropriate GF for each EM problem and secondly because of the resulting singular integrals.

Depending on the basic boundary condition to be enforced, different IE formulations can be derived [31]. The two most common families, belonging to the Surface Integral Equations (SIE), are based on boundray conditions for the tangential Electric Field (EFIE) and tangential Magnetic Field (MFIE). The first one suffers from the internal resonance issue, while the second one, being a Fredholm integral equation of the second kind, is ill-conditioned [32]. As a remedy to these issues, the EFIE and MFIE can be linearly combined together, as the resonant modes of EFIE differ from the ones of MFIE [33]. This leads to the Combined Field IE (CFIE), with the Poggio-Miller-Chang-Harrigton-Wu (PMCHW) formulation [34] being the most widely used. Alternatively, the continuity equations for the electric and magnetic currents can be combined forming the family of the Augmented Field Integral Equations (AFIE) [35]. All the IEs that include the EFIE kernel result in strongly singular integrals which are difficult to be evaluated. As a solution, the less singular scalar and vector potential GFs can be used in order to develop the so-called Mixed Potential IE (MPIE) [36–38].

Recently, extremely large EM scattering problems, like scattering from metallic airplanes, ships, etc. have been solved using IEs applying the Fast Multiple Method (FMM) [39], the Multi-level Fast Multiple Algorithm (MLFMA) [40, 41] or the Adaptive Integral Method (AIM) [42]. Additionally, the combination of Volume IEs, where the equivalent sources are spread over a volume instead of a surface, with the pre-corrected Fast Fourier Transform (pFFT) [43, 44] has been used, in order to derive the EM fields due to the presence of complicated inhomogeneous dielectric structures like the human head [45, 46]. All these methods allow an efficient computation of matrix-vector products enabling the solution of very big systems within reasonable time applying iterative solvers. Another approach to handle big problems is reducing the total amount of unknowns by gathering the basis functions in groups. This idea can be found in Synthetic Basis Functions (SBF) [47], Characteristic Basis Functions (CBF) [48], Macro-Basis Functions (MBF) [49], to mention only but a few.

In general, the treatment of the MoM matrix remains quite independent on the specific nature of the matrix elements. Therefore, all the above discussed strategies [39–49] are expexted to remain valid and compatible with the new GFs introduced hereby.

In more details, this thesis focuses on the EM analysis of planar multilayered structures and one of the most efficient ways of their modeling is reported to be the IEs [38]. The analytical and numerical challenges hidden behind the integral representation of EM fields serves as an excellent motivation for further research within the CEM framework.

Among these challenges, this thesis concentrates on the development of the proper GF of the IEs for multilayered structures with conductive sheets, their numerical evaluation through the so-called Sommerfeld integrals and finally on the computational issues on the multi-dimensional reaction integrals after the application of the MoM procedure.

2.1 Integral Equations in Multilayered Structures

The main core of IEs and one of the most difficult tasks is the development of the GF which corresponds to the geometry and satisfies the boundary conditions. If the structure consists of a plane, stratified medium with rotational symmetry, then the GF can be easier obtained in the spectral or Fourier transform domain. Structures that fit these considerations include patch antennas with many dielectric layers and excitations, photonic crystals, transmission lines and microwave components on multilayered PCBs etc.

The recent boost in applications of graphene, a monoatomic carbon sheet recently isolated through exfoliation of graphite [4], is extremely important within fundamental physics and electronic devices [50]. Graphene's high mobility, optical transparency, configurability through external biases and robustness increase its potential use ranging from solar cells, light emitting devices to touch screens and photodetectors [51, 52].

Following the high potential of graphene, novel monoatomic sheets have recently been fabricated and continue being developed, which may replace graphene in some applications or even introduce new ones [53]. From an EM point of view, all this family of materials can be considered as extremely thin conductive layers within a multilayered structure.

Even in cases where the thickness of the conductive layer is not monoatomic but still much smaller than the operating wavelength, the same approximations as in the true monoatomic layers can be used, from an EM point of view. A typical example is the solar antenna [3], where conductive layers, necessary for the solar panel performance of the solar antenna, are embedded in the multilayered structure of the antenna.

From a more mathematical point of view, with a suitable rotation of the coordinate system, EM fields can be decomposed in TE and TM waves and the spectral domain GFs can be derived through equivalent Transmission Line Models (TLM) [54, 55]. Then the TLMs are solved and the resulting voltages and currents are related to the spectral domain GFs [56–58]. The introduction of structures with very thin conductive layers complicates the development of the TLM, especially in the case where conductivity is of tensorial nature. Then, the tensor mixes the contributions of the TE and TM modes, which cannot any more be evaluated independently.

Similarly to TLM, the Transverse Resonance Method (TRM) [59, 60] has been widely used to derive the propagating modes of structures that include graphene sheets [61–63]. However, TRM is restricted to the propagation characteristics of the multilayered structure, whereas through TLM the EM fields can also be calculated by introducing the appropriate voltage and current sources.

TLM is still applicable but is restricted to very simple geometries that include only one or two conductive sheets [62]. The reason for the limited applicability of TLM is that the boundary conditions on conductive interfaces are based on physical considerations of EM currents and fields rather than equivalent currents and voltages of the TLM. Alternatively, the technique of transmission or propagating matrices of the EM fields throughout different layers [2] is more convenient for structures that include conductive interfaces. An early demonstration of this idea focusing on periodic structures can be found in [64]. Consequently, throughout this thesis, the spectral domain GFs will be developed by enforcing the appropriate boundary conditions directly, circumventing the fictitious voltages and currents.

Moving a step further, the GFs of the EM fields of such multilayered structures are linked to the vector and scalar potentials GFs, serving as the first step for a MPIE formulation. All these contributions are discussed in Chapter 4.

2.2 Numerical Techniques for Sommerfeld Integrals

Once the spectral domain GFs have been developed, the spatial domain counterparts have to be retrieved through inverse Fourier Transform. In case of rotational symmetry this yields to the so-called Sommerfeld integrals [65]. The spectral domain GFs have poles in the complex plane, while the presence of Bessel functions in the Sommerfeld integrals adds oscillations. The integration domain extends to infinity and the integral may show a slow convergence. All these combined techniques end up in a very delicate numerical problem.

The Complex Image Method (CIM) was proposed to tackle the numerical evaluation of Sommerfeld integrals [66]. The spectral domain GF is split into three contributions, the quasi-static term, the surface waves and the remainder. The first two can be handled analytically, while the last one is fitted to a series of complex exponentials which can be transferred to the spatial domain through the Sommerfeld identity [67–71]. The fitting of the remainder to the complex exponentials introduces an error, which until recently was difficult to be estimated. An initial attempt to relate the fitting error in the spectral domain to the related one in the spatial domain was addressed in [72].

An alternative strategy is the direct numerical evaluation of the Sommerfeld integral using specialized techniques. The integral is traditionally split in two parts, the first part and the tail of the Sommerfeld integral due to the different behavior of the kernel in the two integration domains. The first part includes all the poles and is evaluated using the residue theorem in order to circumvent the poles combined with special variable transformation for the branch point [73, 74]. The oscillating one is treated efficiently with the Weighted Averages (WA) method [74]. Further developments have been applied to these techniques throughout the years. For the first part, a deviation in the complex plane has been proposed in order to avoid the poles, as well as the difficult procedure to locate them [75]. Additionally, an integration following the imaginary axis has been proposed [76]. Taking advantage of recent developments in the pole location algorithms [77], a novel technique is developed within the framework of this thesis in Chapter 6 based on the real-axis-integration, where specialized quadrature rules are used in order to provide an efficient and error bounded algorithm for general multilayered GFs. Concerning the tail of the Sommerfeld integral, a revised version of the WA has been developed [78], which competes against advanced quadratures for integrating oscillatory integrands over semi-infinite domains [79, 80].

2.3 Numerical Techniques for Reaction Integrals

The reaction integrals are the entries in the MoM matrix of the IE formulation. They are 4-D integrals in case of Surface IEs (SIEs) or even 6-D in case of Volume IEs (VIEs), if a Galerkin MoM is applied, as they include the interaction between observation and source elements. Moreover, certain components become singular when observation and source points coincide, with the maximum order of the singularity depending on the IE formulation chosen. In the case of EFIE, kernels with singularities R^3 are present, whereas if MPIE is used, the singularities are reduced to R^1, R being the distance between source and observer. For this reason, the MPIE is chosen as the targeting IE method within this thesis.

The accuracy in these numerical evaluation of the integrals is crucial, as this will increase the condition number of the matrix and consequently the number of iterations for the solver to converge, if an iterative one is used. Not to mention the propagation of the errors that will affect the accuracy of the final solution.

One of the most common strategies is the split between the inner and the outer integral. The inner integral, called also potential integral, describes the potential at a certain observation point of the source domain. In general, there are two ways of annihilating the singular behavior of the potential integral, the singularity cancelation and the singularity subtraction technique. With the singularity cancelation, a special variable transformation is applied whose Jacobian cancels approximately or exactly the singularity [81–85]. Then, the transformed integral can be efficiently handled with standard numerical integration techniques due to the cancelation of the singularity. On the other hand, the singularity subtraction technique is based on the subtraction of the singular term from the GF. This term can be integrated analytically, while the remainder, free of singular points, can be integrated numerically without difficulties [86–89]. It should be pointed out that most of these strategies perform quite well for squares or triangles close to the equilateral one, whereas their performance drops as the integration domains get more stretched due to the poor behavior of the mesh tools, or in cases where the separation between the source domain and the observation point is quite small [82–85, 90]. For this reasons, new transformations and improvements are frequently presented in order to address such issues.

Concerning the outer integral, its numerical integration was usually considered trivial, as the singular behavior of the potential integral has already been alleviated either through the singularity cancelation or singularity subtraction method. Unfortunately, this is not the case.

If the observation and source domain coincide or share some common points, the potential integral has a $d \log d$ behavior close to these areas, where d is the normal distance to the common edge or just the common point, resulting in unbounded derivatives of the potential integral. In the limit of the static case, the singular behavior $d \log d$ can be isolated analytically and therefore properly treated [91]. In the dynamic case this is not any more possible. Within this thesis, a new optimized numerical algorithm is developed, which is able to handle efficiently and up to machine precision the evaluation of the outer integral. The proposed method is general and remains valid and competitive for all types of source and observation domains, overlapping, sharing single edge or point, or even in the case that source and observation domains are just very close the one to the other.

Alternatively, the treatment of the full reaction integral can be performed with the Direct Evaluation Method [92, 93]. The inner and the outer integrals are not any more treated independently, but a reordering of the second integration of the inner integral with the first integration of the outer integral and some suitable variable transformations are capable of regularizing the kernel of the integral. Therefore, standard integration techniques can be used. The disadvantage of the method is the load of the analytical preprocessing needed, which is dependent on the integration domain, the kernel and the basis functions used. Furthermore, in the case that source and observation domains are close to each other but do not share any common points, this method has limited applicability. It will be used during the thesis in order to obtain reference results to compare against the numerical algorithms that are discussed in Chapter 7.

3 Potentials and Integral Equations: a Reminder

Among the various methods for solving numerically EM problems, this thesis concentrates in the Surface Integral Equations (SIE) model and in particular in the Mixed Potential Integral Equation (MPIE) which is chosen to be the basis for the further numerical evaluations and contribution presented in the current thesis. For this reason, this chapter includes a short introduction to IEs and additional emphasis to MPIE. The main procedures and difficulties are discussed paving the way for the more thorough discussions presented in the following chapters.

3.1 Integral Equation approach

The EM fields in an arbitrary medium are generally governed by Maxwell's equations. If harmonic signals with a time dependency of $e^{j\omega t}$ are assumed, Maxwell's equations can be written as [94]:

$$\nabla \times \mathbf{E} = -j\omega\mathbf{B} - \mathbf{M} \tag{3.1a}$$

$$\nabla \times \mathbf{H} = +j\omega\mathbf{D} + \mathbf{J} \tag{3.1b}$$

$$\nabla \cdot \mathbf{B} = q_m \tag{3.1c}$$

$$\nabla \cdot \mathbf{D} = q_e \tag{3.1d}$$

where $\mathbf{M}$ and q_m are the fictitious magnetic currents and charges that are introduced in order to make Maxwell's equations symmetric. The electric and magnetic fields are related to their corresponding fluxes $\mathbf{D}$ and $\mathbf{B}$, respectively, and the electric field $\mathbf{E}$ to the induced current $\mathbf{J}$ through the constitutive relationships:

$$\mathbf{D} = \epsilon\mathbf{E} \tag{3.2a}$$

$$\mathbf{B} = \mu\mathbf{H} \tag{3.2b}$$

$$\mathbf{J} = \bar{\bar{\sigma}}\mathbf{E} \tag{3.2c}$$

where ϵ stands for the permittivity, μ for the permeability and $\bar{\bar{\sigma}}$ for the electric conductivity of the medium. In the general case, also μ and ϵ should be considered as tensors. During this thesis, they will be assumed scalar and only the tensorial nature of conductivity will be exploited.

Further on, we define the dyadic Green Function (GF) $\bar{\bar{\mathbf{G}}}_{PQ}(\mathbf{r},\mathbf{r}')$ as the vectorial field $\mathbf{P}$ at a point $\mathbf{r}$ created by a vectorial δ source $\mathbf{Q}$ at a point $\mathbf{r}'$.

Consequently, and taking into account the linearity of Maxwell's equations, the scattered EM fields due to a source distribution $\mathbf{J}$ defined over a surface S' are:

$$\mathbf{E}^s = \iint_{S'} \bar{\bar{\mathbf{G}}}_{EJ}(\mathbf{r}, \mathbf{r}')\mathbf{J}(\mathbf{r}')dS' \tag{3.3a}$$

$$\mathbf{H}^s = \iint_{S'} \bar{\bar{\mathbf{G}}}_{HJ}(\mathbf{r}, \mathbf{r}')\mathbf{J}(\mathbf{r}')dS' \tag{3.3b}$$

It is worth mentioning that equivalent magnetic currents $\mathbf{M}$ can also be introduced, especially if the geometry has a lot of metallizations with few dielectric openings. The inclusion of magnetic sources implies the introduction of $\bar{\bar{\mathbf{G}}}_{EM}$ and $\bar{\bar{\mathbf{G}}}_{HM}$ in (3.3). However, magnetic sources will be dropped in the subsequent analysis, and if needed they can relatively easily be taken into account in a later step [95].

In case that the sources span over a volume V' instead of the surface S', then the integrals become three dimensional and form the basis for Volume Integral Equations (VIE). Within this thesis, we will assume that the sources remain on surfaces and the IEs developed belong to the family of Surface Integral Equations (SIE).

Enforcing the appropriate boundary conditions for the total fields $\mathbf{E} = \mathbf{E}^i + \mathbf{E}^s$ and $\mathbf{H} = \mathbf{H}^i + \mathbf{H}^s$ and replacing the scattered fields by (3.3) on Perfect Electric Conductors (PEC), Perfect Magnetic Conductors (PMC) or impedance surfaces, SIEs are derived. The weak point of these equations is that several components of the field-type GFs have a strong singularity of type R^{-3}, making the numerical evaluation of the integrals in (3.3) really complicated.

In order to overcome this numerical difficulty, vector and scalar potentials have been introduced as an intermediate step that connect the sources to the fields while avoiding the strong singularities of field IEs, which are discussed in the next section.

3.2 Vector and Scalar Potentials

An alternative approach to directly work on the field level (electric and magnetic) is to use the mixed potential approach. Based on the non-divergence of the magnetic flux $\mathbf{B}$:

$$\nabla \cdot \mu\mathbf{H} = \mathbf{0} \tag{3.4}$$

a vector potential A can be introduced such that:

$$\mu\mathbf{H} = \nabla \times \mathbf{A} \tag{3.5}$$

By inserting (3.5) into Maxwell's equations:

$$\nabla \times \mathbf{E} = -j\omega\mu\mathbf{H} \Leftrightarrow \nabla \times (\mathbf{E} + j\omega\mathbf{A}) = \mathbf{0} \tag{3.6}$$

the definition of a scalar potential becomes also evident:

$$\mathbf{E} + j\omega\mathbf{A} = -\nabla V \tag{3.7}$$

At this point, the equivalent magnetic current $\mathbf{M}$ and magnetic charge q_m have been dropped from (3.6) and only electric sources will be assumed from now on.

If we want to link the potentials $\mathbf{A}$ and V to the sources ρ_V and $\mathbf{J}_V$, this is easily done through Maxwell's equations resulting in:

$$\nabla^2 V + j\omega \nabla \cdot \mathbf{A} = -\frac{q_e}{\epsilon} \tag{3.8}$$

and

$$\nabla^2 \mathbf{A} - \nabla(\nabla \cdot \mathbf{A} + j\omega\epsilon\mu V) + \omega^2 \epsilon\mu \mathbf{A} = -\mu \mathbf{J} \tag{3.9}$$

From (3.8) and (3.9) it can be seen that as the potentials are defined through differential operators, there is no unique definition of them and if $\mathbf{A}$ and V are the solutions of an EM problem and ψ an auxiliary scalar function, then $\mathbf{A}'$ and V', defined as:

$$\mathbf{A}' = \mathbf{A} + \nabla\psi \tag{3.10}$$

$$V' = V - j\omega\psi \tag{3.11}$$

are also solutions of the same EM problem. The uniqueness of the potentials is resolved by choosing a gauge. From now on we will use the Lorenz Gauge [95, 96]:

$$\nabla \cdot \mathbf{A} + j\omega\epsilon\mu V = 0 \tag{3.12}$$

By introducing (3.12) into (3.8) and (3.9), we get classical Helmholtz-type differential equations for $\mathbf{A}$ and V:

$$\nabla^2 \mathbf{A} + k^2 \mathbf{A} = -\mu \mathbf{J} \tag{3.13}$$

$$\nabla^2 V + k^2 V = -\frac{q_e}{\epsilon} \tag{3.14}$$

where $k = \omega\sqrt{\mu\epsilon}$ is the wavenumber of the medium. If the excitations $\mathbf{J}$ and q_e are replaced by delta sources, i.e. $\mathbf{J} = \bar{\bar{\mathbf{I}}}\delta(\mathbf{r} - \mathbf{r}')$ and $q_e = \delta(\mathbf{r} - \mathbf{r}')$, respectively, then the solutions of (3.13) and (3.14) are indeed the Green Functions $\bar{\bar{\mathbf{G}}}_A$ and G_V:

$$\nabla^2 \bar{\bar{\mathbf{G}}}_{\mathbf{A}} + k^2 \bar{\bar{\mathbf{G}}}_{\mathbf{A}} = -\mu \bar{\bar{\mathbf{I}}}\delta(\mathbf{r} - \mathbf{r}') \tag{3.15}$$

$$\nabla^2 G_V + k^2 G_V = -\frac{\delta(\mathbf{r} - \mathbf{r}')}{\epsilon} \tag{3.16}$$

If we follow the Sommerfeld approach [2, 38, 65] then a $\hat{z}$ orinented dipole can be described only through the vertical component A_z, while a $\hat{x}$ or $\hat{y}$ oriented dipole needs in addition a second component parallel to the source. Consequently, out of the 9 terms of the dyad $\bar{\bar{\mathbf{G}}}_A$, it is sufficient to define only 5 non-zero entries as following:

$$\bar{\bar{\mathbf{G}}}_A = \begin{bmatrix} G_A^{xx} & 0 & 0 \\ 0 & G_A^{yy} & 0 \\ G_A^{zx} & G_A^{zy} & G_A^{zz} \end{bmatrix} \tag{3.17}$$

Taking into account the following relationships:

$$j\omega\mu\epsilon\bar{\bar{\mathbf{G}}}_{EJ} = k^2\bar{\bar{\mathbf{G}}}_A + \nabla\nabla\cdot\bar{\bar{\mathbf{G}}}_A \tag{3.18}$$

$$j\omega\mu\epsilon\bar{\bar{\mathbf{G}}}_{HJ} = j\omega\epsilon\nabla\times\bar{\bar{\mathbf{G}}}_A \tag{3.19}$$

the GFs of the EM fields are related to the GFs of the mixed potentials.

In Chapters 4 and 6, a strategy for deriving and numerically implementing the potential GFs $\bar{\bar{\mathbf{G}}}_A$ and G_V for multilayered structures that include arbitrary number of conductive sheets is developed.

3.3 Mixed Potential Integral Equation

The next step, after having obtained the potential GFs $\bar{\bar{\mathbf{G}}}_A$ and G_V of a structure, is to develop the integral equation that relates the sources, electric currents and charges, to the produced electric field $\mathbf{E}$. This is done through (3.7) resulting in the final form of the Mixed Potential Integral Equation (MPIE):

$$\mathbf{E} = -j\omega\iint_{S'}\bar{\bar{\mathbf{G}}}_A\mathbf{J}dS' - \nabla\iint_{S'}G_Vq_edS' \tag{3.20}$$

where the electric sources are distributed over the surface S'. Equivalently, a secondary MPIE equation can be written for the magnetic field $\mathbf{H}$ created by electric sources:

$$\mathbf{H} = -\frac{1}{\mu}\nabla\times\iint_{S'}\bar{\bar{\mathbf{G}}}_A\mathbf{J}dS' \tag{3.21}$$

The greatest advantage of the MPIE formulation (3.20) are the milder singularities of the GFs compared to other IEs [2], e.g. EFIE, CFIE, etc., resulting in less numerical implications and consequently higher accuracy for the same amount of computational effort. The main drawback of the MPIE is the introduction of an additional unknown that is the electric charge q_e.

3.3.1 Method of Moments

The MPIE defined by (3.20) and (3.21) serves as a connection between the sources and the fields. In the EM problems that we are dealing with, the sources are unknown, which are represented as a set of N vectorial basis functions $\mathbf{f}_j$ with amplitudes to be determined:

$$\mathbf{J} = \sum_{j=1}^{N}a_j\mathbf{f}_j \tag{3.22}$$

Afterwards, (3.20) is tested against a set of N vectorial weight functions $\mathbf{w}_i$, through a projection technique using internal products. These two steps constitute the so called Method of

Moments (MoM) technique [28] which leads to the MoM system matrix:

$$[M]\mathbf{a} = \mathbf{v} \tag{3.23}$$

In (3.23), the elements of the vector $\mathbf{a}$ are the unknown amplitudes a_j of (3.22). Moreover, the elements m_{ij} of the matrix $[M]$, by applying the continuity equation, are the reaction integrals:

$$m_{ij} = -j\omega \iint_S \mathbf{w}_i \iint_{S'} \bar{\bar{\mathbf{G}}}_A \mathbf{f}_j dS dS' - \frac{1}{j\omega} \iint_S \nabla \cdot \mathbf{w}_i \iint_{S'} G_V \nabla' \cdot \mathbf{f}_j dS dS' \tag{3.24}$$

while the elements of the excitation vector v_i are defined as:

$$v_i = \iint_S \mathbf{w}_i \cdot \mathbf{E}^i dS \tag{3.25}$$

$\mathbf{E}^i$ being the exciting electric field. The choices for the basis $\mathbf{f}_j$ and weight $\mathbf{w}_i$ functions are numerous. One of the most common choices for the basis functions $\mathbf{f}_j$ are rooftops if their support domain S' is rectangular or RWG [97] for triangular domains. The Galerkin approach that forces the set of the weight functions to coincide with the one of the basis functions, i.e. $\mathbf{w}_i = \mathbf{f}_i$, usually leads to more accurate results which completes the skeleton of the numerical solution of EM problems through MPIE.

The four dimensional integrals of (3.24) still have the weak singularity R^{-1} and special treatment is required. A very efficient numerical method for such a task is developed in Chapter 7.

4 EM Modeling of Multilayered Structures

One of the keystones in the development of an Integral Equation - Method of Moment (IE-MoM) code is the derivation of the Green Function (GF) of the structure under consideration. For planar multilayered cases, this task is quite simplified by applying a two dimensional Fourier transform in the lateral coordinates. Then, the GFs in the transformed spectral domain can be derived in closed form. Simple geometries like dielectric slabs which is the building block for microstrip antennas, have been intensively studied for many years [29, 31, 56, 66, 98]. GFs for arbitrary multilayered structures can be obtained either by solving the equivalent transmission line problem [98] or by employing the technique of the propagator matrix [2]. Once the spectral domain GFs are developed, the spatial domain counterparts are obtained, most of the times numerically, through the so-called Sommerfeld integrals [65]. The spatial domain GFs are used to construct the MoM matrix, as discussed in Section 3.3.1 in order to solve the considered EM problem.

Most of the previously mentioned methods to obtain the spectral domain GFs are tailored for applications that include stratified media. The recent manufacturing of extremely thin, even mono-atomically thick, conductive sheets like graphene [4] open a new era with wide range of applications varying from solar cells to plasmonic and THz diagnostic devices [3, 51, 52]. Plenty of these applications, can fit very well in the framework of the planar multilayered structures, where thin conductive sheets separate the dielectric layers. Traditional methods would consider the conductive sheets as thin lossy dielectric layers. However, the thinner the layer, the less stable the algorithms become, not to mention the limiting case of the monoatomic thickness of graphene. Recently, the Transverse Resonance Method (TRM) has been used in order to derive the propagating characteristics of plasmon modes in simple structures that include one or two conductive sheets [61–63]. Frequently, conductivity is considered to be scalar. Only few publications consider conductivity tensorial, which is the case of graphene sheets biased by a magnetic field [62, 99]. However, the TRM method is limited to deriving modes but not GFs and fields. Some authors have managed to derive GFs for the fields of simple graphene structures [100, 101], restricting themselves in scalar conductivity cases. This thesis serves as a complement to these works, proposing a general methodology for deriving GFs, both on the field and potential level, for arbitrary number of dielectric layers and conductive sheets, either with scalar or tensorial conductivity.

The current work treats the conductive sheets as boundary conditions connecting dielectric layers, and their conductivity is treated such as to keep its general tensorial nature. The dielectric layers are considered isotropic regarding their electric permittivity and permeability. In Section 4.1 the general mathematical framework for Maxwell's equations for multilayered structures is presented. It is followed by the spectral-spatial transformations in Section 4.2. The propagator matrix technique [2, 102] is reviewed and a generalized algorithm is provided in Section 4.3 in order to derive the spectral domain GFs of EM fields and potentials for arbitrary multilayered structures. This algorithm is enhanced in Section 4.4 in order to include thin conductive layers and scalar and vector potential GFs are obtained. Finally, in Section 4.5, examples of high technological impact are presented, accompanied by their corresponding mixed potential GFs.

4.1 Maxwell Equations for Multilayered Structures

To begin with, Maxwell's equations of (3.1) can be rearranged so as all the transverse fields components, either electric or magnetic, are related only to the normal components [95].

In order to do so, the transverse vectorial quantities and operators are defined as follows:

$$\mathbf{S} = \mathbf{S}_t + S_z \hat{z} \tag{4.1}$$

$$\nabla = \nabla_t + \frac{\partial}{\partial z}\hat{z}, \tag{4.2}$$

where $\mathbf{S}$ stands for either $\mathbf{E}$, $\mathbf{H}$, $\mathbf{J}$ or $\mathbf{M}$. After some algebraic manipulation of the Maxwell equations and the insertion of the previous notation, the following set of equations can be obtained, following the developments of [103, 104]:

$$\nabla_t \times \mathbf{E}_t = -(j\omega\mu H_z + M_z)\hat{z} \tag{4.3a}$$

$$\nabla_t \times \mathbf{H}_t = (j\omega\epsilon E_z + J_z)\hat{z} \tag{4.3b}$$

$$\frac{\partial \mathbf{E}_t}{\partial z} - \nabla_t E_z = -(j\omega\mu \mathbf{H}_t + \mathbf{M}_t) \times \hat{z} \tag{4.3c}$$

$$\frac{\partial \mathbf{H}_t}{\partial z} - \nabla_t H_z = (j\omega\epsilon \mathbf{E}_t + \mathbf{J}_t) \times \hat{z} \tag{4.3d}$$

With the help of some additional mathematical operations, the previous set of equations (4.3) can be written in the following way:

$$\frac{\partial \mathbf{E}_t}{\partial z} = -j\omega\mu(\mathbf{H}_t \times \hat{z}) + \frac{1}{j\omega\epsilon}\nabla_t(\nabla_t \cdot (\mathbf{H}_t \times \hat{z})) - \frac{1}{j\omega\epsilon}\nabla_t J_z - \mathbf{M}_t \times \hat{z} \tag{4.4a}$$

$$\frac{\partial \mathbf{H}_t}{\partial z} = j\omega\epsilon(\mathbf{E}_t \times \hat{z}) - \frac{1}{j\omega\mu}\nabla_t(\nabla_t \cdot (\mathbf{E}_t \times \hat{z})) - \frac{1}{j\omega\mu}\nabla_t M_z + \mathbf{J}_t \times \hat{z} \tag{4.4b}$$

$$E_z = \frac{1}{j\omega\epsilon}\nabla_t(\mathbf{H}_t \times \hat{z}) - \frac{1}{j\omega\epsilon}J_z \tag{4.4c}$$

$$H_z = -\frac{1}{j\omega\mu}\nabla_t(\mathbf{E}_t \times \hat{z}) + \frac{1}{j\omega\mu}M_z \tag{4.4d}$$

No further manipulation will be performed in the aforementioned equations for the moment. It is much easier to perform a double Fourier transformation, as introduced in the following chapter, on all these equations since they become simpler in the transformed domain.

4.2 Spectral Domain Transformation & Sommerfeld Integrals

One of the most efficient techniques for handling problems that are transversally invariant is the spectral domain approach. According to this, the transverse Cartesian coordinates x, y are replaced by their spectral counterparts k_x and k_y based on the following double Fourier transformation pair:

$$f(x,y) = \mathrm{IFT}\{\tilde{f}(k_x,k_y)\} = \frac{1}{2\pi}\iint_{-\infty}^{\infty} \tilde{f}(k_x,k_y)e^{jk_xx}e^{jk_yy}dk_xdk_y \tag{4.5}$$

$$\tilde{f}(k_x,k_y) = \mathrm{FT}\{f(x,y)\} = \frac{1}{2\pi}\iint_{-\infty}^{\infty} f(x,y)e^{-jk_xx}e^{-jk_yy}dxdy \tag{4.6}$$

One of the greatest simplifications, thanks to this transformation, is the handling of the spatial derivatives, which for the case of the transverse coordinates become multiplications:

$$\frac{\partial}{\partial x} \rightarrow jk_x \tag{4.7}$$

$$\frac{\partial}{\partial y} \rightarrow jk_y \tag{4.8}$$

$$\nabla = \nabla_t + \frac{\partial}{\partial z}\hat{z} \rightarrow \tilde{\nabla}_t + \frac{\partial}{\partial z}\hat{z} = j\mathbf{k}_\rho + \frac{\partial}{\partial z}\hat{z}, \tag{4.9}$$

where $\mathbf{k}_\rho = k_x\hat{x} + k_y\hat{y}$.

Moreover, the differential operator of the Helmholtz equation in the spectral domain is transformed in the following way:

$$\nabla^2 + k^2 \rightarrow \frac{\partial^2}{\partial z^2} + k_z^2, \tag{4.10}$$

$k_z^2 = k^2 - k_\rho^2$, resulting in a 1D second order differential operator.

If the function $\tilde{f}$ depends only on k_ρ and not on k_x and k_y independently, a rotational symmetry can be implied and the 2D integral can be reduced to a 1D one through a polar coordinate transformation:

$$k_x = k_\rho \cos(k_\phi) \tag{4.11}$$

$$k_y = k_\rho \sin(k_\phi) \tag{4.12}$$

It can be proven that if there is no dependency on the angular coordinate k_ϕ (rotational symmetry), i.e. $\tilde{f}(k_\rho,k_\phi) = \tilde{f}(k_\rho)$, then the double Fourier transformation reduces to the Sommerfeld integral S_0:

$$f(\rho) = S_0[\tilde{f}] = \int_0^\infty J_0(k_\rho\rho)k_\rho\tilde{f}(k_\rho)dk_\rho, \tag{4.13}$$

where $\rho^2 = x^2 + y^2$ and J_0 is the Bessel function of 1^{st} kind of 0^{th} order. The spatial domain angular coordinate $\phi = \arctan(y/x)$ has already been analytically integrated in (4.13).

Even though the multilayered structure is assumed rotationally symmetric in the transverse plane, rotationally asymmetric excitations may result in presence of k_ϕ in the spectral and ϕ in the spatial domain, respectively.

Even in this case, a transformation through the polar coordinates can be performed resulting in generalized Sommerfeld integrals:

$$S_n[\tilde{f}] = \int_0^\infty J_n(k_\rho \rho) k_\rho^{n+1} \tilde{f}(k_\rho) dk_\rho \tag{4.14}$$

Then, assuming a function $\tilde{g} = \tilde{g}(k_\rho)$ and applying the appropriate properties of Bessel functions [105, 106], the transformations shown in Table 4.1 are applicable.

Spectral Domain	Spatial Domain
$\tilde{G} = \tilde{A}$	$G = S_0[\tilde{A}]$
$\tilde{G} = jk_x\tilde{A}$	$G = -\cos(\phi)S_1[\tilde{A}]$
$\tilde{G} = jk_y\tilde{A}$	$G = -\sin(\phi)S_1[\tilde{A}]$
$\tilde{G} = k_x^2\tilde{A}$	$G = -\frac{\cos(2\phi)}{\rho}S_1[\tilde{A}] + \cos^2(\phi)S_0[k_\rho^2\tilde{A}]$
$\tilde{G} = k_y^2\tilde{A}$	$G = \frac{\cos(2\phi)}{\rho}S_1[\tilde{A}] + \sin^2(\phi)S_0[k_\rho^2\tilde{A}]$
$\tilde{G} = k_x k_y\tilde{A}$	$G = -\frac{\sin(2\phi)}{\rho}S_1[\tilde{A}] + \frac{1}{2}\sin(2\phi)S_0[k_\rho^2\tilde{A}]$

Table 4.1: Transformations between the spectral and the spatial domain for various expressions of $\tilde{G}$. $\tilde{A}$ is assumed to have radial symmetry, i.e. dependency only on k_ρ and not on k_x or k_y. The generalized Sommerfeld integral S_n is defined in (4.14).

4.3 Spectral Domain Green Functions

Having already defined the spectral domain transformation in Section 4.2, (4.4) can be written in the spectral domain greatly simplifying the transverse derivatives. Then, the set of these differential equations is solved assuming δ excitations for the sources.

4.3.1 Electric and Magnetic Field Green Functions

Equations (4.4) derived in the previous section can be transformed to the spectral domain as follows:

$$\frac{\partial \tilde{\mathbf{E}}_t}{\partial z} = -j\omega\mu(\tilde{\mathbf{H}}_t \times \hat{z}) + \frac{1}{j\omega\epsilon} j\mathbf{k}_\rho (j\mathbf{k}_\rho \cdot (\tilde{\mathbf{H}}_t \times \hat{z})) - \frac{1}{j\omega\epsilon} j\mathbf{k}_\rho J_z - \tilde{\mathbf{M}}_t \times \hat{z} \tag{4.15a}$$

$$\frac{\partial \tilde{\mathbf{H}}_t}{\partial z} = j\omega\epsilon(\tilde{\mathbf{E}}_t \times \hat{z}) - \frac{1}{j\omega\mu} j\mathbf{k}_\rho (j\mathbf{k}_\rho \cdot (\tilde{\mathbf{E}}_t \times \hat{z})) - \frac{1}{j\omega\mu} j\mathbf{k}_\rho \tilde{M}_z + \tilde{\mathbf{J}}_t \times \hat{z} \tag{4.15b}$$

$$\tilde{E}_z = \frac{1}{j\omega\epsilon} j\mathbf{k}_\rho (\tilde{\mathbf{H}}_t \times \hat{z}) - \frac{1}{j\omega\epsilon} \tilde{J}_z \tag{4.15c}$$

$$\tilde{H}_z = -\frac{1}{j\omega\mu} j\mathbf{k}_\rho (\tilde{\mathbf{E}}_t \times \hat{z}) + \frac{1}{j\omega\mu} \tilde{M}_z \tag{4.15d}$$

The advantage of the spectral domain transformation is obvious in the previous equations. All the spatial derivatives have been replaced by vectorial products. However, a simple decomposition in the two transverse directions is not possible if $\tilde{\mathbf{E}}_t$ and $\tilde{\mathbf{H}}_t$ are projected on the initial $\hat{x}$ and $\hat{y}$ Cartesian coordinate system. The right way to further simplify these equations is to perform a rotation in the transverse coordinates, which will allow us to separate between TM ($\tilde{H}_z = 0$) and TE ($\tilde{E}_z = 0$) set of solutions.

The proper system of coordinates (u, v) that permits decoupling of the solutions in TM and TE modes is defined by $\hat{u} = \mathbf{k}_\rho / k_\rho$ and $\hat{v} = \hat{z} \times \hat{u}$ and is shown in Fig. 4.1. The rotation can be summarized through the following forward transformations:

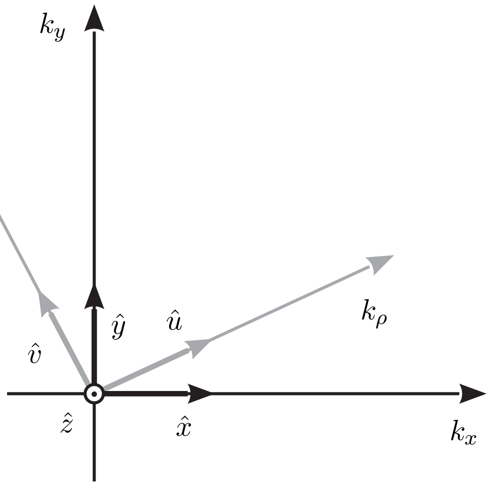

Figure 4.1: Rotated coordinate system in the spectral domain.

$$\hat{u} = \frac{k_x}{k_\rho}\hat{x} + \frac{k_y}{k_\rho}\hat{y} \tag{4.16}$$

$$\hat{v} = -\frac{k_y}{k_\rho}\hat{x} + \frac{k_x}{k_\rho}\hat{y} \tag{4.17}$$

and backward transformations of unitary vectors:

$$\hat{x} = \frac{k_x}{k_\rho}\hat{u} - \frac{k_y}{k_\rho}\hat{v} \tag{4.18}$$

$$\hat{y} = \frac{k_y}{k_\rho}\hat{u} + \frac{k_x}{k_\rho}\hat{v} \tag{4.19}$$

Applying this rotation, the previous equations become scalar and the TM and TE contributions can be written independently:

TM

$$\frac{\partial \tilde{E}_u}{\partial z} = -jk_z\frac{k_z}{\omega\epsilon}\tilde{H}_u - \frac{k_\rho}{\omega\epsilon}\tilde{J}_z - \tilde{M}_v \tag{4.20a}$$

$$\frac{\partial \tilde{H}_v}{\partial z} = -jk_z\frac{\omega\epsilon}{k_z}\tilde{E}_v - \tilde{J}_u \tag{4.20b}$$

$$\tilde{E}_z = \frac{k_\rho}{\omega\epsilon}\tilde{H}_v - \frac{1}{j\omega\epsilon}\tilde{J}_z \tag{4.20c}$$

TE

$$\frac{\partial \tilde{H}_u}{\partial z} = jk_z\frac{k_z}{\omega\mu}\tilde{E}_u - \frac{k_\rho}{\omega\mu}\tilde{M}_z + \tilde{J}_v \tag{4.21a}$$

$$\frac{\partial \tilde{E}_v}{\partial z} = jk_z\frac{\omega\mu}{k_z}\tilde{H}_u + \tilde{M}_u \tag{4.21b}$$

$$\tilde{H}_z = -\frac{k_\rho}{\omega\mu}\tilde{E}_v + \frac{1}{j\omega\mu}\tilde{M}_z \tag{4.21c}$$

If the source is defined, magnetic or electric current, transverse or vertical, then the two sets of equations (4.20) and (4.21) result in two decoupled second order differential equations of the normal components. The solution of these differential equations will provide the total EM fields in the spectral domain for certain excitations.

4.3.2 Electric and Magnetic Dipole Excitations

Assuming δ excitations for all the components of the electric and magnetic currents in (4.20) and (4.21), the normal electric and magnetic fields, i.e. $\tilde{E}_z$ and $\tilde{H}_z$ can be derived. As a δ

excitation has been assumed, the solutions of the normal fields coincide with the corresponding GFs, i.e. $\tilde{G}^{zi}_{EW}$ and $\tilde{G}^{zi}_{HW}$, $W \in \{J, M\}$ depending on the electric or magnetic type of the source and $i \in \{u, v, z\}$ or $i \in \{x, y, z\}$ indicating the direction of the source.

Assuming that the δ sources radiate in the unbounded space, the free space spectral domain GFs can be obtained and are shown in Tables 4.2 and 4.3 for electric and magnetic current excitations, respectively [107].

Electric Current Excitation	
$\tilde{G}^{zx}_{EJ} = \frac{-k_x}{4\pi\omega\epsilon} \mathrm{e}^{-jk_z\|z-z_0\|} \mathrm{sgn}(z - z_0)$	$\tilde{G}^{zx}_{HJ} = \frac{-k_y}{4\pi k_z} \mathrm{e}^{-jk_z\|z-z_0\|}$
$\tilde{G}^{zy}_{EJ} = \frac{-k_y}{4\pi\omega\epsilon} \mathrm{e}^{-jk_z\|z-z_0\|} \mathrm{sgn}(z - z_0)$	$\tilde{G}^{zy}_{HJ} = \frac{k_x}{4\pi k_z} \mathrm{e}^{-jk_z\|z-z_0\|}$
$\tilde{G}^{zz}_{EJ} = \frac{-k_\rho^2}{4\pi\omega\epsilon k_z} \mathrm{e}^{-jk_z\|z-z_0\|}$	$\tilde{G}^{zz}_{HJ} = 0$

Table 4.2: Free space spectral domain GFs of an electric current **J**.

Magnetic Current Excitation	
$\tilde{G}^{zx}_{EM} = \frac{k_y}{4\pi k_z} \mathrm{e}^{-jk_z\|z-z_0\|}$	$\tilde{G}^{zx}_{HM} = \frac{-k_x}{4\pi\omega\mu} \mathrm{e}^{-jk_z\|z-z_0\|} \mathrm{sgn}(z - z_0)$
$\tilde{G}^{zy}_{EM} = \frac{-k_x}{4\pi k_z} \mathrm{e}^{-jk_z\|z-z_0\|}$	$\tilde{G}^{zy}_{HM} = \frac{-k_y}{4\pi\omega\mu} \mathrm{e}^{-jk_z\|z-z_0\|} \mathrm{sgn}(z - z_0)$
$\tilde{G}^{zz}_{EM} = 0$	$\tilde{G}^{zz}_{HM} = \frac{-k_\rho^2}{4\pi\omega\mu k_z} \mathrm{e}^{-jk_z\|z-z_0\|}$

Table 4.3: Free space spectral domain GFs of a magnetic current **M**.

4.3.3 Spectral Domain Vector and Scalar Potential Green Functions

At this point, the magnetic currents $\mathbf{M}_t$ and M_z will be dropped, but we are able to obtain their contributions later on by applying the duality principles of Maxwell's equations [95].

We are able to connect the spectral domain GFs for the potentials with their electric and magnetic field counterparts:

$$\tilde{G}_A^{xx} = -\frac{\mu \tilde{G}_{HJ}^{zx}}{jk_y} \tag{4.22}$$

$$\tilde{G}_A^{yy} = -\frac{\mu \tilde{G}_{HJ}^{zy}}{jk_x} \tag{4.23}$$

$$k_\rho^2 \tilde{G}_A^{zx} = j\omega\mu\epsilon \tilde{G}_{EJ}^{zx} + \frac{k_x}{k_y}\mu \frac{\partial \tilde{G}_{HJ}^{zx}}{\partial z} \tag{4.24}$$

$$k_\rho^2 \tilde{G}_A^{zy} = j\omega\mu\epsilon \tilde{G}_{EJ}^{zy} + \frac{k_y}{k_x}\mu \frac{\partial \tilde{G}_{HJ}^{zy}}{\partial z} \tag{4.25}$$

$$k_\rho^2 \tilde{G}_A^{zz} = j\omega\mu\epsilon \tilde{G}_{EJ}^{zz} \tag{4.26}$$

and finally for the scalar potential G_V:

$$k_\rho^2 \tilde{G}_V^{x} = k_\rho^2 \tilde{G}_V^{y} = \frac{j\omega}{jk_x}\frac{\partial \tilde{G}_{EJ}^{zx}}{\partial z} - \frac{k^2}{j\epsilon k_y}\tilde{G}_{HJ}^{zx} \tag{4.27}$$

$$\tilde{G}_V^{z} = \frac{j\omega}{k_z'^2}\tilde{G}_{EJ}^{xx}(z', z) + \frac{j\omega}{k_z'^2}\frac{k_y}{k_x}\tilde{G}_{EJ}^{yx}(z', z) \tag{4.28}$$

It is useful to derive some inverse formulas relating electric and magnetic field GFs to potential GFs. Among them, the following are some of the most commonly needed:

$$\tilde{G}_{HJ}^{zx} = -\frac{jk_y}{\mu}\tilde{G}_A^{xx} \tag{4.29}$$

$$\frac{\partial \tilde{G}_{EJ}^{zx}}{\partial z} = \frac{k_x k_\rho^2}{\omega}\tilde{G}_V^{x} - \omega k_x \tilde{G}_A^{xx} \tag{4.30}$$

Finally, the following equations that relate potentials without involving field GFs are also valid:

$$\epsilon\mu \tilde{G}_V^{x} = \tilde{G}_A^{xx} + \frac{1}{jk_x}\frac{\partial \tilde{G}_A^{zx}}{\partial z} \tag{4.31}$$

$$\epsilon\mu \frac{\partial \tilde{G}_V^{x}}{\partial z} = \frac{\partial \tilde{G}_A^{xx}}{\partial z} - \frac{1}{jk_x}k_z^2 \tilde{G}_A^{zx} \tag{4.32}$$

$$\tilde{G}_V^{z} = -\frac{k_\rho^2}{k_z'^2}\tilde{G}_V^{x}(z', z) + \frac{\omega^2}{k_z'^2}\tilde{G}_A^{xx}(z', z), \tag{4.33}$$

where $k_z^2 = k^2 - k_\rho^2$.

4.3.4 Propagator Matrix and Terminating Conditions

In case of an arbitrary multilayered structure like the one in Fig. 4.2, the GFs need to be derived. A usual approach is to solve the equivalent transmission line systems [98]. Since we are going to introduce in the following sections conductive sheets and their corresponding boundary conditions, we choose hereby a method based on connecting the normal components of the EM fields through the different interfaces. This method is usually called Propagator Matrix technique [2].

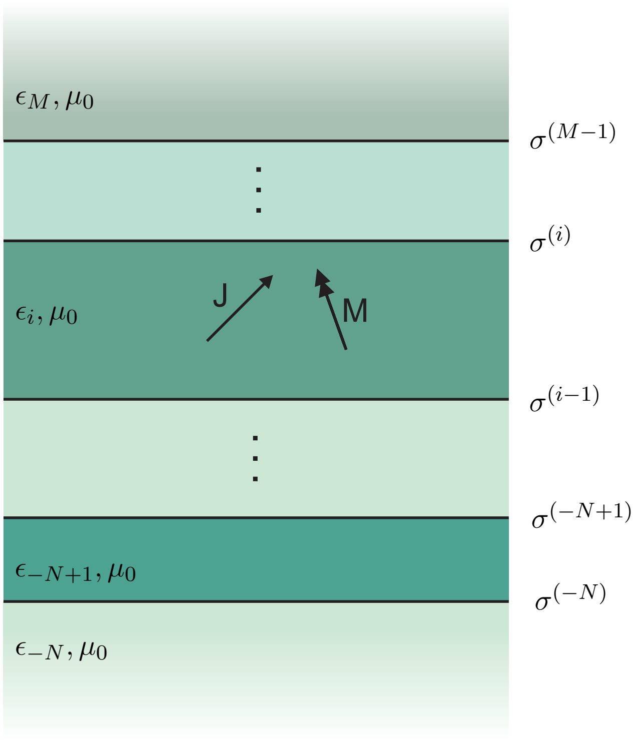

Figure 4.2: General multilayered structure with dielectric layers and conductive interfaces.

Dielectric layer without sources

In a dielectric layer, in the absence of sources, like the one in Fig. 4.3, the electric and magnetic fields must satisfy the homogeneous Helmholtz equation:

$$\nabla^2\Phi + k_{z\#i}^2\Phi = 0, \tag{4.34}$$

where Φ stands for any of the field components $\tilde{E}_{x,y,z}$ and $\tilde{H}_{x,y,z}$ and $k_{z\#i}$ represents the vertical propagation constant within the layer i. All the possible solutions of this equation can be summarized in the following matrix form, which connects the fields in the lower side of the dielectric with the ones on the top for the TM modes:

$$\begin{bmatrix} \tilde{E}_{z\#i}^{(i+1)} \\ \dfrac{\partial \tilde{E}_{z\#i}^{(i+1)}}{\partial z} \end{bmatrix} = \begin{bmatrix} \cos(k_{z\#i}d_i) & \dfrac{1}{k_{z\#i}}\sin(k_{z\#i}d_i) \\ -k_{z\#i}\sin(k_{z\#i}d_i) & \cos(k_{z\#i}d_i) \end{bmatrix} \begin{bmatrix} \tilde{E}_{z\#i}^{(i)} \\ \dfrac{\partial \tilde{E}_{z\#i}^{(i)}}{\partial z} \end{bmatrix} \tag{4.35}$$

and for the TE modes:

$$\begin{bmatrix} \tilde{H}_{z\#i}^{(i+1)} \\ \dfrac{\partial \tilde{H}_{z\#i}^{(i+1)}}{\partial z} \end{bmatrix} = \begin{bmatrix} \cos(k_{z\#i}d_i) & \dfrac{1}{k_{z\#i}}\sin(k_{z\#i}d_i) \\ -k_{z\#i}\sin(k_{z\#i}d_i) & \cos(k_{z\#i}d_i) \end{bmatrix} \begin{bmatrix} \tilde{H}_{z\#i}^{(i)} \\ \dfrac{\partial \tilde{H}_{z\#i}^{(i)}}{\partial z} \end{bmatrix} \tag{4.36}$$

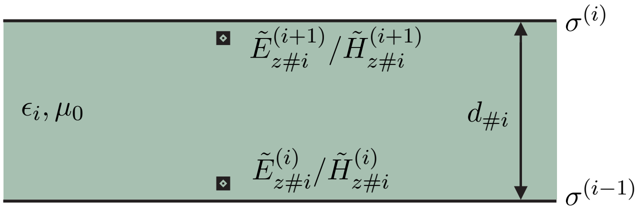
$\sigma^{(i)}$
$\tilde{E}_{z\#i}^{(i+1)}/\tilde{H}_{z\#i}^{(i+1)}$
ϵ_i, μ_0
$d_{\#i}$
$\tilde{E}_{z\#i}^{(i)}/\tilde{H}_{z\#i}^{(i)}$
$\sigma^{(i-1)}$

Figure 4.3: Propagation through a dielectric layer without sources.

Interface between different dielectrics

The connection between two different dielectrics is taken into account through the following matrices:

$$\begin{bmatrix} \tilde{E}_{z\#i+1}^{(i)} \\ \dfrac{\partial \tilde{E}_{z\#i+1}^{(i)}}{\partial z} \end{bmatrix} = \begin{bmatrix} \dfrac{\epsilon_i}{\epsilon_{i+1}} & 0 \\ 0 & 1 \end{bmatrix} \begin{bmatrix} \tilde{E}_{z\#i}^{(i)} \\ \dfrac{\partial \tilde{E}_{z\#i}^{(i)}}{\partial z} \end{bmatrix} \tag{4.37}$$

and

$$\begin{bmatrix} \tilde{H}_{z\#i+1}^{(i)} \\ \dfrac{\partial \tilde{H}_{z\#i+1}^{(i)}}{\partial z} \end{bmatrix} = \begin{bmatrix} 1 & 0 \\ 0 & 1 \end{bmatrix} \begin{bmatrix} \tilde{H}_{z\#i}^{(i)} \\ \dfrac{\partial \tilde{H}_{z\#i}^{(i)}}{\partial z} \end{bmatrix}, \tag{4.38}$$

for the TM and TE modes, respectively.

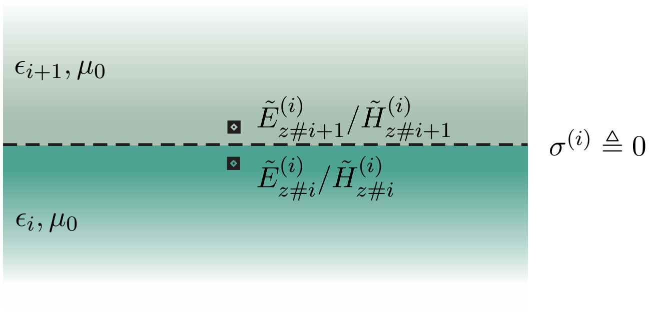
ϵ_{i+1}, μ_0
$\tilde{E}^{(i)}_{z\#i+1}/\tilde{H}^{(i)}_{z\#i+1}$
$\sigma^{(i)} \triangleq 0$
$\tilde{E}^{(i)}_{z\#i}/\tilde{H}^{(i)}_{z\#i}$
ϵ_i, μ_0

Figure 4.4: Propagation through an interface between two dielectric layers.

Open semi-infinite layer

All the components of the EM fields have to respect the Sommerfeld radiation condition at the semi infinite layer on the top and/or the bottom of the multilayered structure:

$$\lim_{r\to\infty} r(\frac{\partial\Phi}{\partial r} + jk\Phi) = 0, \tag{4.39}$$

Φ chosen among E_x, E_y, E_z, H_x, H_y or H_z. In case the semi-infinite layer is placed on the top of the multilayered structure, the following relations for the fields on the interface of Fig. 4.5 are valid:

$$\begin{bmatrix} 0 \end{bmatrix} = \begin{bmatrix} jk_{z\#M} & 1 \end{bmatrix} \begin{bmatrix} \tilde{E}^{(M-1)}_{z\#M} \\ \dfrac{\partial\tilde{E}^{(M-1)}_{z\#M}}{\partial z} \end{bmatrix} \tag{4.40}$$

$$\begin{bmatrix} 0 \end{bmatrix} = \begin{bmatrix} jk_{z\#M} & 1 \end{bmatrix} \begin{bmatrix} \tilde{H}^{(M-1)}_{z\#M} \\ \dfrac{\partial\tilde{H}^{(M-1)}_{z\#M}}{\partial z} \end{bmatrix} \tag{4.41}$$

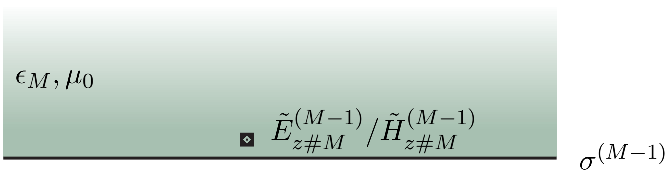
ϵ_M, μ_0
$\tilde{E}^{(M-1)}_{z\#M}/\tilde{H}^{(M-1)}_{z\#M}$
$\sigma^{(M-1)}$

Figure 4.5: Radiation from the upper semi-infinite medium.

If the semi-infinite layer is placed on the bottom of the multilayered structure, like in Fig. 4.6, the following terminating conditions are valid:

$$\begin{bmatrix}0\end{bmatrix} = \begin{bmatrix}-jk_{z\#-N} & 1\end{bmatrix}\begin{bmatrix}\tilde{E}^{(-N)}_{z\#-N} \\ \dfrac{\partial \tilde{E}^{(-N)}_{z\#-N}}{\partial z}\end{bmatrix} \tag{4.42}$$

$$\begin{bmatrix}0\end{bmatrix} = \begin{bmatrix}-jk_{z\#-N} & 1\end{bmatrix}\begin{bmatrix}\tilde{H}^{(-N)}_{z\#-N} \\ \dfrac{\partial \tilde{H}^{(-N)}_{z\#-N}}{\partial z}\end{bmatrix} \tag{4.43}$$

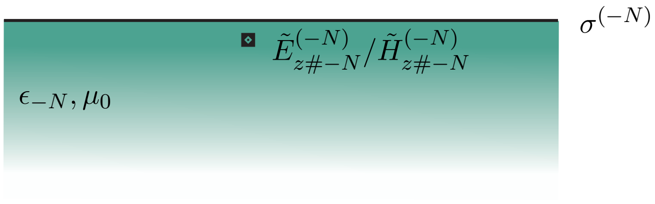

Figure 4.6: Radiation from the lower semi-infinite medium.

Surface impedance

If the multilayered structure is terminated by a surface impedance Z_s, the normal components of the electric and magnetic fields are directly connected through an approximate boundary condition, the Leontovich boundary condition [95]:

$$\hat{n} \times (\hat{n} \times \tilde{\mathbf{E}}) = -Z_s \hat{n} \times \tilde{\mathbf{H}} \tag{4.44}$$

If the lowest layer of the multilayered structure is backed by the surface impedance Z_s, the electric and magnetic field are connected as follows:

$$\begin{bmatrix}0\end{bmatrix} = \begin{bmatrix}jZ_s\omega\epsilon_{-N} & -1\end{bmatrix}\begin{bmatrix}\tilde{E}^{(-N-1)}_{z\#-N} \\ \dfrac{\partial \tilde{E}^{(-N-1)}_{z\#-N}}{\partial z}\end{bmatrix} \tag{4.45}$$

$$\begin{bmatrix}0\end{bmatrix} = \begin{bmatrix}\dfrac{j\omega\mu_0}{Z_s} & -1\end{bmatrix}\begin{bmatrix}\tilde{H}^{(-N-1)}_{z\#-N} \\ \dfrac{\partial \tilde{H}^{(-N-1)}_{z\#-N}}{\partial z}\end{bmatrix} \tag{4.46}$$

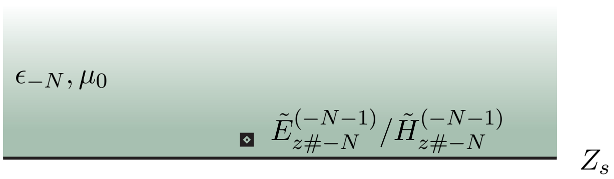

Figure 4.7: Surface impedance boundary condition on the lower layer.

If the top layer of the multilayered structure is backed by the surface impedance Z_s, the electric and magnetic field are connected as follows:

$$\begin{bmatrix} 0 \end{bmatrix} = \begin{bmatrix} jZ_s\omega\epsilon_M & 1 \end{bmatrix} \begin{bmatrix} \tilde{E}^{(M)}_{z\#M} \\ \dfrac{\partial \tilde{E}^{(M)}_{z\#M}}{\partial z} \end{bmatrix} \tag{4.47}$$

$$\begin{bmatrix} 0 \end{bmatrix} = \begin{bmatrix} \dfrac{j\omega\mu_0}{Z_s} & 1 \end{bmatrix} \begin{bmatrix} \tilde{H}^{(M)}_{z\#M} \\ \dfrac{\partial \tilde{H}^{(M)}_{z\#M}}{\partial z} \end{bmatrix} \tag{4.48}$$

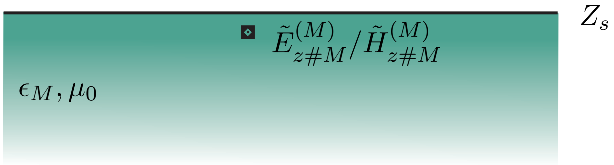

Figure 4.8: Surface impedance boundary condition on the upper layer.

If the impedance surface is a Perfect Electric Conductor (PEC), then $Z_s \to 0$. Consequently, from (4.47) and (4.48) it can be concluded that $\tilde{H}^{(-N-1)}_{z\#-N}$, $\partial\tilde{E}^{(-N-1)}_{z\#-N}/\partial z$, $\tilde{H}^{(M)}_{z\#M}$ and $\partial\tilde{E}^{(M)}_{z\#M}/\partial z$ are identically zero. On the contrary, if the impedance surface represents a Perfect Magnetic Conductor (PMC), then $Z_s \to \infty$ and $\tilde{E}^{(-N-1)}_{z\#-N}$, $\partial\tilde{H}^{(-N-1)}_{z\#-N}/\partial z$, $\tilde{E}^{(M)}_{z\#M}$ and $\partial\tilde{H}^{(M)}_{z\#M}/\partial z$ are now identically zero.

Excitation

The fields at the interfaces of the excitation layer $\tilde{E}^{(i+1)}_{z\#i}$, $\tilde{E}^{(i)}_{z\#i}$, $\tilde{H}^{(i+1)}_{z\#i}$ and $\tilde{H}^{(i)}_{z\#i}$ are connected to the excitation through the equations (4.49):

$$\tilde{E}^{(i+1)}_{z\#i} = A^{+}\cos(k_{z\#i}(z_{i+1}-z_0)) + A^{-}\sin(k_{z\#i}(z_{i+1}-z_0)) + \tilde{G}^{zm,exc}_{EJ}(z_{i+1}-z_0) \tag{4.49a}$$

$$\tilde{E}^{(i)}_{z\#i} = A^{+}\cos(k_{z\#i}(z_{i}-z_0)) + A^{-}\sin(k_{z\#i}(z_{i}-z_0)) + \tilde{G}^{zm,exc}_{EJ}(z_{i}-z_0) \tag{4.49b}$$

$$\tilde{H}^{(i+1)}_{z\#i} = B^{+}\cos(k_{z\#i}(z_{i+1}-z_0)) + B^{-}\sin(k_{z\#i}(z_{i+1}-z_0)) + \tilde{G}^{zm,exc}_{HJ}(z_{i+1}-z_0) \tag{4.49c}$$

$$\tilde{H}^{(i)}_{z\#i} = B^{+}\cos(k_{z\#i}(z_{i}-z_0)) + B^{-}\sin(k_{z\#i}(z_{i}-z_0)) + \tilde{G}^{zm,exc}_{HJ}(z_{i}-z_0) \tag{4.49d}$$

where z_0 is the position of the source and $m \in \{x, y, z\}$ the orientation of the source. The excitation GFs $\tilde{G}^{zm,exc}_{EJ}$ and $\tilde{G}^{zm,exc}_{HJ}$ are the free space GFs of a dipole that were derived in Section 4.3.2.

By properly cascading the different matrices developed in the previous sections the fields values and their normal derivatives are propagated through different interfaces and layers. The fields $\tilde{E}^{(i+1)}_{z\#i}$, $\tilde{H}^{(i+1)}_{z\#i}$ and their derivatives are connected through a terminating boundary condition, open space or surface impedance, in the upper layer. Similarly, the fields $\tilde{E}^{(i)}_{z\#i}$, $\tilde{H}^{(i)}_{z\#i}$ and their normal derivatives are connected through another terminating condition in the lower layer. Then, the proper number of equations is defined in order to solve for the four unknowns A^{+}, A^{-}, B^{+} and B^{-}. At this point, the spectral domain GFs of the multilayered structure of Fig. 4.2 have been obtained.

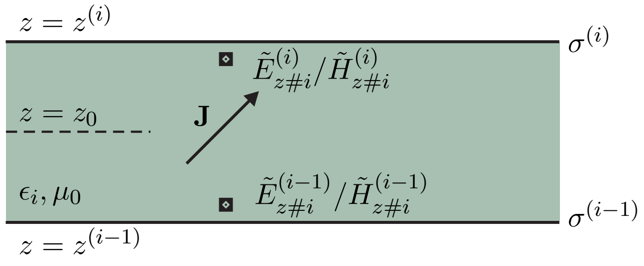
$z = z^{(i)}$
$\sigma^{(i)}$
$\tilde{E}^{(i)}_{z\#i}/\tilde{H}^{(i)}_{z\#i}$
$z = z_0$
J
ϵ_i, μ_0
$\tilde{E}^{(i-1)}_{z\#i}/\tilde{H}^{(i-1)}_{z\#i}$
$\sigma^{(i-1)}$
$z = z^{(i-1)}$

Figure 4.9: Dielectric layer with excitation.

4.4 Multilayered Structures with Thin Conductive Interfaces

All the matrices defined in the previous section remain valid in the presence of conductive sheets apart from the interface between the dielectrics. This block is hereby updated in order to accommodate the presence of a surface current between the two dielectrics. Both scalar and tensorial conductivities are taken into account.

4.4.1 Interface with scalar conductivity

The electric and magnetic fields on the two sides of a conductive sheet are connected through the following relationships:

$$\hat{n} \times (\tilde{\mathbf{E}}_2 - \tilde{\mathbf{E}}_1) = 0 \tag{4.50}$$

$$\hat{n} \times (\tilde{\mathbf{H}}_2 - \tilde{\mathbf{H}}_1) = \tilde{\mathbf{J}}_s = \sigma \hat{n} \times \tilde{\mathbf{E}}_{1,2}, \tag{4.51}$$

which state that the tangential electric field components are continuous through the interface. On the other hand, the tangential magnetic field components show a discontinuity at the interface, which is proportional to the electrical conductivity σ of the conductive sheet and the value of the tangential electric field at the interface.

Decomposing the tangential fields into the two orthogonal directions $\hat{u}$ and $\hat{v}$, the previous equations can be rewritten in scalar form:

$$\tilde{E}^{(1)}_{u2} = \tilde{E}^{(1)}_{u1} \tag{4.52}$$

$$\tilde{E}^{(1)}_{v2} = \tilde{E}^{(1)}_{v1} \tag{4.53}$$

$$\tilde{H}^{(1)}_{u2} - \tilde{H}^{(1)}_{u1} = \sigma \tilde{E}^{(1)}_{v1,2} \tag{4.54}$$

$$\tilde{H}^{(1)}_{v2} - \tilde{H}^{(1)}_{v1} = -\sigma \tilde{E}^{(1)}_{u1,2} \tag{4.55}$$

Decomposing in TM ($\tilde{E}_v = \tilde{H}_u = 0$) and in TE ($\tilde{E}_u = \tilde{H}_v = 0$) modes in the media below and above the conductive interface, the normal components of the electric and magnetic fields are related according to:

TM modes

$$\frac{\partial \tilde{E}^{(1)}_{z2}}{\partial z} = \frac{\partial \tilde{E}^{(1)}_{z1}}{\partial z} \tag{4.56}$$

$$\epsilon_2 \tilde{E}^{(1)}_{z2} - \epsilon_1 \tilde{E}^{(1)}_{z1} = -\sigma \frac{j}{\omega} \frac{\partial \tilde{E}^{(1)}_{z1,2}}{\partial z} \tag{4.57}$$

TE modes

$$\tilde{H}^{(1)}_{z2} = \tilde{H}^{(1)}_{z1} \tag{4.58}$$

$$\frac{\partial \tilde{H}^{(1)}_{z2}}{\partial z} - \frac{\partial \tilde{H}^{(1)}_{z1}}{\partial z} = \sigma j \omega \mu_0 \tilde{H}^{(1)}_{z1,2} \tag{4.59}$$

For a generalized multilayered structure, it is more convenient to reformulate the previous equations in matrix form which relate the normal fields and their normal derivatives in the medium $\#i$ below the interface (i) with the ones in the medium $\#i+1$.

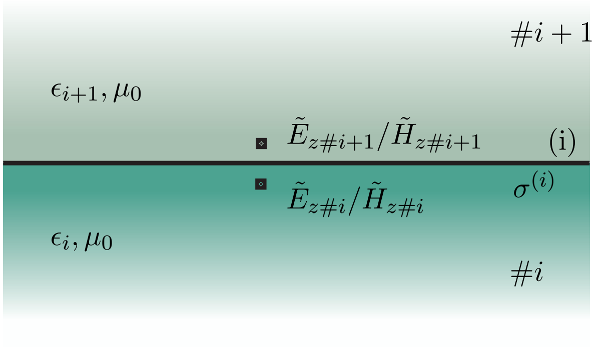
$\#i+1$
ϵ_{i+1}, μ_0
$\tilde{E}_{z\#i+1}/\tilde{H}_{z\#i+1}$
(i)
$\sigma^{(i)}$
$\tilde{E}_{z\#i}/\tilde{H}_{z\#i}$
ϵ_i, μ_0
$\#i$

Figure 4.10: Interface with scalar conductivity.

$$\begin{bmatrix} \tilde{E}^{(i+1)}_{z\#i+1} \\ \dfrac{\partial \tilde{E}^{(i+1)}_{z\#i+1}}{\partial z} \end{bmatrix} = \begin{bmatrix} \dfrac{\epsilon_{\#i}}{\epsilon_{\#i+1}} & -\dfrac{j\sigma^{(i)}}{\omega\epsilon_{\#i+1}} \\ 0 & 1 \end{bmatrix} \begin{bmatrix} \tilde{E}^{(i+1)}_{z\#i} \\ \dfrac{\partial \tilde{E}^{(i+1)}_{z\#i}}{\partial z} \end{bmatrix} \tag{4.60}$$

$$\begin{bmatrix} \tilde{H}^{(i+1)}_{z\#i+1} \\ \dfrac{\partial \tilde{H}^{(i+1)}_{z\#i+1}}{\partial z} \end{bmatrix} = \begin{bmatrix} 1 & 0 \\ \sigma^{(i)} j\omega\mu_0 & 1 \end{bmatrix} \begin{bmatrix} \tilde{H}^{(i+1)}_{z\#i} \\ \dfrac{\partial \tilde{H}^{(i+1)}_{z\#i}}{\partial z} \end{bmatrix} \tag{4.61}$$

4.4.2 Interface with tensorial conductivity

Some conductive layers may exhibit a tensorial electrical conductivity behavior. This means that the induced currents on the conductive layer do not behave the same way in the two main coordinates $\hat{u}$ and $\hat{v}$, defined in (4.16) and (4.17). In this case conductivity is not anymore a scalar value but is described by a tensor:

$$\bar{\bar{\sigma}} = \begin{bmatrix} \sigma_{uu} & \sigma_{uv} \\ \sigma_{vu} & \sigma_{vv} \end{bmatrix} \tag{4.62}$$

Apparently, the vectorial boundary conditions shown in the previous section are still valid, just the conductivity of the interface has to be treated as a tensor:

$$\hat{n} \times (\tilde{\mathbf{E}}_2 - \tilde{\mathbf{E}}_1) = 0 \tag{4.63}$$

$$\hat{n} \times (\tilde{\mathbf{H}}_2 - \tilde{\mathbf{H}}_1) = \tilde{\mathbf{J}}_s = \hat{n} \times \bar{\bar{\sigma}} \cdot \tilde{\mathbf{E}}_{1,2} \tag{4.64}$$

What needs to be updated is the scalar equations for the transverse fields, which in this case are developed as:

$$\tilde{E}^{(1)}_{u2} = \tilde{E}^{(1)}_{u1} \tag{4.65}$$

$$\tilde{E}^{(1)}_{v2} = \tilde{E}^{(1)}_{v1} \tag{4.66}$$

$$\tilde{H}^{(1)}_{u2} - \tilde{H}^{(1)}_{u1} = \sigma_{vu}\tilde{E}^{(1)}_{u1,2} + \sigma_{vv}\tilde{E}^{(1)}_{v1,2} \tag{4.67}$$

$$\tilde{H}^{(1)}_{v2} - \tilde{H}^{(1)}_{v1} = -\sigma_{uu}\tilde{E}^{(1)}_{u1,2} - \sigma_{uv}\tilde{E}^{(1)}_{v1,2} \tag{4.68}$$

The diagonal terms of $\bar{\bar{\sigma}}$, σ_{uv} and σ_{vu}, are responsible for the coupling of all the transverse components. Consequently, the decomposition in TM and TE modes that can be solved independently is not any more applicable. In other words, if only a TM mode is excited below the conductive interface, the tensorial conductivity will couple the TM excitation to a TE mode and a mix of TM and TE modes will coexist. Expressing the previous equations through their normal components and normal derivatives, we derive the following equations:

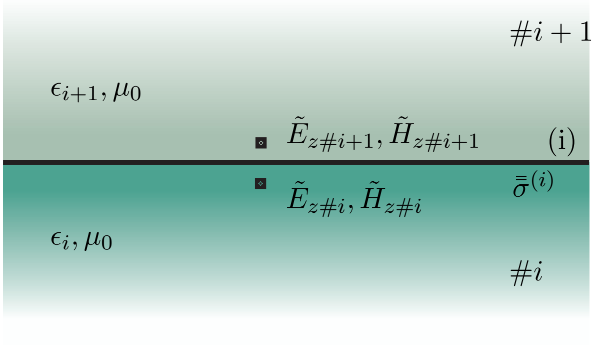
$\#i+1$
ϵ_{i+1}, μ_0
$\tilde{E}_{z\#i+1}, \tilde{H}_{z\#i+1}$
(i)
$\bar{\bar{\sigma}}^{(i)}$
$\tilde{E}_{z\#i}, \tilde{H}_{z\#i}$
ϵ_i, μ_0
$\#i$

Figure 4.11: Interface with tensorial conductivity.

$$\frac{\partial \tilde{E}^{(1)}_{z2}}{\partial z} = \frac{\partial \tilde{E}^{(1)}_{z1}}{\partial z} \tag{4.69}$$

$$\tilde{H}^{(1)}_{z2} = \tilde{H}^{(1)}_{z1} \tag{4.70}$$

$$\epsilon_2\tilde{E}^{(1)}_{z2} - \epsilon_1\tilde{E}^{(1)}_{z1} = -\sigma^{(1)}_{uu}\frac{j}{\omega}\frac{\partial \tilde{E}^{(1)}_{z1,2}}{\partial z} + \sigma^{(1)}_{uv}\mu_0\tilde{H}^{(1)}_{z1,2} \tag{4.71}$$

$$\frac{\partial \tilde{H}^{(1)}_{z2}}{\partial z} - \frac{\partial \tilde{H}^{(1)}_{z1}}{\partial z} = \sigma^{(1)}_{vu}\frac{\partial \tilde{E}^{(1)}_{z1,2}}{\partial z} + \sigma^{(1)}_{vv}j\omega\mu_0\tilde{H}^{(1)}_{z1,2} \tag{4.72}$$

Using the previous equations, we can write the generalized matrix to connect the fields below and above an interface with tensorial conductivity:

$$\begin{bmatrix} \tilde{E}^{(i+1)}_{z\#i+1} \\ \dfrac{\partial \tilde{E}^{(i+1)}_{z\#i+1}}{\partial z} \\ \tilde{H}^{(i+1)}_{z\#i+1} \\ \dfrac{\partial \tilde{H}^{(i+1)}_{z\#i+1}}{\partial z} \end{bmatrix} = \begin{bmatrix} \dfrac{\epsilon_{\#i}}{\epsilon_{\#i+1}} & -\dfrac{j\sigma^{(i)}_{uu}}{\omega\epsilon_{\#i+1}} & \dfrac{\mu_0\sigma^{(i)}_{uv}}{\epsilon_{\#i+1}} & 0 \\ 0 & 1 & 0 & 0 \\ 0 & 0 & 1 & 0 \\ 0 & \sigma^{(i)}_{vu} & j\omega\mu_0\sigma^{(i)}_{vv} & 1 \end{bmatrix} \begin{bmatrix} \tilde{E}^{(i+1)}_{z\#i} \\ \dfrac{\partial \tilde{E}^{(i+1)}_{z\#i}}{\partial z} \\ \tilde{H}^{(i+1)}_{z\#i} \\ \dfrac{\partial \tilde{H}^{(i+1)}_{z\#i}}{\partial z} \end{bmatrix} \tag{4.73}$$

Finally, we now have all the building blocks to construct the GFs for a general multilayered structure, with arbitrary excitation and conductive layers, either with scalar or tensorial electrical conductivity. It can be easily observed that if the conductivity $\sigma = 0$, then the classic building blocks of the propagator matrix are obtained.

4.4.3 Connecting 3D conductivity to 2D conductivity

Before approaching the infinitesimally thin conductive interface, a connection between the definitions of the bulky conductivity of a material (σ_{3D}) and the surface conductivity of a sheet (σ_{2D}) will be demonstrated. Let us imagine a layer (#2) which instead of a lossless dielectric is filled with a material that is described by its bulky conductivity σ_{3D}. Usually, the effect of the conductivity of a material on the EM fields is described by introducing losses in the dielectric, or in other words by allowing an imaginary part in the dielectric constant of the material of the layer #2:

$$\epsilon^{(2)} = \epsilon^{(20)} - j\frac{\sigma_{3D}}{\omega} \tag{4.74}$$

Assuming for simplicity the propagation of a TM mode, we are able to connect the vertical component of the electric field and its derivative in the lowest medium (#1) with the one on the top (#3):

$$\begin{bmatrix} \tilde{E}^{(3)}_{z\#3} \\ \dfrac{\partial \tilde{E}^{(3)}_{z\#3}}{\partial z} \end{bmatrix} = \begin{bmatrix} T_{(2)} \end{bmatrix} \begin{bmatrix} M_{\#2} \end{bmatrix} \begin{bmatrix} T_{(1)} \end{bmatrix} \begin{bmatrix} \tilde{E}^{(2)}_{z\#1} \\ \dfrac{\partial \tilde{E}^{(2)}_{z\#1}}{\partial z} \end{bmatrix}, \tag{4.75}$$

where

$$\begin{bmatrix} M_{\#2} \end{bmatrix} \triangleq \begin{bmatrix} M_{11} & M_{12} \\ M_{21} & M_{22} \end{bmatrix} = \begin{bmatrix} \cos kz_2 d_2 & \dfrac{1}{kz_2}\sin kz_2 d_2 \\ -kz_2 \sin kz_2 d_2 & \cos kz_2 d_2 \end{bmatrix} \tag{4.76}$$

$$\begin{bmatrix} T_{(2)} \end{bmatrix} = \begin{bmatrix} \dfrac{\epsilon_2}{\epsilon_3} & 0 \\ 0 & 1 \end{bmatrix} \tag{4.77}$$

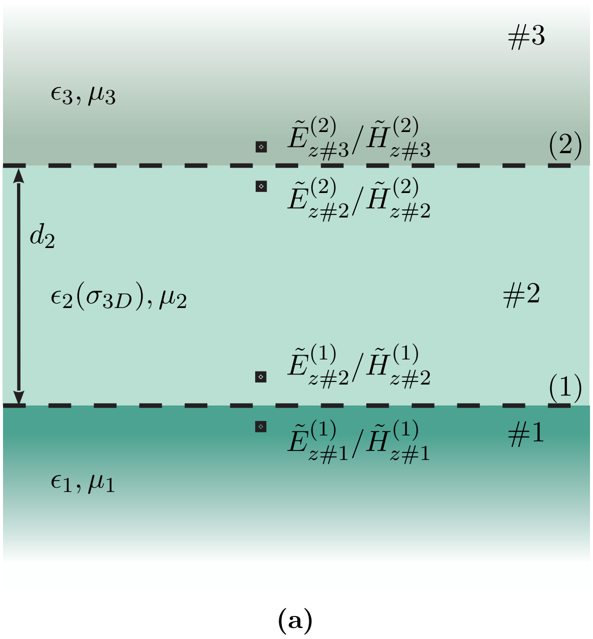
#3
ϵ_3, μ_3
$\tilde{E}^{(2)}_{z\#3}/\tilde{H}^{(2)}_{z\#3}$
(2)
$\tilde{E}^{(2)}_{z\#2}/\tilde{H}^{(2)}_{z\#2}$
d_2
$\epsilon_2(\sigma_{3D}), \mu_2$
#2
$\tilde{E}^{(1)}_{z\#2}/\tilde{H}^{(1)}_{z\#2}$
(1)
$\tilde{E}^{(1)}_{z\#1}/\tilde{H}^{(1)}_{z\#1}$
#1
ϵ_1, μ_1
(a)

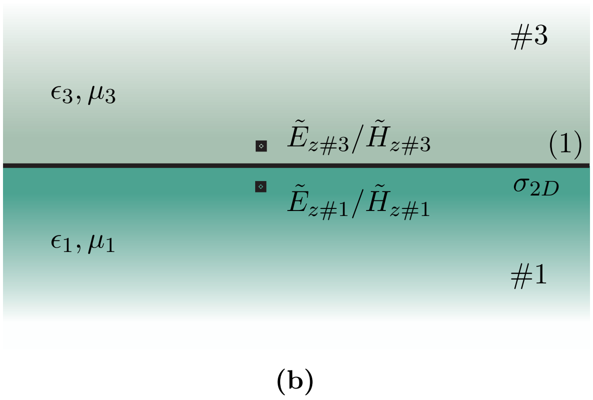
#3
ϵ_3, μ_3
$\tilde{E}_{z\#3}/\tilde{H}_{z\#3}$
(1)
σ_{2D}
$\tilde{E}_{z\#1}/\tilde{H}_{z\#1}$
ϵ_1, μ_1
#1
(b)

Figure 4.12: A dielectric layer with bulky conductivity σ_{3D} and thickness d_2 (a) and its limiting case of a conductive sheet with σ_{2D} when $d_2 \rightarrow 0$ (b).

$$\left[T_{(1)}\right] = \begin{bmatrix} \frac{\epsilon_1}{\epsilon_2} & 0 \\ 0 & 1 \end{bmatrix} \tag{4.78}$$

On the other hand, if a conductive interface with surface conductivity σ_{2D} between two media is considered, then the fields below and above the interface are connected as following:

$$\begin{bmatrix} \tilde{E}^{(1)}_{z\#3} \\ \frac{\partial \tilde{E}^{(1)}_{z\#3}}{\partial z} \end{bmatrix} = \left[\Sigma_{(1)}\right] \begin{bmatrix} \tilde{E}^{(1)}_{z\#1} \\ \frac{\partial \tilde{E}^{(1)}_{z\#1}}{\partial z} \end{bmatrix}, \tag{4.79}$$

where

$$\left[\Sigma_{(1)}\right] = \begin{bmatrix} \dfrac{\epsilon_1}{\epsilon_3} & -\dfrac{j\sigma_{2D}}{\omega\epsilon_3} \\ 0 & 1 \end{bmatrix} \tag{4.80}$$

Obviously, the two structures should exhibit exactly the same behavior, when $d_2 \to 0$. In other words:

$$\lim_{d_2 \to 0}\left(\left[T_{(2)}\right]\left[M_{\#2}\right]\left[T_{(1)}\right]\right) = \left[\Sigma_{(1)}\right] \tag{4.81}$$

From the previous matrix equation, the following set of equations can be derived:

$$\lim_{d_2 \to 0} M_{11} = \lim_{d_2 \to 0} \cos kz_2 d_2 = 1 \tag{4.82a}$$

$$\lim_{d_2 \to 0} \epsilon_2 M_{12} = \lim_{d_2 \to 0} \epsilon_2 \frac{\sin kz_2 d_2}{kz_2} = -\frac{j\sigma_{2D}}{\omega} \tag{4.82b}$$

$$\lim_{d_2 \to 0} \frac{\epsilon_1}{\epsilon_2} M_{21} = \lim_{d_2 \to 0} -\frac{\epsilon_1}{\epsilon_2} kz_2 \sin kz_2 d_2 = 0 \tag{4.82c}$$

$$\lim_{d_2 \to 0} M_{22} = \lim_{d_2 \to 0} \cos kz_2 d_2 = 1 \tag{4.82d}$$

Assuming that all the limits of (4.82) exist, then we deduce that $kz_2 d_2 \ll 1$ and consequently using the small angle approximation, we get $\sin kz_2 d_2 \simeq kz_2 d_2$. Then,

$$\lim_{d_2 \to 0} \epsilon_2 M_{12} = \lim_{d_2 \to 0} \epsilon_2 \frac{\sin kz_2 d_2}{kz_2} = \lim_{d_2 \to 0} \epsilon_2 d_2 = \lim_{d_2 \to 0} \epsilon^{(20)} d_2 - j\frac{\sigma_{3D}}{\omega} d_2 = -\lim_{d_2 \to 0} j\frac{\sigma_{3D}}{\omega} d_2 \triangleq -\frac{j\sigma_{2D}}{\omega} \tag{4.83}$$

Consequently,

$$\sigma_{2D} = \lim_{d \to 0} \sigma_{3D} d \tag{4.84}$$

Of course, (4.84) verifies also (4.82) and concludes the mathematical connection between σ_{3D} and σ_{2D}. From a more physical point of view, the conductivity of a thin metallic film will strongly depend on the thickness of the film. Indeed, it is reported that the electrical conductivity of sufficiently thin metal films (with the current in the plane of the film) is less than that of the bulk metal [108]. In this case, its value depends on the mean free path of the electrons. The basic theory for metal films can be found in Fuchs [109]. A simple approximation that is widely used within the material science community and takes into account the surface interaction of the molecules, is the Sondheimer's approach [110]:

$$\sigma_{3D} \propto 1 + \frac{3}{8}\frac{\lambda_0(1-p)}{d}, \tag{4.85}$$

being d the thickness of the thin film and p representing the surface scattering effects. This equation is fully compatible to the derived result in (4.84).

4.4.4 Mixed Potentials in the presence of conductive interfaces

Taking a look at the previous subsection, the tensorial nature of the conductive sheet couples the TM and TE modes, which cannot any more be solved independently. This results in an increased complexity in handling the GFs on the field level.

On the other hand, if we take a more careful look into the components of the vector and scalar potentials, we observe that by nature they consist of a mixture of TM and TE contributions within each dielectric layer. Consequently, the coupling between the TM and TE modes, implied by the tensorial nature of the conductive interface, is not expected to increase the number of the non zero components of the Mixed Potentials Green's Functions. The conductive layer will just complicate the algebraic connection of the potentials below and above the conductive interface.

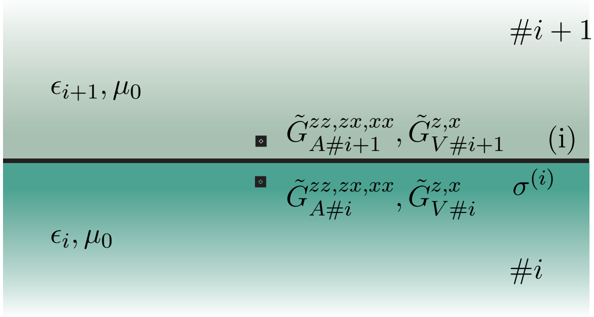
$\#i+1$
ϵ_{i+1}, μ_0
$\tilde{G}_{A\#i+1}^{zz,zx,xx}, \tilde{G}_{V\#i+1}^{z,x}$
(i)
$\tilde{G}_{A\#i}^{zz,zx,xx}, \tilde{G}_{V\#i}^{z,x}$
$\sigma^{(i)}$
ϵ_i, μ_0
$\#i$

Figure 4.13: Interface with mixed potentials

In order to shorten the formulas, layer $\#i$ is indicated as layer 1, while layer $\#i+1$ is replaced by layer 2.

$\tilde{\mathbf{G}}_{\mathbf{A}}^{\mathbf{zz}}$

$$\begin{bmatrix} \tilde{G}_{A2}^{zz(1)} \\ \dfrac{\partial \tilde{G}_{A2}^{zz(1)}}{\partial z} \end{bmatrix} = \begin{bmatrix} 1 & -\dfrac{j\sigma}{\omega\epsilon_1} \\ 0 & \dfrac{\epsilon_2}{\epsilon_1} \end{bmatrix} \begin{bmatrix} \tilde{G}_{A1}^{zz(1)} \\ \dfrac{\partial \tilde{G}_{A1}^{zz(1)}}{\partial z} \end{bmatrix} \tag{4.86}$$

$\tilde{\mathbf{G}}_{\mathbf{A}}^{\mathbf{xx}}$

$$\begin{bmatrix} \tilde{G}_{A2}^{xx(1)} \\ \dfrac{\partial \tilde{G}_{A2}^{xx(1)}}{\partial z} \end{bmatrix} = \begin{bmatrix} 1 & 0 \\ j\sigma\omega\mu_0 & 1 \end{bmatrix} \begin{bmatrix} \tilde{G}_{A1}^{xx(1)} \\ \dfrac{\partial \tilde{G}_{A1}^{xx(1)}}{\partial z} \end{bmatrix} \tag{4.87}$$

$\tilde{\mathbf{G}}_{\mathbf{A}}^{\mathbf{zx}}$

$$\begin{bmatrix} \tilde{G}_{A2}^{zx(1)} \\ \dfrac{\partial \tilde{G}_{A2}^{zx(1)}}{\partial z} \end{bmatrix} = \begin{bmatrix} \tilde{G}_{A1}^{zx(1)} \\ \dfrac{\partial \tilde{G}_{A1}^{zx(1)}}{\partial z} \end{bmatrix} + \begin{bmatrix} \dfrac{\sigma\mu_0}{\omega} \\ j\mu_0(\epsilon_2 - \epsilon_1) \end{bmatrix} k_x \tilde{G}_{V1}^{x(1)} \tag{4.88}$$

$\tilde{\mathbf{G}}_{\mathbf{V}}^{\mathbf{x}}$

$$\begin{aligned} k_x \begin{bmatrix} \tilde{G}_{V2}^{x(1)} \\ \epsilon_2 \dfrac{\partial \tilde{G}_{V2}^{x(1)}}{\partial z} \end{bmatrix} &= \begin{bmatrix} 1 & 0 \\ \dfrac{j\sigma}{\omega}[(\epsilon_1 + \epsilon_2)\omega^2\mu - k_\rho^2] & 1 \end{bmatrix} k_x \begin{bmatrix} \tilde{G}_{V1}^{x(1)} \\ \epsilon_1 \dfrac{\partial \tilde{G}_{V1}^{x(1)}}{\partial z} \end{bmatrix} \\ &+ \begin{bmatrix} 0 & 0 \\ -\dfrac{\omega^2}{j}(\epsilon_2 - \epsilon_1) & -\sigma\omega \end{bmatrix} \begin{bmatrix} \tilde{G}_{A1}^{zx(1)} \\ \dfrac{\partial \tilde{G}_{A1}^{zx(1)}}{\partial z} \end{bmatrix} \end{aligned} \tag{4.89}$$

The previous set of equations is very useful if we want to develop the Mixed Potential GFs for a generalized multilayered case. Knowing the scalar and vector potentials below the conductive layer, we connect them with the ones on the upper side of the conductive layer.

Advancing a bit, the boundary conditions for the GFs of the vector and scalar potentials are derived under the general case of the tensorial conductivity:

$\tilde{\mathbf{G}}_{\mathbf{A}}^{\mathbf{zz}}$

$$\begin{bmatrix} \tilde{G}_{A2}^{zz(1)} \\ \dfrac{\partial \tilde{G}_{A2}^{zz(1)}}{\partial z} \end{bmatrix} = \begin{bmatrix} 1 & -\dfrac{j\sigma_{uu}}{\omega\epsilon_1} \\ 0 & \dfrac{\epsilon_2}{\epsilon_1} \end{bmatrix} \begin{bmatrix} \tilde{G}_{A1}^{zz(1)} \\ \dfrac{\partial \tilde{G}_{A1}^{zz(1)}}{\partial z} \end{bmatrix} \tag{4.90}$$

$\tilde{\mathbf{G}}_{\mathbf{A}}^{\mathbf{xx}}$

$$\begin{bmatrix} \tilde{G}_{A2}^{xx(1)} \\ \dfrac{\partial \tilde{G}_{A2}^{xx(1)}}{\partial z} \end{bmatrix} = \begin{bmatrix} 1 & 0 \\ j\sigma_{vv}\omega\mu_0 + \dfrac{\omega\mu_0 k_x \sigma_{vu}}{jk_y} & 1 \end{bmatrix} \begin{bmatrix} \tilde{G}_{A1}^{xx(1)} \\ \dfrac{\partial \tilde{G}_{A1}^{xx(1)}}{\partial z} \end{bmatrix} + \begin{bmatrix} 0 \\ \dfrac{-\mu_0\sigma_{vu}k_\rho^2 k_x}{jk_y\omega} \end{bmatrix} \tilde{G}_{V1}^{x(1)} \tag{4.91}$$

$\tilde{\mathbf{G}}_{\mathbf{A}}^{\mathbf{zx}}$

$$\begin{bmatrix} \tilde{G}_{A2}^{zx(1)} \\ \dfrac{\partial \tilde{G}_{A2}^{zx(1)}}{\partial z} \end{bmatrix} = \begin{bmatrix} 1 & -\dfrac{\omega\mu_0}{jk_\rho^2}(\sigma_{vv} - \sigma_{uu} + \dfrac{k_y}{k_x}\sigma_{uv} - \dfrac{k_x}{k_y}\sigma_{vu}) \\ 0 & 1 \end{bmatrix} \begin{bmatrix} \tilde{G}_{A1}^{zx(1)} \\ \dfrac{\partial \tilde{G}_{A1}^{zx(1)}}{\partial z} \end{bmatrix}$$
$$+ \begin{bmatrix} \dfrac{\mu_0}{\omega}(\sigma_{uu} + \dfrac{k_x}{k_y}\sigma_{vu}) + \dfrac{\epsilon_1\mu_0^2\omega}{k_\rho^2}(\sigma_{vv} - \sigma_{uu} + \dfrac{k_y}{k_x}\sigma_{uv} - \dfrac{k_x}{k_y}\sigma_{vu}) \\ j\mu_0(\epsilon_2 - \epsilon_1) \end{bmatrix} k_x \tilde{G}_{V1}^{x(1)} \tag{4.92}$$

$\tilde{\mathbf{G}}_{\mathbf{V}}^{\mathbf{x}}$

$$k_x \begin{bmatrix} \tilde{G}_{V2}^{x(1)} \\ \epsilon_2 \dfrac{\partial \tilde{G}_{V2}^{x(1)}}{\partial z} \end{bmatrix} = \begin{bmatrix} 1 & 0 \\ \begin{array}{c} \dfrac{j}{\omega}[\mu\omega^2(\epsilon_1\sigma_{uu} + \epsilon_2\sigma_{uu} - \epsilon_1\dfrac{k_y}{k_x}\sigma_{uv} + \epsilon_2\dfrac{k_x}{k_y}\sigma_{vu}) - k_\rho^2\sigma_{uu} + \\ \dfrac{\epsilon_1\epsilon_2\mu^2\omega^4}{k_\rho^2}(\sigma_{vv} - \sigma_{uu} + \dfrac{k_y}{k_x}\sigma_{uv} - \dfrac{k_x}{k_y}\sigma_{vu})] \end{array} & 1 \end{bmatrix} k_x \begin{bmatrix} \tilde{G}_{V1}^{x(1)} \\ \epsilon_1 \dfrac{\partial \tilde{G}_{V1}^{x(1)}}{\partial z} \end{bmatrix}$$
$$+ \begin{bmatrix} 0 & 0 \\ -\dfrac{\omega^2}{j}(\epsilon_2 - \epsilon_1) & -\omega\sigma_{uu} + \omega\dfrac{k_y}{k_x}\sigma_{uv} - \dfrac{\omega^3\epsilon_2\mu}{k_\rho^2}(\sigma_{vv} - \sigma_{uu} + \dfrac{k_y}{k_x}\sigma_{uv} - \dfrac{k_x}{k_y}\sigma_{vu}) \end{bmatrix} \begin{bmatrix} \tilde{G}_{A1}^{zx(1)} \\ \dfrac{\partial \tilde{G}_{A1}^{zx(1)}}{\partial z} \end{bmatrix} \tag{4.93}$$

In Table 4.4 we summarize the continuity properties of the mixed potentials as the observer crosses an interface. It becomes obvious that the z-oriented components of the vector potential become discontinuous when the observer crosses a conductive sheet.

Potential GFs	Non-conductive interface	Conductive interface Scalar or Tensorial
G_A^{xx}	Continuous	Continuous
G_A^{zx}	Continuous	Discontinuous
G_A^{zz}	Continuous	Discontinuous
G_V^{ρ}	Continuous	Continuous
G_V^{z}	Continuous	Continuous

Table 4.4: Continuity properties of the mixed potentials as the observer crossed an interface.

4.4.5 Derivation of the Mixed Potentials GFs

The propagator matrix technique described for the normal fields in the previous section becomes quite challenging if we want to apply it to obtain the Mixed Potentials GFs. The reason for this is that the mixed potentials on the two sides of the dielectric interface (conductive or not) are not any more related through a single matrix that can be cascaded.

To overcome this difficulty, the proposed strategy is to develop the EM field GFs of the multilayered structure through the propagator matrix technique and afterwards apply for each set of observation and source points the following transformations between EM and potentials GFs for a horizontal excitation (assumed $\hat{x}$ directed) based on (4.22), (4.24) and (4.27):

$$\begin{bmatrix} \tilde{G}_A^{xx} \\ \tilde{G}_A^{zx} \\ \tilde{G}_V^{x} \end{bmatrix} = \begin{bmatrix} 0 & 0 & \dfrac{j\mu_0}{k_y} & 0 \\ \dfrac{j\omega\mu_0\epsilon}{k_\rho^2} & 0 & 0 & \dfrac{\mu_0 k_x}{k_\rho^2 k_y} \\ 0 & \dfrac{\omega}{k_\rho^2 k_x} & \dfrac{j\omega^2\mu_0}{k_\rho^2 k_y} & 0 \end{bmatrix} \begin{bmatrix} \tilde{G}_{EJ}^{zx} \\ \dfrac{\partial \tilde{G}_{EJ}^{zx}}{\partial z} \\ \tilde{G}_{HJ}^{zx} \\ \dfrac{\partial \tilde{G}_{HJ}^{zx}}{\partial z} \end{bmatrix} \tag{4.94}$$

and for a vertical excitation through (4.26), (4.33), (4.27) and (4.22):

$$\begin{bmatrix} \tilde{G}_A^{zz} \\ \tilde{G}_V^{z} \end{bmatrix} = \begin{bmatrix} \dfrac{j\omega\mu_0\epsilon}{k_\rho^2} & 0 \\ 0 & -\dfrac{\omega}{k_{z'}^2 k_x} \end{bmatrix} \begin{bmatrix} \tilde{G}_{EJ}^{zz} \\ \dfrac{\partial \tilde{G}_{EJ}^{zx}(z',z)}{\partial z'} \end{bmatrix}, \tag{4.95}$$

where the primed variables refer to the source point and its hosting layer and the unprimed ones to the observation point and its hosting layer.

Two different scalar potentials $\tilde{G}_V$ are defined within (4.94) and (4.95) depending on the orientation of the source. This contradicts the scalar nature of $\tilde{G}_V$, but it is inherent to the Sommerfeld's choice for the potentials [38]. Actually, $\tilde{G}_V$ represents the potential associated with a unit charge and a direction, mimicking a quasi dipole. Obviously, the oscillation in the transverse and the vertical direction result in different radiated fields and consequently two separate expressions for the scalar potential, i.e. $\tilde{G}_V^{x,y}$ and $\tilde{G}_V^{z}$ have to be defined.

4.5 Examples with high technological impact

The propagator matrix developed in Section 4.4 provides the spectral domain GFs for the fields for arbitrary multilayered structures. The spectral domain GFs for the potentials can be obtained afterwards through (4.94) and (4.95). This strategy will be used in order to analyze some multilayered structures that include conductive sheets and are of high scientific interest.

The first example includes a single conductive sheet floating in free space. If this conductive sheet is made out of graphene, then it can support the propagation of plasmon modes extremely confined on the sheet. The second example includes a dielectric slab, backed by

PEC with a conductive sheet on top of it. If the conductive sheet is a typical semiconductor, then such a structure represents a solar antenna. If it is replaced by graphene, it results in a graphene dielectric slab or equivalently in a graphene parallel plate waveguide consisting of two parallel graphene layers. In all examples, the poles for the most general case of tensorial conductivity are obtained. Additionally, all the components of the vector and scalar potentials for the case of scalar conductivity are provided. In the case of tensorial conductivity, only certain components are presented as the formulas become more complex to write down.

4.5.1 Single conductive sheet

Let us assume a conductive sheet on the interface between two semi-infinite dielectrics and a δ source excitation in the upper dielectric. The excitation may have arbitrary direction, as shown in Fig 4.14, but it will be decomposed in its vertical ($\hat{z}$) and transverse ($\hat{x}$ and $\hat{y}$) components.

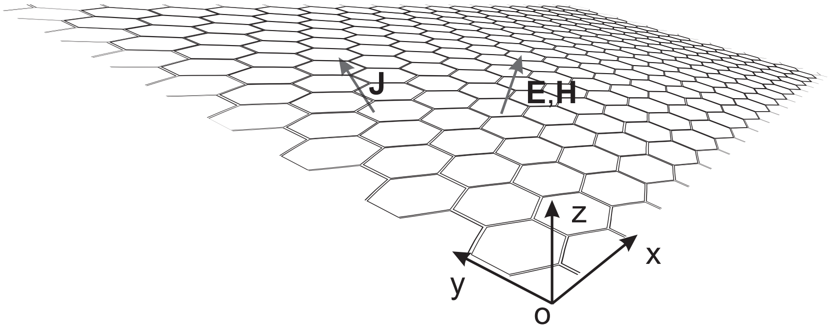

Figure 4.14: A conductive layer (in this case a graphene sheet) seperating two semi-infinite spaces.

Using the propagator matrix technique or by simply matching the boundary conditions on the conductive interface, the source excitation and the upper and lower layer radiation conditions, the closed form expressions for the GFs for the potentials of the structure shown in Fig. 4.15 both for horizontal and vertical excitations are derived and shown in Tables 4.5, 4.6, 4.7, 4.8 and 4.9.

src in #1	obs in #1	$z > z_0$	$\tilde{G}_A^{xx} = 2e^{-jk_{z1}z}\tilde{J}_x\mu_0\dfrac{-jk_{z1} + (k_{z2} + \mu_0\sigma\omega)\tan(k_{z1}z_0)}{k_{z1}D^{TE}}\cos(k_{z1}z_0)$
src in #1	obs in #1	$z < z_0$	$\tilde{G}_A^{xx} = 2e^{-jk_{z1}z_0}\tilde{J}_x\mu_0\dfrac{-jk_{z1} + (k_{z2} + \mu_0\sigma\omega)\tan(k_{z1}z)}{k_{z1}D^{TE}}\cos(k_{z1}z)$
src in #1	obs in #2	$z < z_0$	$\tilde{G}_A^{xx} = -2je^{jk_{z2}z}e^{-jk_{z1}z_0}\tilde{J}_x\mu_0\dfrac{1}{D^{TE}}$

Table 4.5: Closed-form expressions of $\tilde{G}_A^{xx}$ for a conductive sheet separating two semi-infinite media.

src in #1	obs in #1	$z > z_0$	$\tilde{G}_A^{zx} = je^{-jk_{z1}z}\tilde{J}_x k_x \mu_0 \frac{1}{2k_\rho^2}\big(3e^{jk_{z1}z_0} - e^{-jk_{z1}z_0}\frac{3D^{TE}D^{TM} - 2\epsilon_1 k_{z2}D^{TE} - 4k_{z1}D^{TM}}{D^{TM}D^{TE}}\big)$
src in #1	obs in #1	$z < z_0$	$\tilde{G}_A^{zx} = je^{-jk_{z1}z_0}\tilde{J}_x k_x \mu_0 \frac{1}{2k_\rho^2}\big(-3e^{jk_{z1}z} - e^{-jk_{z1}z}\frac{3D^{TE}D^{TM} - 2\epsilon_1 k_{z2}D^{TE} - 4k_{z1}D^{TM}}{D^{TM}D^{TE}}\big)$
src in #1	obs in #2	$z < z_0$	$\tilde{G}_A^{zx} = -je^{jk_{z2}z}e^{-jk_{z1}z_0}\tilde{J}_x k_x \mu_0 \; \frac{1}{k_\rho^2}\frac{2k_{z2}D^{TM} + \epsilon_2 k_{z1}D^{TE}}{D^{TM}D^{TE}}$

Table 4.6: Closed-form expressions of $\tilde{G}_A^{zx}$ for a conductive sheet separating two semi-infinite media.

src in #1	obs in #1	$z > z_0$	$\tilde{G}_A^{zz} = je^{-jk_{z1}z}\tilde{J}_z\mu_0\frac{e_1k_{z2}\omega + jk_{z1}(k_{z2}\sigma + \epsilon_2\omega)\tan(k_{z1}z_0)}{\omega k_{z1}D^{TM}}\cos(k_{z1}z_0)$
src in #1	obs in #1	$z < z_0$	$\tilde{G}_A^{zz} = je^{-jk_{z1}z_0}\tilde{J}_z\mu_0\frac{e_1k_{z2}\omega + jk_{z1}(k_{z2}\sigma + \epsilon_2\omega)\tan(k_{z1}z)}{\omega k_{z1}D^{TM}}\cos(k_{z1}z)$
src in #1	obs in #2	$z < z_0$	$\tilde{G}_A^{zz} = -je^{jk_{z2}z}e^{-jk_{z1}z_0}\tilde{J}_z\mu_0\frac{\epsilon_2}{D^{TM}}$

Table 4.7: Closed-form expressions of $\tilde{G}_A^{zz}$ for a conductive sheet separating two semi-infinite media.

src in #1	obs in #1	$z > z_0$	$\tilde{G}_V^x = -je^{-jk_{z1}z}\tilde{J}_x\frac{1}{k_\rho^2 k_{z1}}\big(-j\sin(k_{z1}z_0)\frac{k_\rho^2}{\epsilon_1} + e^{-jk_{z1}z_0}k_{z1}(\frac{k_{z1}k_{z2}}{D^{TM}} - \frac{\mu_0\omega^2}{D^{TE}})\big)$
src in #1	obs in #1	$z < z_0$	$\tilde{G}_V^x = -je^{-jk_{z1}z_0}\tilde{J}_x\frac{1}{k_\rho^2 k_{z1}}\big(-j\sin(k_{z1}z)\frac{k_\rho^2}{\epsilon_1} + e^{-jk_{z1}z}k_{z1}(\frac{k_{z1}k_{z2}}{D^{TM}} - \frac{\mu_0\omega^2}{D^{TE}})\big)$
src in #1	obs in #2	$z < z_0$	$\tilde{G}_V^x = -je^{jk_{z2}z}e^{-jk_{z1}z_0}\tilde{J}_x\omega\frac{1}{k_\rho^2}(\frac{k_{z1}k_{z2}}{\omega D^{TM}} - \frac{\mu\omega}{D^{TE}})$

Table 4.8: Closed-form expressions of $\tilde{G}_V^x$ for a conductive sheet separating two semi-infinite media.

src in #1	obs in #1	$z > z_0$	$\tilde{G}_V^z = je^{-jk_{z1}z}\tilde{J}_z\frac{\epsilon_1 k_{z2}\omega + jk_{z1}(k_{z2}\sigma + \epsilon_2\omega)\tan(k_{z1}z_0)}{\epsilon_1 k_{z1}\omega D^{TM}}\cos(k_{z1}z_0)$
src in #1	obs in #1	$z < z_0$	$\tilde{G}_V^z = je^{-jk_{z1}z_0}\tilde{J}_z\frac{\epsilon_1 k_{z2}\omega + jk_{z1}(k_{z2}\sigma + \epsilon_2\omega)\tan(k_{z1}z)}{\epsilon_1 k_{z1}\omega D^{TM}}\cos(k_{z1}z)$
src in #1	obs in #2	$z < z_0$	$\tilde{G}_V^z = je^{-jk_{z1}z}e^{jk_{z2}z_0}\tilde{J}_z\frac{k_{z2}}{k_{z1}D^{TM}}$

Table 4.9: Closed-form expressions of $\tilde{G}_V^z$ for a conductive sheet separating two semi-infinite media.

src in #1	obs in #1	$z > z_0$	$\tilde{G}_A^{xx} = 2e^{-jk_{z1}z}\tilde{J}_x\mu_0[-jk_{z1}\big(D^{TM}(\sigma_{uu}) - 0.5k_{z1}k_{z2}\frac{\sigma_{vu}}{\omega}\big)+$ $\big(D^{TM,TE}(\bar{\bar{\sigma}}) - k_{z1}D^{TM}(\sigma_{uu}) + 0.5k_{z1}^2k_{z2}\frac{\sigma_{uv}}{\omega}\big)\tan(k_{z1}z_0)]\frac{\cos(k_{z1}z_0)}{k_{z1}D^{TM,TE}(\bar{\bar{\sigma}})}$
src in #1	obs in #1	$z < z_0$	$\tilde{G}_A^{xx} = 2e^{-jk_{z1}z_0}\tilde{J}_x\mu_0[-jk_{z1}\big(D^{TM}(\sigma_{uu}) - 0.5k_{z1}k_{z2}\frac{\sigma_{vu}}{\omega}\big)+$ $\big(D^{TM,TE}(\bar{\bar{\sigma}}) - k_{z1}D^{TM}(\sigma_{uu}) + 0.5k_{z1}^2k_{z2}\frac{\sigma_{uv}}{\omega}\big)\tan(k_{z1}z)]\frac{\cos(k_{z1}z_0)}{k_{z1}D^{TM,TE}(\bar{\bar{\sigma}})}$
src in #1	obs in #2	$z < z_0$	$\tilde{G}_A^{xx} = -2je^{jk_{z2}z}e^{-jk_{z1}z_0}\tilde{J}_x\mu_0\frac{D^{TM}(\sigma_{uu}) - 0.5k_{z1}k_{z2}\frac{\sigma_{vu}}{\omega}}{D^{TM,TE}(\bar{\bar{\sigma}})}$

Table 4.10: Closed-form expressions of $\tilde{G}_A^{xx}$ for a conductive sheet separating two semi-infinite media with tensorial conductivity $\bar{\bar{\sigma}}$.

src in #1	obs in #1	$z > z_0$	$\tilde{G}_V^z = \quad je^{-jk_{z1}z}\tilde{J}_z[\epsilon_1 k_{z2}\omega\big(D^{TE}(\sigma_{vv}) - 2\mu\omega\sigma_{uv}\big)+$ $j\big(k_{z1}(k_{z2}\sigma_{uu} + \epsilon_2\omega)D^{TE}(\sigma_{vv}) + k_{z2}\mu\omega\sigma_{uv}(2\epsilon_1\omega - k_{z1}\sigma_{vu})\big)\tan(k_{z1}z_0)]\frac{\cos(k_{z1}z_0)}{\epsilon_1 k_{z1}\omega D^{TM,TE}(\bar{\bar{\sigma}})}$
src in #1	obs in #1	$z < z_0$	$\tilde{G}_V^z = \quad je^{-jk_{z1}z_0}\tilde{J}_z[\epsilon_1 k_{z2}\omega\big(D^{TE}(\sigma_{vv}\big) - 2\mu\omega\sigma_{uv})+$ $j\big(k_{z1}(k_{z2}\sigma_{uu} + \epsilon_2\omega)D^{TE}(\sigma_{vv}) + k_{z2}\mu\omega\sigma_{uv}(2\epsilon_1\omega - k_{z1}\sigma_{vu})\big)\tan(k_{z1}z_0)]\frac{\cos(k_{z1}z)}{\epsilon_1 k_{z1}\omega D^{TM,TE}(\bar{\bar{\sigma}})}$
src in #1	obs in #2	$z < z_0$	$\tilde{G}_V^z = je^{-jk_{z1}z}e^{jk_{z2}z_0}\tilde{J}_z\frac{k_{z2}\big(D^{TE}(\sigma_{vv}) - 2\mu\omega\sigma_{uv}\big)}{k_{z1}D^{TM,TE}(\bar{\bar{\sigma}})}$

Table 4.11: Closed-form expressions of $\tilde{G}_V^z$ for a conductive sheet separating two semi-infinite media with tensorial conductivity $\bar{\bar{\sigma}}$.

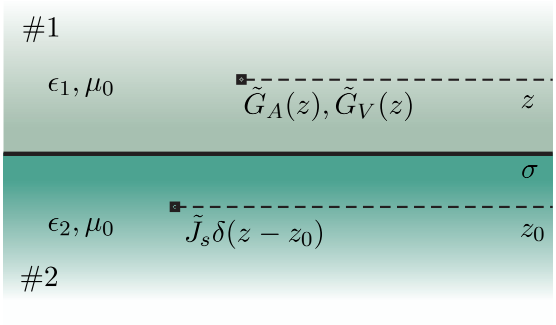

Figure 4.15: A conductive layer (in this case a graphene sheet) separating two semi-infinite spaces.

In all these formulas, $\tilde{J}_x$ and $\tilde{J}_z$ correspond to the surface of the Dirac δ function in the spectral domain. If a δ Dirac function with unit surface is assumed in the spatial domain, then $\tilde{J}_x = \tilde{J}_z = 1/2\pi$. Finally, the denominators $D^{TM}(\sigma)$ and $D^{TE}(\sigma)$ can be found in (4.96a) and (4.96b), respectively.

Two different set of poles appear in the equations of the Tables 4.5, 4.6, 4.7, 4.8 and 4.9. They are actually related to the TM and TE contributions and they can be summarized as:

$$D^{TM}(\sigma) = k_{z1}k_{z2}\frac{\sigma}{\omega} + \epsilon_2 k_{z1} + \epsilon_1 k_{z2} \tag{4.96a}$$

$$D^{TE}(\sigma) = k_{z1} + k_{z2} + \mu_0\sigma\omega \tag{4.96b}$$

If the conductivity is tensorial, then there are no more independent TM and TE modes, but a hybrid mixture of both of them:

$$D^{TM,TE}(\bar{\bar{\sigma}}) = D^{TM}(\sigma_{uu})D^{TE}(\sigma_{vv}) - k_{z1}k_{z2}\mu_0\sigma_{uv}\sigma_{vu} \tag{4.97}$$

The expressions for the GFs of the potentials become more complicated to be written down but not that difficult to be implemented. As a figure of merit, only $\tilde{G}_A^{xx}$ and $\tilde{G}_V^{z}$ are shown in Tables 4.10 and 4.11, respectively. The poles of $\tilde{G}_A^{xx}$ and $\tilde{G}_V^{z}$ for the case of the tensorial conductivity are the solutions of the coupled equation (4.97) and not any more the independent solutions of the TE and TM denominators of (4.96a) and (4.96b) found in the Tables 4.5 and 4.9, respectively [99]. If the tensorial conductivity $\bar{\bar{\sigma}}$ becomes scalar, i.e. $\sigma_{uu} = \sigma_{vv} = \sigma$ and $\sigma_{uv} = \sigma_{vu} = 0$, then the TE and TM modes are decoupled and the solutions for the casse of the scalar conductivity are retrieved (4.96). The Table 4.12 summarizes the contribution of the TM and TE parts in the denominators of the potential GFs.

The TM and TE poles, for the case that the upper and lower media are the same, are available in the literature as they can be obtained through the transmission line method [62]. The solutions of the equations $D^{TM} = 0$ and $D^{TE} = 0$, for the case of $k_{z1} = k_{z2}$ and $\epsilon_1 = \epsilon_2$

Potential GFs	σ ($\sigma = 0$ included)		$\bar{\bar{\sigma}}$
Type of poles	D^{TM}	D^{TE}	$D^{TM,TE}$
G_A^{xx}	No	Yes	Yes
G_A^{zx}	Yes	Yes	Yes
G_A^{zz}	Yes	No	Yes
G_V^{ρ}	Yes	Yes	Yes
G_V^{z}	Yes	No	Yes

Table 4.12: Contribution of TM and TE poles in multilayered structures with embedded sheets of scalar or tensorial conductivity.

coincide with the ones of (4.96), as in this case they allow for the following analytical solution:

$$k_\rho^{TM} = k\sqrt{1 - \left(\frac{2}{\eta\sigma}\right)^2} \tag{4.98}$$

$$k_\rho^{TE} = k\sqrt{1 - \left(\frac{\eta\sigma}{2}\right)^2}, \tag{4.99}$$

η being the impedance of the surrounding medium, i.e. $\eta = \sqrt{\frac{\epsilon}{\mu}}$. A requirement that the previous poles result in proper modes is that $\mathrm{Re}\{k_{\rho_p}\} > 0$ and $\mathrm{Im}\{k_{\rho_p}\} < 0$. Consequently, a proper TM pole exists if and only if $\mathrm{Im}\{\sigma\} < 0$, while a proper TE pole exists if and only if $\mathrm{Im}\{\sigma\} > 0$. The presence of such poles results in the existence and excitation of surface waves that remain conformed in the conductive interface between the dielectrics.

Graphene sheets (complex conductivity)

The requirement of $\mathrm{Im}\{\sigma\} < 0$ in order to support a proper TM wave is usually fulfilled by metals in the optical frequency range. This surface wave, called a surface plasmon polariton (SPP), remains extremely confined on the interface between the metal and the dielectric.

The surface charge density oscillations associated with the SPP can give rise to enhanced near-fields [6]. In lower than the optical frequencies, the SPP losses are so severe that a plasmon was never observed in structures made out of standard materials. The recent development of graphene [4] revealed its potentiality to support SPPs even at THz range [5] due to the negative imaginary part of its surface conductivity, shown in Fig. 4.16.

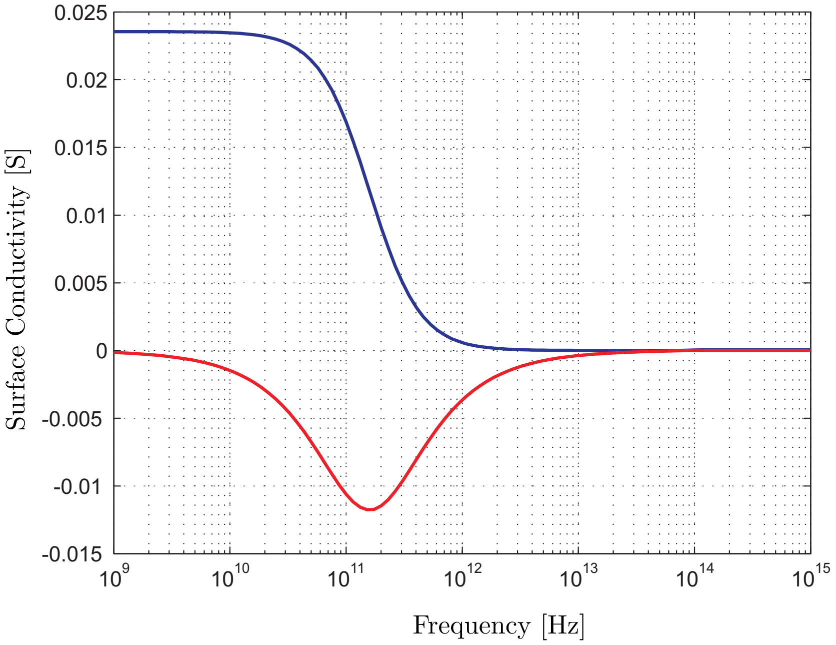

Figure 4.16: Real (blue line) and imaginary (red line) part of σ of a graphene sheet at 300K, at a chemical potential of 0.2eV and of relaxation time of 1ps using Kubo formula [111].

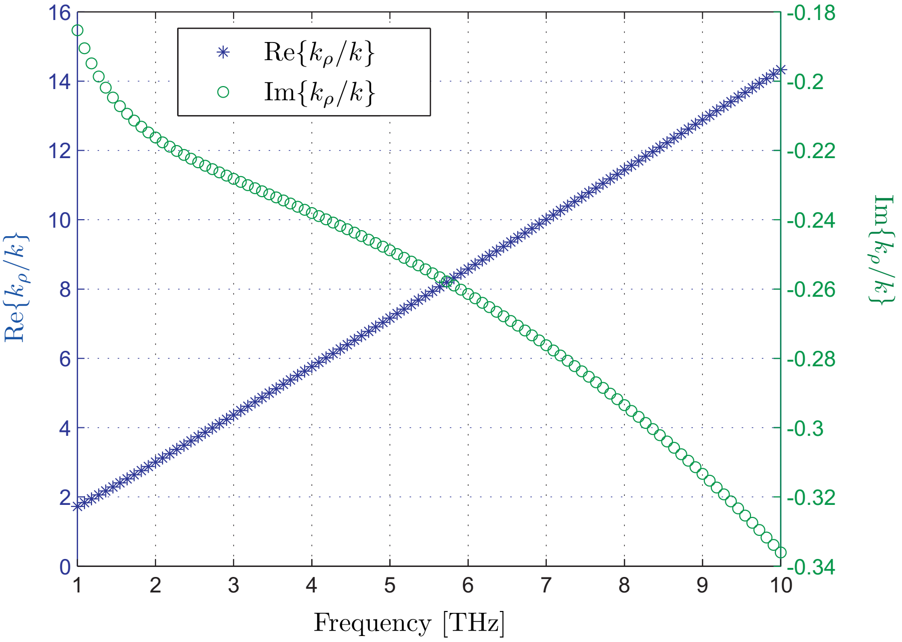

Figure 4.17: Real and imaginary part of the SPP propagating along a graphene sheet as indicated in (4.98). The graphene is set at 300^{o}K with a chemical potential of 0.2eV and a relaxation time of 1ps. The Kubo formula [111] was used for the conductivity of the graphene sheet.

The real and the imaginary part of the SPP pole, given by (4.98), are shown in Fig. 4.17 as a function of the excitation frequency.

As an alternative demonstration, the position of the SPP on the complex plane is shown in Fig. 4.18 for different frequencies. This representation of the pole position is quite popular in the classical textbooks analyzing dielectric slabs [2] where surface waves are supported and indicates that SPP and surface waves could potentially be handled using the same numerical tools that are proposed throughout this thesis.

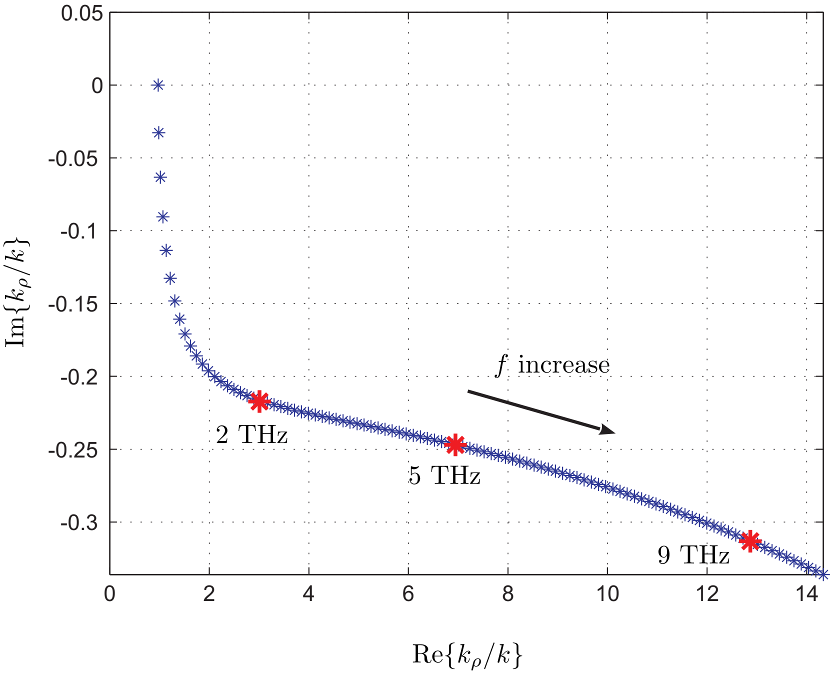

Figure 4.18: Position of the pole of the plasmon mode on the complex plane for a graphene layer floating in the air according to (4.98). The graphene is set at 300^{o}K with a chemical potential of 0.2eV and a relaxation time of 1ps. The Kubo formula [111] was used for the conductivity of the graphene sheet.

Since the above are first presented examples of a complete structure, the procedure for developing the mixed potential GFs can be verified. The GFs for the fields of a floating graphene layer can be found in the literature [101]. The very same problem, that is a graphene layer and a dipole source either vertically or horizontally on the top of the graphene sheeet, can be modeled using the mixed potentials. Through the vector and scalar potential, the total electric field created just below the graphene sheet can be calculated through the identity:

$$\mathbf{E} + j\omega\mathbf{A} = -\nabla V \tag{4.100}$$

This equation can be written also in terms of GFs, where we should be careful with the excitation of the scalar potential GF. In this case, the so-called $G_{V_{\mathrm{DIP}}}$ is created by an unitary electric dipole. Then, the following relations are valid:

$$\tilde{G}^{x}_{V_{\mathrm{DIP}}} = -\frac{jk_x}{j\omega}\tilde{G}^{x}_{V} \tag{4.101}$$

$$\tilde{G}^{z}_{V_{\mathrm{DIP}}} = \frac{1}{j\omega}\frac{\partial \tilde{G}^{z}_{V}}{\partial z'} \tag{4.102}$$

Splitting in $\hat{x}$ and $\hat{z}$ directed δ excitation, the normal component of the electric field should be given, respectively, by:

$$\mathrm{IFT}\{\tilde{G}^{zx}_{EJ}\} = -j\omega\mathrm{IFT}\{\tilde{G}^{zx}_{A}\} - \frac{\partial}{\partial z}\mathrm{IFT}\{\tilde{G}^{x}_{V_{\mathrm{DIP}}}\} \tag{4.103}$$

and

$$\mathrm{IFT}\{\tilde{G}^{zz}_{EJ}\} = -j\omega\mathrm{IFT}\{\tilde{G}^{zz}_{A}\} - \frac{\partial}{\partial z}\mathrm{IFT}\{\tilde{G}^{z}_{V_{\mathrm{DIP}}}\} \tag{4.104}$$

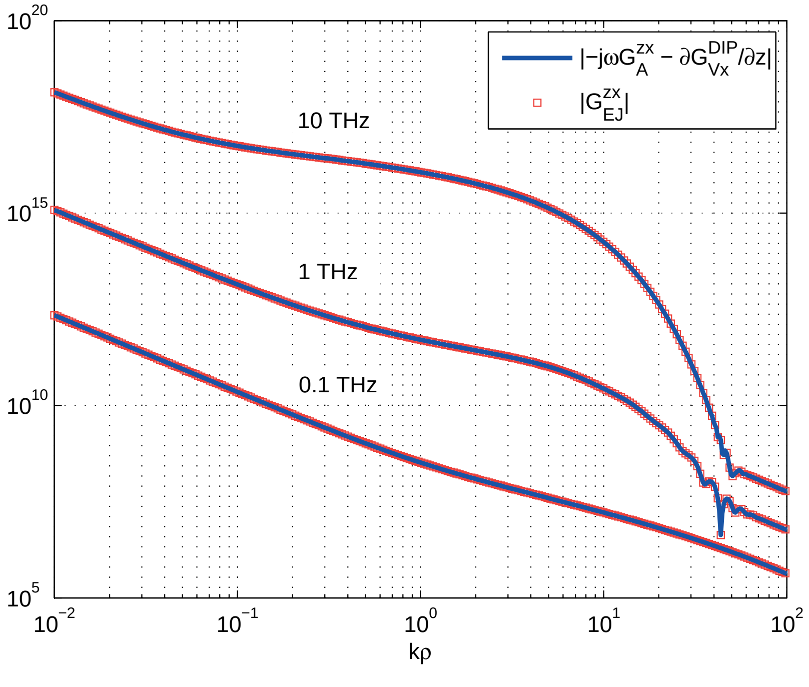

Figure 4.19: G^{zx}_{EJ} for different horizontal separations ρ between the source and the observation point. The horizontal source is placed on the upper side of the graphene sheet and the field is calculated on the lower side of the sheet. The GF is calculated both directly and through the mixed potentials yielding identical results.

As it can be seen in Figs. 4.19 and 4.20, the spatial domain GFs for the electric field are identical, either calculated directly as in [101] or through the mixed potentials. This is another

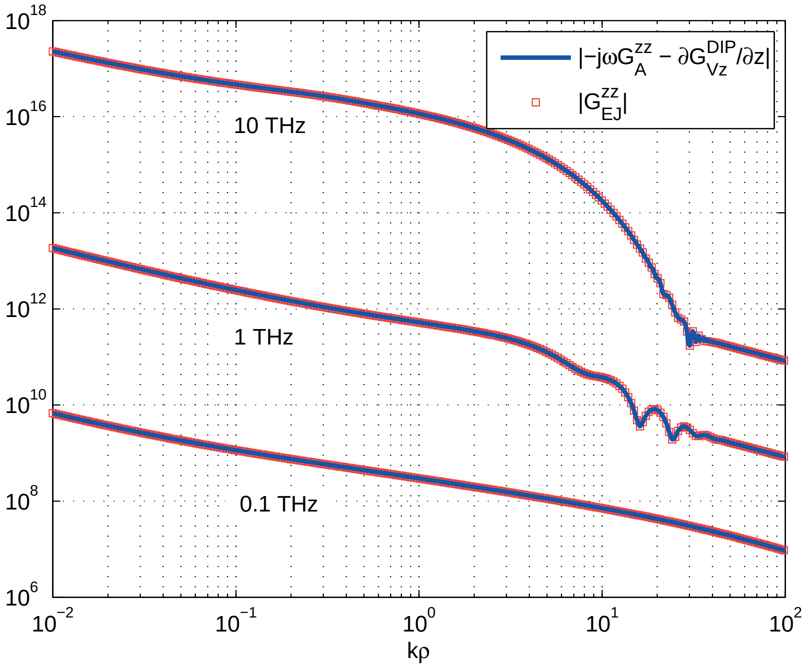

Figure 4.20: G_{EJ}^{zz} for different horizontal separations ρ between the source and the observation point. The vertical source is placed on the upper side of the graphene sheet and the field is calculated on the lower side of the sheet. The GF is calculated both directly and trough the mixed potentials yielding identical results.

practical proof, that the derivation of the mixed potentials as described in this chapter can be used, taking advantage of the weaker singularities that appear in the integrals of the MPIE compared to the EFIE. A novel efficient technique for calculating the spatial domain GFs through the IFTs of (4.103) and (4.104) will be presented in Chapter 6.

Some additional results for the GFs for the potentials are provided. Actually, it is the first time that such plots are available in literature [112]. The effect of the plasmon mode on the curves is the oscillations that are present at average horizontal distances. For small horizontal distances, the near field effect dominates, while for larger horizontal distances, the losses of the plasmonic mode are not any more present. Moreover, at relatively low frequencies, the plasmon mode has extremely large losses [113], and consequently the effect of the plasmon in the curves of $f = 1$ THz is not so intense and a behavior closer to the one of free space is obtained.

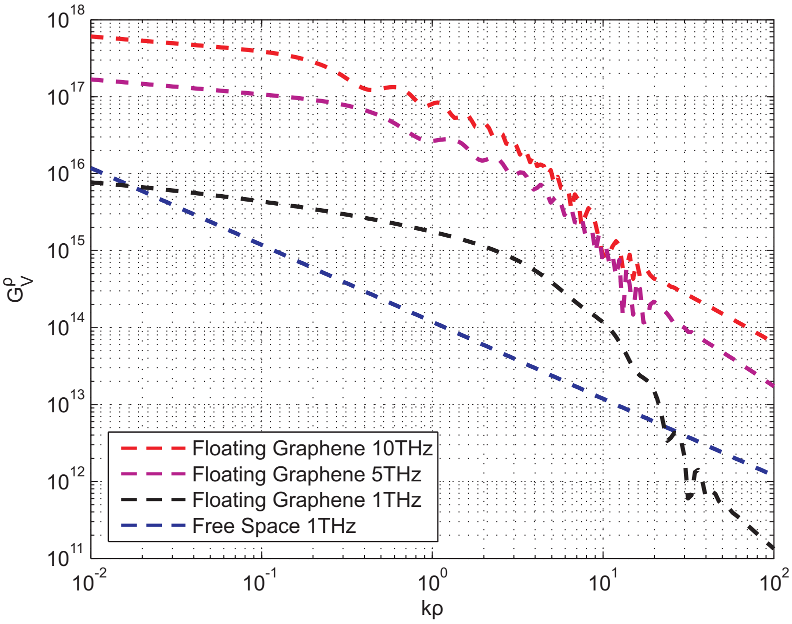

Figure 4.21: G_V^ρ of floating graphene sheet for different horizontal distances ρ and frequencies. The source and observation are located on the graphene sheet but on different sides.

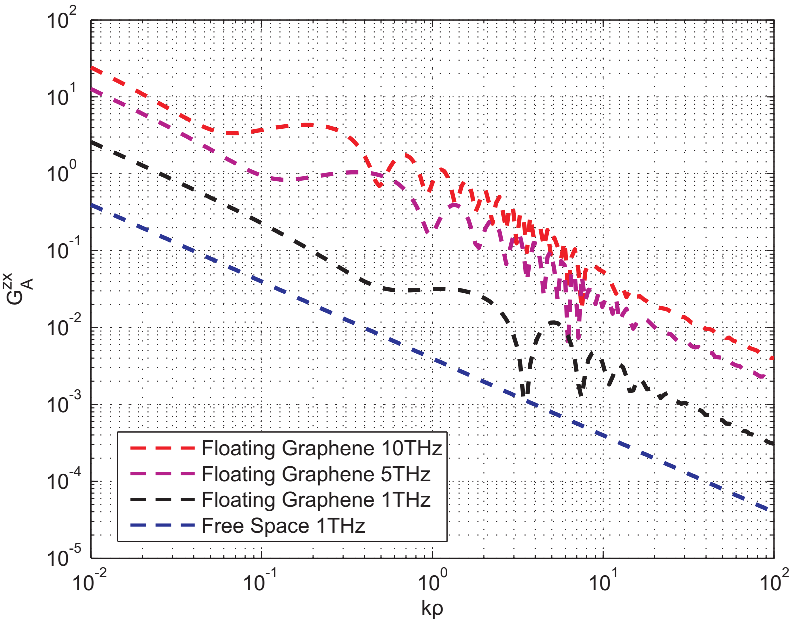

Figure 4.22: G_A^{zx} of floating graphene sheet for different horizontal distances ρ and frequencies. The source and observation are located on the graphene sheet but on different sides.

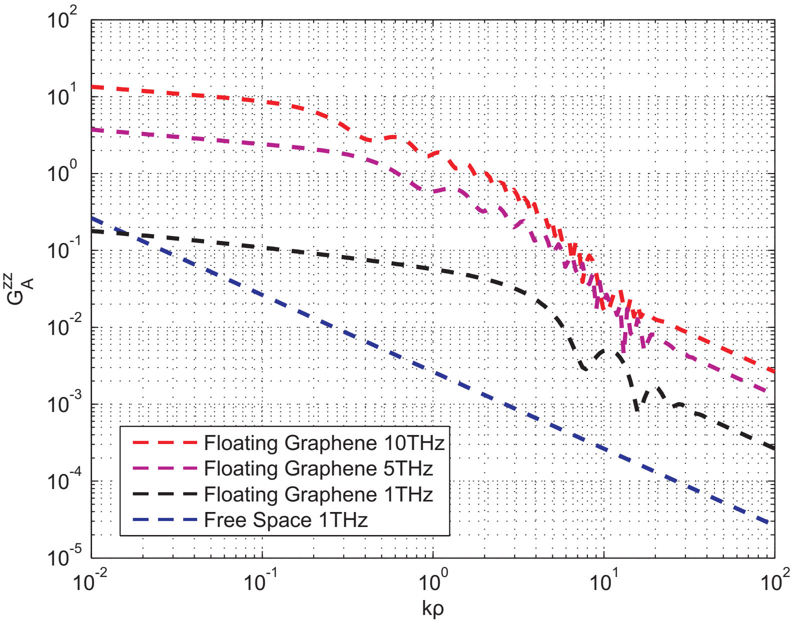

Figure 4.23: G_A^{zz} of floating graphene sheet for different horizontal distances ρ and frequencies. The source and observation are located on the graphene sheet but on different sides.

4.5.2 Grounded slabs

A big family of multilayered structures that has been widely analyzed and used is the grounded slab. In general, it comprises a dielectric slab of finite thickness with metallization on the one side. Hereby, three different types of grounded slabs are discussed. The first one is the classical grounded slab which serves as the substrate for a patch antenna. TM and/or TE surface waves may be supported depending on the parameters of the slab and the operating frequency. The second example is a grounded slab which is topped by a conductive sheet as shown in Fig. 4.24. If the conductivity of this sheet is assumed to be real valued, then it becomes the basic design of a solar antenna [3]. Also in this case only TM and/or TE surface waves can be supported. If the conductivity becomes imaginary, typically if the metallic sheet is a graphene layer, then apart from the TM/TE surface waves a surface plasmon mode will be present [114]. Finally, if the conductivity is tensorial, then all again hybrid TM/TE modes will be present.

Dielectric Slab

Classical ground slabs, which are backed with PEC on one side and open on the other as shown in Fig. 4.24 for $\sigma = 0$, have been extensively studied. If some metallization of a specific shape is added on top of them, then they work as patch antennas, famous for their planar profile, easy fabrication and compatibility with standard integrated circuits [1]. The

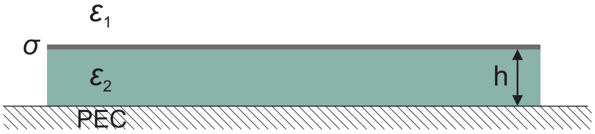

Figure 4.24: Grounded dielectric slab topped by a conductive sheet.

GFs of such structures can be found in classical CEM books [115], where the TM and TE poles are the solution of the following equations, where h denotes the thickness of the slab and the subindexes 1 and 2 refer to the semi-infinite medium and the substrate respectively:

$$D_{slab}^{TM} = k_{z1}\epsilon_2 + j\epsilon_1 k_{z2}\tan(k_{z2}h) \tag{4.105a}$$

$$D_{slab}^{TE} = k_{z2} + jk_{z1}\tan(k_{z2}h) \tag{4.105b}$$

Slab with a metallic sheet on the top

If the top side of the slab is covered by a metallic layer as in Fig. 4.24, the design of a solar antenna is retrieved. This is a very useful design for satellites because a solar panel and an antenna share the same surface. However, the presence of conductive layers on the top of the antenna will affect the performance its performance, therefore the solar antenna has to be designed very carefully. In the range of operating frequencies of such antennas, the solar panel metallic sheets can be considered as very thin [3, 116]. A very accurate simulation of such structures can be performed using the methods described in the current chapter.

Another example is a graphene sheet placed on the top of a dielectric slab. The GFs for the fields and the potentials will remain valid, just the values of the scalar conductivity will be complex. Obviously, a complex value for the conductivity is going to affect the position of the proper poles and under certain circumstances a plasmon mode will be able to propagate. Such a structure received a lot of interest recently, as the graphene sheet that supports the plasmon mode should be placed on a dielectric for structural purposes. Moreover, in order to apply an electric bias on the graphene sheet (a situation really desired as it reconfigures the properties of the graphene itself and consequently of the whole structure) a metallic back-end should exist below the dielectric support. As the plasmon remains quite confined on the graphene sheet, the ground plane will not really affect its propagation characteristics [117]. However, more and more nanoscale devices with graphene layers are developed where the ground plane has to be taken into account in the plasmonic propagation. Finally, such a configuration may also represent a parallel plate waveguide with the conductive walls made out of graphene, where a quasi-TEM mode is supported [118]. The analysis in [118] is based on the propagating modes, while the excitation of these modes can only be modeled through a GF based approach like the one presented hereby.

Based on the propagator matrix for the certain structure, the TM and TE poles can be found as:

$$D^{TM}_{slab}(\sigma) = k_{z1}\epsilon_2 + j(k_{z1}k_{z2}\frac{\sigma}{\omega} + \epsilon_1 k_{z2})\tan(k_{z2}h) \tag{4.106a}$$

$$D^{TE}_{slab}(\sigma) = k_{z2} + j(k_{z1} + \mu_0\sigma\omega)\tan(k_{z2}h) \tag{4.106b}$$

Similarly to the classical grounded dielectric slab, the subindexes 1 and 2 refer to the semi-infinite medium and the substrate, respectively, and h represents the thickness of the slab. It is easy to observe that if $\sigma \to 0$ the poles (4.105) are retrieved.

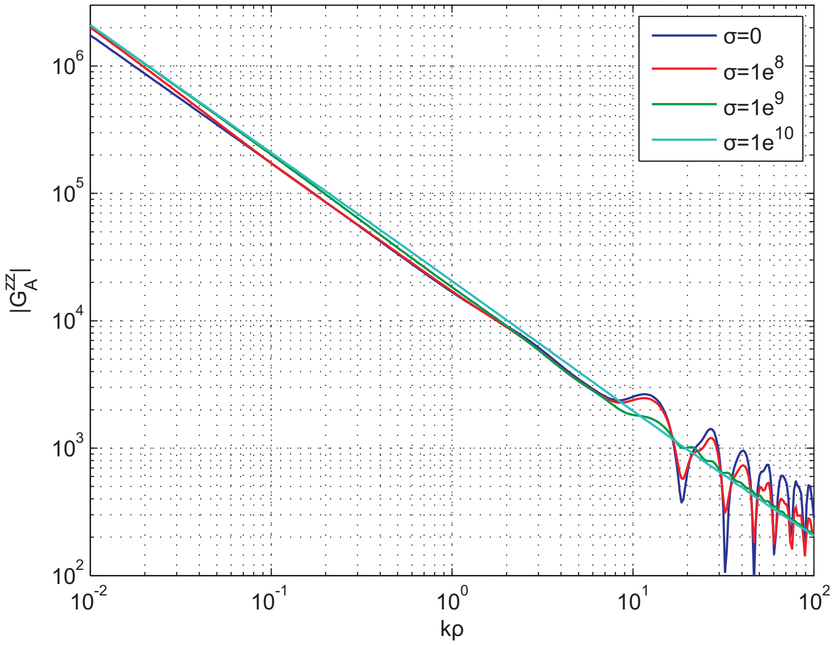

Figure 4.25: G_A^{zz} of the grounded slab of Fig. 4.24 with $\epsilon_2 = 5$ and thickness $h = \lambda$ at 1 THz topped by a sheet with a conductivity varying from 0 to very large values. Source and observation are placed on the top of the conductive sheet.

If the source is placed on the top of the conductive sheet (assumed to be at $z_0 = 0$), then, the vertical vector potential in the spectral domain $\tilde{G}_A^{zz}$ for $z > z_0$ is found to be:

$$\tilde{G}_A^{zz} = \frac{-j}{k_{z1}} \frac{\epsilon_2 k_{z1} + j k_{z1} k_{z2} \frac{\sigma}{\omega} \tanh\left(k_{z2}h\right)}{D^{TM}(\sigma)} e^{-jk_{z1}z} \tag{4.107}$$

The other components of the spectral domain mixed potential GFs can also be derived with the methods developed in this chapter in a straightforward way. However, they get very complicated forms to be written down and will be skipped from the current document.

As an example, the grounded slab of Fig. 4.24 with thickness $h = \lambda$ and permittivity $e_2 = 5$ is topped by a metallic sheet whose conductivity varies. A vertical electric dipole, oscillating at 1 THz is placed on the top of the metallic sheet. The vertical vector potential G_A^{zz} is calculated for different horizontal distances ρ on the top of the sheet, as shown in Fig. 4.25.

Under the condition that the conductivity of the sheet is sufficiently large, e.g $\sigma = 1e^{10}[S]$, the interface between the semi-infinite medium and the slab behaves like a PEC and the GF of a dipole in free space is retrieved (with double strength due to the image theory). If the conductivity vanishes, then the solutions of the dielectric slab are derived, with the surface waves being dominant in larger horizontal distances. If the conductivity varies between these limiting cases, a mixed behavior with surface waves present is obtained.

Finally, if the grounded slab is topped by a conductive sheet with tensorial conductivity $\bar{\bar{\sigma}}$, then the TM and TE poles are coupled. The solution of (4.108) will give the new poles. An example of such a design is a graphene sheet on the top of the grounded slab with a magnetic bias [114].

$$D_{slab}^{TE,TM}(\bar{\bar{\sigma}}) = D_{slab}^{TM}(\sigma_{uu})D_{slab}^{TE}(\sigma_{vv}) + k_{z1}k_{z2}\mu_0\sigma_{uv}\sigma_{vu}\tan^2(k_{z2}h) \tag{4.108}$$

The above equation agrees with the recent publication [119] if $\sigma_{uu} = \sigma_{vv} = \sigma_d$ and $\sigma_{uv} = -\sigma_{vu} = \pm\sigma_h$. However, (4.108) remains more general and can account for arbitrary conductivity tensors. The difficulty in (4.108) is the calculation of the poles, as this transcendental equation is very sensitive to the initial guess of the numerical root searching algorithms [63, 120, 121].

Moreover, if we suppose that $h \to \infty$, the effect of the PEC on the conductive interface should be minimized and the characteristic modes of the free standing conductive layer should be recovered. Indeed, recalling that $\tan(x) = -j\tanh(jx)$ and $\lim_{y\to\infty}\tanh(y) = 1$:

$$\lim_{h\to\infty} D_{slab}^{TM}(\sigma) = \lim_{h\to\infty} k_{z1}\epsilon_2 + (k_{z1}k_{z2}\frac{\sigma}{\omega} + \epsilon_1 k_{z2})\tanh(jk_{z2}h) = D^{TM}(\sigma) \tag{4.109a}$$

$$\lim_{h\to\infty} D_{slab}^{TM}(\sigma) = \lim_{h\to\infty} k_{z2} + (k_{z1} + \mu_0\sigma\omega)\tanh(jk_{z2}h) = D^{TE}(\sigma) \tag{4.109b}$$

$$\lim_{h\to\infty} D_{slab}^{TM,TE}(\bar{\bar{\sigma}}) = \lim_{h\to\infty} D_{slab}^{TM}(\sigma_{uu})D_{slab}^{TE}(\sigma_{vv}) - k_{z1}k_{z2}\mu_0\sigma_{uv}\sigma_{vu}\tanh^2(jk_{z2}h) = D^{TM,TE}(\bar{\bar{\sigma}}) \tag{4.109c}$$

4.6 Conclusion

A general procedure based on the propagator matrix technique to derive the spectral domain GFs has been presented. The multilayered structures may have arbitrary number of dielectric layers and conductive sheets. The conductivity of the sheets can be either of scalar or tensorial nature. The poles of simple structures that can be found in literature, most commonly obtained by the Transverse Resonant Method, coincide with the denominators of the corresponding GFs verifying the validity of our results. More complicated structures can now be easily modeled resulting in more accurate and delicate designs of microwave and THz applications. Last but not least, the mixed potential GFs for such problems are obtained for the first time, up to our knowledge, paving the way for an easier IE-MoM implementation. In order to provide the spatial domain counterparts of the GFs hereby presented, a novel and efficient numerical integration of the Sommerfeld integrals should be applied. This method will be analyzed in full details in the subsequent Chapter 6.

5 Double Exponential (DE) Quadrature Rule

In the previous Chapter 4, the spectral domain GFs for multilayered structures including conductive sheets were derived and discussed. Their derivation required tedious analytical calculations but no numerical approximations or evaluations. Actually, this is the advantage of the spectral domain approach for multilayered cases, that the GFs can be obtained in closed form. However, in order to calculate EM fields and solve EM problems through the MoM approach, briefly introduced in Chapter 3, the spatial domain GF have to be calculated through Sommerefeld integrals like the one presented in Table 4.1. These integrals, even for simple multilayered structures, have to be numerically evaluated. Discussion and novel techniques follow in Chapter 6. Additionally, as soon as the spatial domain GF are at hand, reaction integrals like the one that appear in (3.24) have to be calculated. Dedicated numerical algorithms for this purpose can be found in Chapter 7. All these subsequent numerical methods have a common ground. They need special numerical integration algorithms that can be applied efficiently to each one of these problems. For this reason, this chapter is dedicated to the introduction of a special integration technique that will be extensively used in the next chapters, the Double Exponential (DE) quadrature rule [122].

After a short introduction on the philosophy of the numerical integration (Section 5.1), common integration routines are presented in Section 5.2. Most of these routines fail when the functions to be integrated have some kind of singular behavior at some points, a very common fact in plenty of integrals appearing in CEM. This raises the need for a more specialized rule for such cases. A efficient solution for integrals with endpoint singularities is presented in Section 5.3, where the DE rule is introduced. Special details on the idea behind the DE rule are highlighted and, crucial for the performance of the algorithm, strategies are developed. A specific implementation of DE rule is provided, where if the accuracy of the numerical integration is not enough, all the computational effort done is not wasted but reused for the next more accurate iteration. Finally, hints for constructing various DE type quadrature rules are provided, depending on the specific properties of the functions to be integrated. Consequently, the DE rule can be modified accordingly in order to also fit in numerical techniques other than the ones presented in the current thesis.

5.1 Numerical Integration

Numerical integration has emerged as a very important aspect in all computational sciences, especially those which involve integro-differential operators. As the functions that can be analytically integrated are limited, plenty of well-known mathematicians, e.g. T.Simpson (1710-1761) and C.F. Gauss (1777-1855), have tried to develop numerical tools to derive the numerical value of the integration of a function over the domain (a, b):

$$I^{\text{exact}} = \int_a^b f(x)dx \tag{5.1}$$

The usual strategy approximates the exact solution of (5.1) as a finite summation of instances of the function $f(x)$, properly weighted:

$$I^{\text{approx}} = \sum_{i=1}^{N} w_i f(x_i) \tag{5.2}$$

The set comprising of the sampling points x_i and the corresponding weights w_i, $\{x_i, w_i\}$, define a so-called quadrature rule. Usually, the quadrature rules are developed over a reference integration domain, $x \in (-1, 1)$ being the most common case. Having calculated the proper sampling points and weights over the reference domain $\{x_i^{\text{Ref}}, w_i^{\text{Ref}}\}$, a quadrature rule for an arbitrary integration domain (a, b) becomes readily available through an affine transformation:

$$\begin{aligned} \int_a^b f(x)dx =& \frac{b-a}{2} \int_{-1}^{1} f(\frac{b-a}{2}x + \frac{b+a}{2})dx \\ \simeq& \frac{b-a}{2} \sum_{i=1}^{N} w_i^{\text{Ref}} f(\frac{b-a}{2}x_i^{\text{Ref}} + \frac{b+a}{2}) = \sum_{i=1}^{N} w_i f(x_i) \end{aligned} \tag{5.3}$$

Generally, (5.3) allows us to conclude the affine transformation that connects the quadrature rule over the domain (a, b) and the reference rule over the domain $(-1, 1)$:

$$\{x_i, w_i\} = \{\frac{b-a}{2}x_i^{\text{Ref}} + \frac{b+a}{2}, \frac{b-a}{2}w_i^{\text{Ref}}\} \tag{5.4}$$

In other words, the, most of the times, tedious computations to derive a quadrature rule $\{x_i, w_i\}$ are performed only once on the reference domain and the set of weights and points is stored. Each time that a numerical integration needs to be performed using a certain quadrature, a scale and shift of the set $\{x_i^{\text{Ref}}, w_i^{\text{Ref}}\}$ is enough to provide the appropriate updated quadrature rule at minimum computational expense. A strong recommendation is that the quadrature rule $\{x_i^{\text{Ref}}, w_i^{\text{Ref}}\}$ is calculated with higher precision arithmetic than the further calculations themselves. The more precise calculations add a lot of computational time, calls for specialized high precision libraries, but are performed only once and guaranty that all the significant digits at the nominal precision arithmetic are correct and they do not suffer from propagation errors in their less significant digits.

5.2 Interpolatory quadratures and singular integrals

The most common strategy to derive a quadrature rule is by approximating the integrand $f(x)$ with the sum of projections on interpolatory functions which can be integrated analytically. Depending on the set of the interpolatory functions chosen, different quadrature rules can be defined. More detailed and complete analysis on different quadrature rules can be found in classical numerical analysis textbooks like [123, 124].

Interpolation with orthogonal polynomials evaluated at equally spaced points yields the Newton-Cotes quadratures. If the chosen polynomials are piecewise constant, the midpoint rule is obtained, if they are piecewise linear, they result in the trapezoidal rule and if they are piecewise quadratic, the Simpson rule is obtained.

Another family of quadrature rules is derived, if a set of orthogonal polynomials is defined over the whole integration domain. These are the Gaussian quadratures and depending on the choice of the polynomial basis Gauss-Legendre, Gauss-Jacobi, Gauss-Chebyshev etc quadratures are defined. Gaussian quadratures are able to exactly integrate polynomials up to degree $2n-1$, n being the number of the integration points, multiplied with very specific weighting functions. Gaussian quadratures, in particular Gauss-Legendre (GL) quadrature rule, are widely used in computational science, even in cases when the integrands are strictly defined and can be integrated analytically on the paper, as with a relatively few integration points, they provide very accurate results.

The error estimate of an integration $\int_a^b f(x)dx$ through a GL quadrature is given by [125]:

$$\int_a^b f(x)dx = \sum_{i=1}^{N} w_i^{GL} f(x_i^{GL}) + \frac{(b-a)^{2n+1}(n!)^4}{(2n+1)[(2n)!]^3} f^{2n}(\xi), \tag{5.5}$$

where $\xi \in (a,b)$ and f^{2n} denotes the $2n^{th}$ derivative of f. It has to be pointed out that this error estimate is difficult to be evaluated numerically as higher order derivatives of the integrand need to be evaluated. However, from (5.5) it becomes clear that if the derivatives of the integrand are not bounded within the integration domain (a,b), even if the function $f(x)$ itself doesn't have singularities, the GL rule will lead to a very poor numerical approximation of the integral.

An example will be demonstrated for a better understanding of the performance of the Gaussian quadrature. The function to be integrated is $x\log x$ over the domain $x \in (0,1)$. The function itself doesn't have any singularities as shown in Fig. 5.1 and can be integrated analytically:

$$\int_0^1 x \log x dx = -\frac{1}{4}, \tag{5.6}$$

the absolute value of the integration corresponds to the shaded area of Fig. 5.1. The error of the numerical integration (5.6) using a GL quadrature rule is shown in Fig. 5.2 for different number of integration points. The slow convergence, that is due to the unbounded higher order derivatives of the integrand, results in unaffordable amount of computations in order to derive an accurate result. The ideal performance of a suitable quadrature rule (calculated with double-precision arithmetic) is also shown in Fig. 5.2 for comparison purposes. Additional quadrature rules have been developed to accommodate certain types of singularities of the integrand. They form the Gauss-Jacobi (GJ) quadratures, which can efficiently evaluate the following integrals:

$$\int_{-1}^1 f(x)(1-x)^{\alpha}(1+x)^{\beta}dx, \tag{5.7}$$

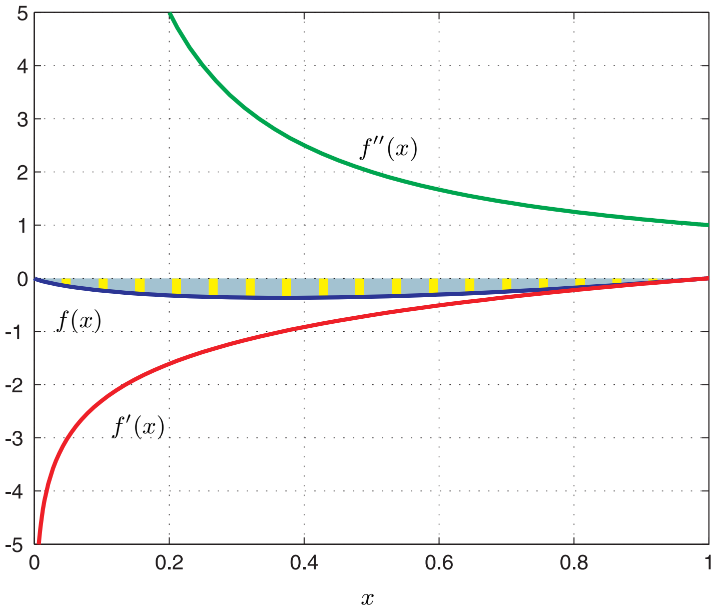

Figure 5.1: Plot of $f(x) = x \log x$, its first and second derivatives over the domain $x \in (0, 1)$. The surface of the shaded area is 0.25, corresponding to the value of the integral of $f(x)$ over the predefined domain (5.6).

where $f(x)$ is a smooth function for $x \in [-1, 1]$ and $\alpha, \beta > -1$. However, if the irregularity of the initial integrand cannot be completely isolated in the terms $(1-x)^\alpha(1+x)^\beta$, then even the GJ quadrure will have a poor behavior similar to the one of GL in Fig. 5.2.

Consequently, scientists were seeking for a quadrature rule that would be able to integrate efficiently functions with arbitrary singularities at the end points of the integration domain. Such a rule is the Double Exponential quadrature and its development and properties are described in details in the following sections.

5.3 Developing the DE transformation

The Double Exponential (DE) rule, developed during the seventies by Takahasi and Mori [122], serves as a general purpose quadrature rule for integrals with arbitrary endpoint singularities. The basic strategy is to transform the finite domain into an infinite one in such a way that the singularities are send to infinity in the transformed domain. If the transformation poses a strong decay at infinity, the singularities will be killed by the transformation and the infinite interval could possibly be truncated with no noticeable loss of accuracy.

One of the keystones towards the development of DE was the mathematical proof that for the numerical integration of an analytical function over $(-\infty, \infty)$ the trapezoidal rule with an equal mesh size is asymptotically optimal among formulas with the same density of sampling points [126]. Having this argument at hand, Takahasi and Mori were seeking for a proper transformation $\phi(t)$ that maps a finite integration domain, assumed here the reference domain

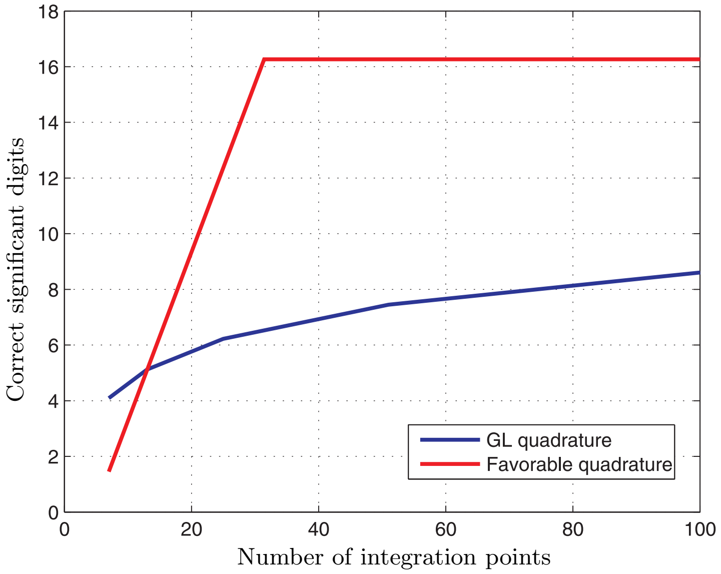

Figure 5.2: Gauss Legendre (GL) performance for the integration of the sample function $x \log x$. The ideal behavior of a quadrature rule is also shown for comparison purposes.

$(-1, 1)$, to the infinite domain $(-\infty, \infty)$. If $f(x)$ is the function to be integrated:

$$I^f = \int_{-1}^{1} f(x)dx \tag{5.8}$$

the transformation function $\phi(t)$ should be analytic $\forall t \in (-\infty, \infty)$ and satisfy the proper boundary properties:

$$\phi(-\infty) = -1 \tag{5.9}$$

$$\phi(\infty) = 1 \tag{5.10}$$

Under these conditions (5.8) can be written as:

$$I^f = \int_{-\infty}^{\infty} f(\phi(t))\phi'(t)dt \tag{5.11}$$

The transformed integral (5.11) is discretized using the trapezoidal rule following its optimality argument [126]:

$$I^f = h \sum_{k=-\infty}^{\infty} f(\phi(kh))\phi'(kh) + \mathrm{E}^{\mathrm{discr}} \tag{5.12}$$

where the discretization error is given by $\mathrm{E}^{\mathrm{discr}} = O(e^{-\frac{2\pi d}{h}})$, h being the separation distance of the trapezoidal rule between the sampling points and d the minimum distance between the singular points of $f(\phi(t))\phi'(t)$ and the real axis [127].

Additionally, in order to derive a handful numerical tool, a truncation of the infinite series has to be performed at some moderate value of $k = \pm n$, introducing an additional truncation error $\mathrm{E}^{\mathrm{trunc}}$:

$$I^f = h \sum_{k=-n}^{n} f(\phi(kh))\phi'(kh) + \mathrm{E}^{\mathrm{discr}} + \mathrm{E}^{\mathrm{trunc}} \tag{5.13}$$

If the transformation $x = \phi(t)$ makes the decay of the transformed integrand too fast, then the mesh size h will not be sufficiently small to catch the variations of the integrand and $\mathrm{E}^{\mathrm{discr}}$ will increase. On the other hand, if the transformation $x = \phi(t)$ implies a slower decay, then the transformed integrand at the truncation term $k = \pm n$, will not have small enough values, resulting in a higher $\mathrm{E}^{\mathrm{trunc}}$. Consequently, an optimal decay rate should exist that minimizes the total error of the quadrature rule (5.13).

In order to visualize this argument, the function $\cos(t)$ is chosen and is multiplied with a function that decays single exponentially, double exponentially or triple exponentially for large values of the argument t, i.e. $d_1(t) = \cos(t)\exp(-|t|)$, $d_2(t) = \cos(t)\exp(\exp(-|t|))$, $d_3(t) = \cos(t)\exp(\exp(\exp(-|t|)))$, respectively. The fictitious functions $d_i(t)$ represent the transformed integrand $f(\phi(t))\phi'(t)$ of (5.11). A discretization step of $h = 0.5$ is chosen and the summation is truncated at $t = nh = 2$, as shown in Fig 5.3.

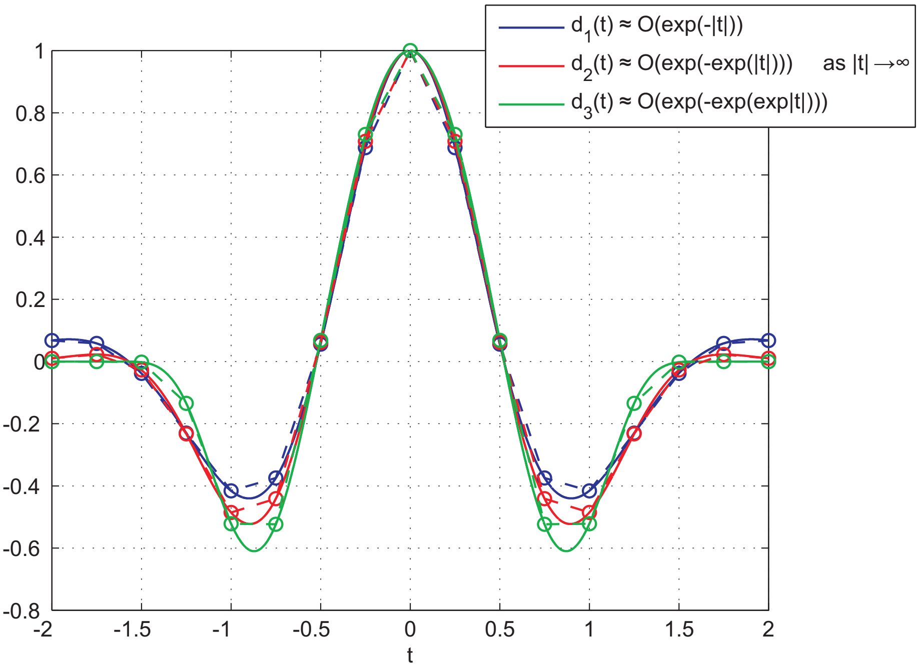

Figure 5.3: The function $\cos(t)$ is multiplied with a single exponentially (blue), double exponentially (red) or triple exponentially (green) decaying function. The solid lines represent the continuous functions, while the dashed line the sampled ones through the trapezoidal rule.

The truncation and discretization errors are shown in Figs. 5.4a and 5.4b, respectively. It is obvious, that while the truncation error decreases with the faster decay, the discretization

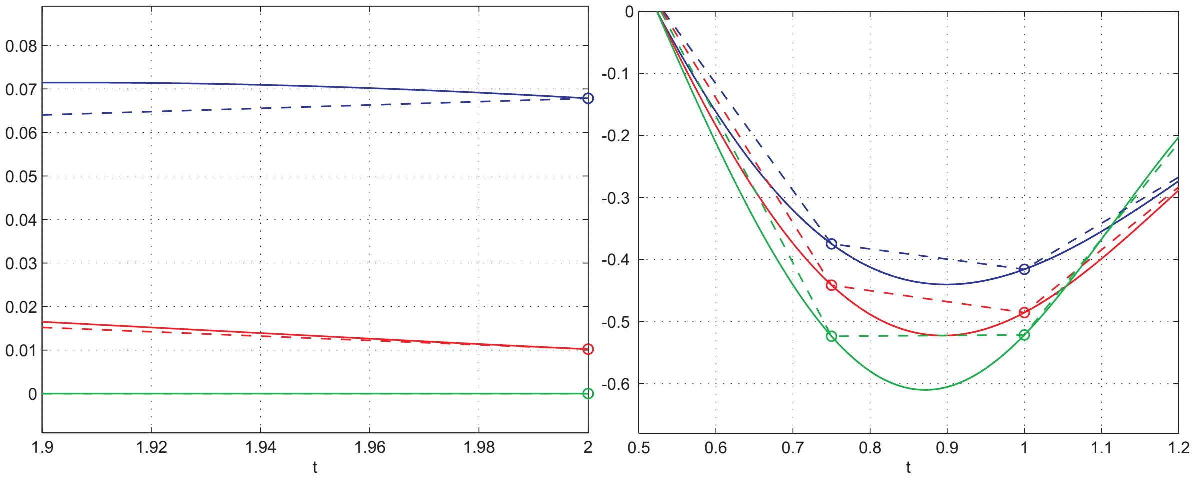

(a) **(b)**

Figure 5.4: Truncation error $\mathrm{E}^{\mathrm{trunc}}$ (a) and discretization error $\mathrm{E}^{\mathrm{discr}}$ (b) for the function $\cos(t)$ of Fig. 5.3 when a single (blue), double (red) or triple (green) exponential decay is applied. The solid lines represent the continuous functions, while the dashed line the sampled ones through the trapezoidal rule as in Fig. 5.3.

error increases. Consequently, there should be an optimal decay rate that minimizes the total error of the quadrature rule (5.13).

The appropriate decay rate for an optimal rule was found by Takahasi and Mori to be the double exponential one, which names also the numerical quadrature (DE) [122]:

$$x = \phi(t) = \tanh(\frac{\pi}{2}\sinh(t)) \tag{5.14}$$

and its derivative $\phi'(t)$ decays double exponentially for large arguments of t:

$$\phi'(t) = \frac{\frac{\pi}{2}\cosh(t)}{\cosh^2(\frac{\pi}{2}\sinh(t))} \simeq O(\exp(-\frac{\pi}{2}\exp(|t|))), t \to \infty \tag{5.15}$$

The DE transformation $\phi(t)$ (5.14) alongside with its derivative $\phi'(t)$ (5.15) are shown in Fig. 5.5. The coefficient $\pi/2$ in the original DE transform (5.14) was chosen in order to facilitate the numerical error analysis that Takahasi and Mori performed [122]. Modification of this choice are proposed in Chapter 7 in order to improve even further the performance of the DE rule, but within the current chapter we stick to the original transformation. Introducing (5.14) and (5.15) into (5.13), the final form of the DE quadrature rule can be derived:

$$I^f \simeq \sum_k w_k^{DE} f(x_k^{DE}) = \sum_{k=-n}^{n} \frac{\frac{\pi}{2}h\cosh(kh)}{\cosh^2(\frac{\pi}{2}\sinh(kh))} f(\tanh(\frac{\pi}{2}\sinh(kh))) \tag{5.16}$$

The DE rule, that sometimes is also known as $\tanh-\sinh$ rule due to the transformation involved (5.14), takes the form of an ordinary quadrature with predefined weights w_k and abscissas x_k which can be precomputed and stored in the memory.

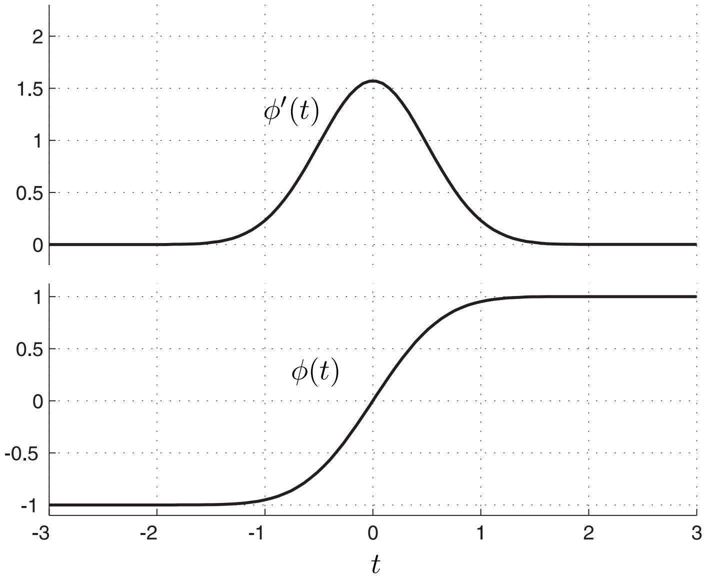

Figure 5.5: Double Exponential or tanh – sinh transformation and its corresponding derivative.

At this moment, there hasn't been yet discussion about the efficiency of the DE rule on integrating endpoint singularities. This additional and quite unique property can be justified through the Euler-Maclaurin formula [128], where the function $f(x)$ is assumed to be at least $(2m+2)$ times continuously differentiable over the interval $[a, b]$:

$$\int_a^b f(x)dx = h\sum_{j=0}^{n} f(x_j) - \frac{h}{2}(f(a) - f(b)) - \sum_{i=1}^{m} \frac{h^{2i}B_{2i}}{(2i)!}(f^{(2i-1)}(b) - f^{(2i-1)}(a)) - \mathrm{E}^{\mathrm{EMcL}} \quad (5.17)$$

where B_{2i} are the Bernoulli numbers and

$$\mathrm{E}^{\mathrm{EMcL}} = \frac{h^{2m+2}(b-a)B_{2m+1f^{(2m+2)}}(\xi)}{(2m+2)!} \quad (5.18)$$

for some $\xi \in (a, b)$. In general, the trapezoidal rule is considered as a very simple integration routine with a poor performance. Indeed, from (5.17) and for $m = 1$ it can be seen that each time that h is halved, the computational expense doubles but the discretization error reduces only by a factor of 4. However, if the integrand $f(x)$ has some very specific properties, which are fulfilled in the case of the DE transformation, then the error of the trapezoidal rule reduces much faster.

It has to be pointed out that (5.17) is valid even in the case that $a \to -\infty$ and $b \to \infty$. If the function $f(x)$ shows a smooth, bell-shaped behavior and the function itself and all its derivatives tend to zero at the endpoints a and b, properties that the DE transformation fulfils, then the second and the third terms of the right hand side of (5.17) vanish automatically. But since $\mathrm{E}^{\mathrm{EMcL}}$ is smaller than a constant times $\frac{h^{2m+2}}{(2m+2)!}$, for arbitrary m, we conclude that the error tends to zero more rapidly than any power of h [129].

A more illustrative approach for explaining the efficiency of the DE rule for handling arbitrary endpoint singularities can be obtained from Fig. 5.6, where the abscissas of the GL and the DE rules for the same number of integration points are shown. The DE rule can accumulate integration points arbitrarily close to the singular endpoints and extract accurate information from them. If the original function $f(x)$ has a singularity only in one end (for instance at $x = +1$), we are wasting points around $x = -1$. More specific DE transformation can be proposed following the discussions in Section 5.3.3.

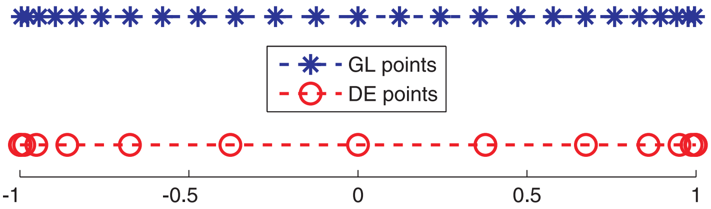

Figure 5.6: GL and DE abscissas for rules comprising 25 integration points over the reference domain $(-1, 1)$

5.3.1 Performance and implementation of DE quadrature rules

The first published paper on DE dates back to 1974 [122]. However, it didn't receive much attention until recently and one of the reasons for this is that a careless implementation of DE can jeopardize its fast convergence [127]. The $\cosh(\pi/2\sinh(t))$ term in the denominator of the weights of the DE formula (5.16) leads very fast to numerical overflows. An additional issue is if $f(x)$ has an endpoint singularity like $(1+x)^{-1+\mu}$ or $(1-x)^{-1+\mu}$, μ being a small positive constant, a large error due to loss of significant digits occurs at x very close to -1 or 1.

In order to overcome such problems, the summation of (5.16) is truncated at the point x_k for which the following inequality holds: $1-x_k < \text{eps}$, ensuring that $1-x$ and $-1+x$ are never equal to zero, eps being the machine's roundoff error. As initial discretization step $h = 1$ is chosen, which is halved in the next level of DE for reasons discussed in Section 5.3.2. For a double precision arithmetic unit, the number of integration points N used for each level M of the quadrature rule are shown in Table 5.1 [130].

The example of the equation (5.6) $f(x) = x\log x$ is used in order to demonstrate the performance of the DE rule against common interpolatory quadratures. As already said, it is the unbounded higher order derivatives at the endpoint $x = 0$ that deteriorate the performance of the GL rules. However, the DE rule manages to perform the integration in a fast and precise way, reaching numerically exact results for double precision arithmetics within a few integration points, as demonstrated in Fig. 5.7. Its behavior is very close to the ideal one of Fig. 5.2 and effort to improve it even more is made in Chapter 7. In fact the type of the singularity of $f(x) = x\log x$ is very similar to the one that appears in the MoM

M	0	1	2	3	4	5	6	7
h	1	1/2	1/4	1/8	1/16	1/32	1/64	1/128
N	7	13	25	51	101	203	405	809

Table 5.1: Number of integration points N for the level M of the DE rule where the discretization step is h. These values are valid for double precision arithmetic units.

reaction integrals of Chapter 7, improvising already the very competitive behavior of DE in these problems.

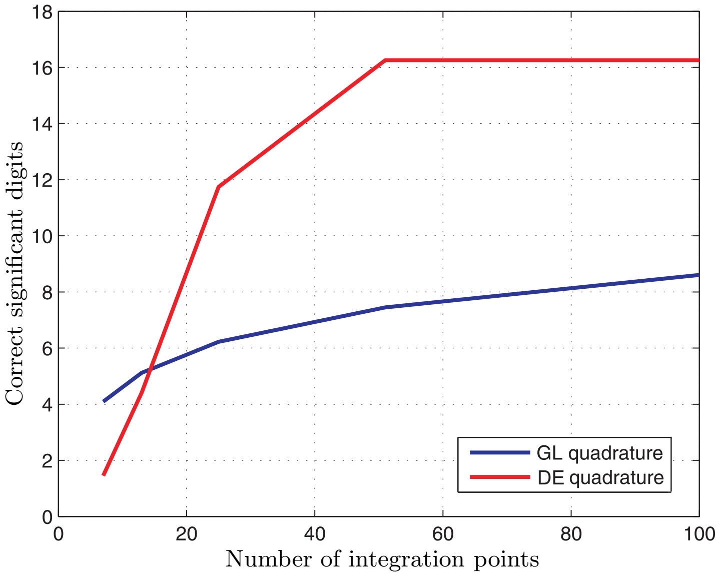

Figure 5.7: Performance of GL and DE quadrature rules integrating the function $f(x) = x \log x$ for $x \in (0, 1)$.

Another example that reveals the performance of the DE rule when integrands with endpoints singularities are involved is:

$$I = \int_{-1}^{1} \frac{1}{\sqrt{1-x^2}} dx = \pi. \tag{5.19}$$

Both endpoints $x = \pm 1$ are singular. The integral (5.19) is quite important as similar integrals appear often in Electromagnetics as it will be shown in Chapter 6. If the DE transformation of (5.14) is applied in (5.19), the integral becomes:

$$I = \int_{-\infty}^{\infty} \frac{\frac{\pi}{2}\cosh t}{\cosh^2(\frac{\pi}{2}\sinh t)} dt \tag{5.20}$$

The original integrand of (5.19) and the transformed one (5.20) are shown in Fig. 5.8: The singularities of the integrand (5.19) at the endpoints $x = \pm 1$ is moved through the DE transformation to $t = \pm\infty$ and they are decayed fast enough, so that the transformed integral (5.20) can be safely truncated. In the certain example of Fig. 5.8, the transformed integrand of (5.20) decreases to values of the order 10^{-13} for $t = 3$ and 10^{-38} for $t = 4$.

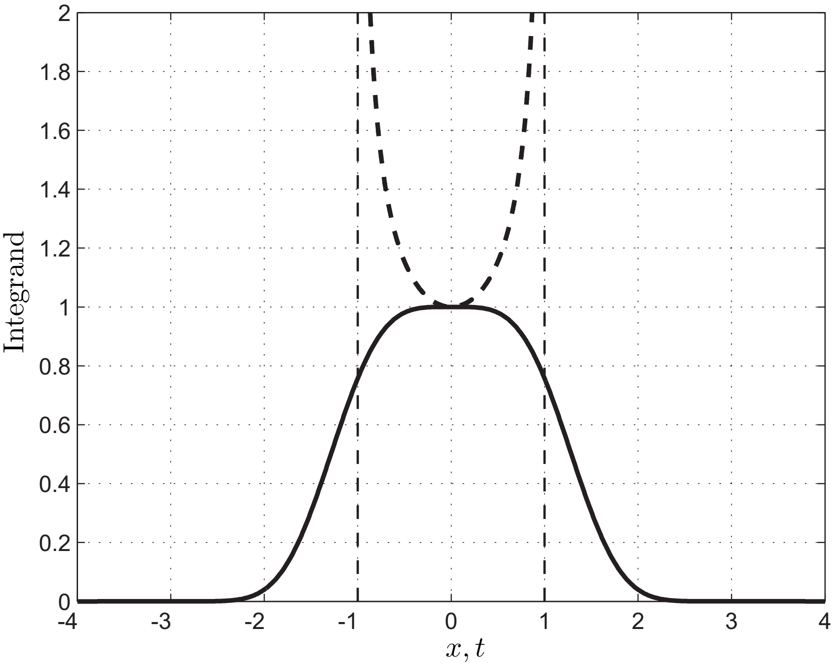

Figure 5.8: Original integrand (5.19) (dashed line) with singularities at the endpoints $x = \pm 1$ and transformed integrand (5.20) (continuous line) where the singularities have been moved to $t = \pm\infty$ and sufficiently decayed. The area under both curves is the same.

The performance of the DE rule against the GL one is shown in Fig. 5.9. The GL quadrature fails to converge to the exact value of the integral (5.19). On the other hand, the DE rule converges very fast to almost 16 correct significant digits, thus the numerically exact value for double precision arithmetics.

It has to be mentioned that if we use the GJ quadrature rule (5.7) with $\alpha = \beta = -0.5$, then the the singularities are taken into account through the weights of the Gaussian rule. According to (5.7) the remaining function $f(x) = 1$, that is a polynomial of zero order, which can be integrated exactly using only one sampling point according to the theory of Gaussian quadratures. However, if the behavior of the singularity varies even slightly than the one of the (5.19), then the performance of the DE rule remains the same as in Fig. 5.9 but the behavior

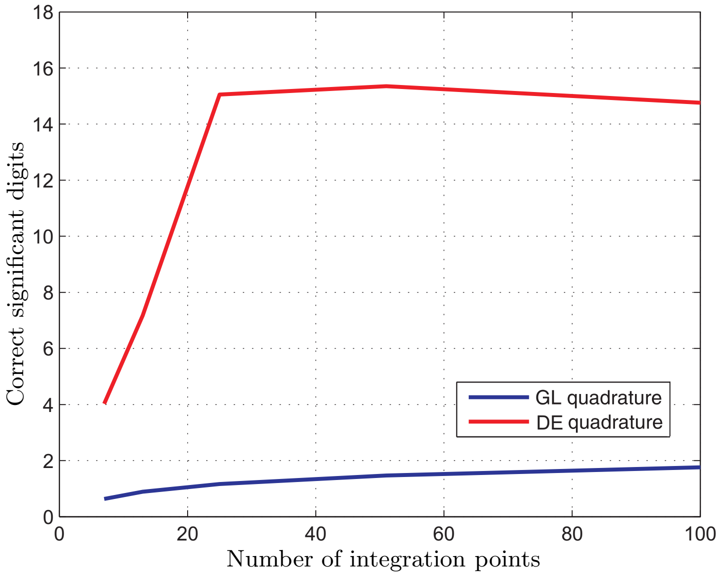

Figure 5.9: Performance of GL and DE quadrature rules integrating the function $f(x) = 1/\sqrt{1-x^2}$ for $x \in (-1, 1)$.

of GJ will tend to the GL one. And, unfortunately, in very limited cases the integrands that appear in the Chapters 6 and 7 have such a well defined singular behavior. Consequently, DE will be a very handful tool for their efficient numerical evaluation.

5.3.2 Adaptive DE quadrature rules

The number of integration points needed to guaranty a predefined accuracy is usually difficult to be estimated. Developing adaptive quadrature rules, that is reusing the computations that were done in a previous step, is a very appreciated as they save computational resources. The common strategy is that the numerical calculation of the integrals starts with a small number of integration points that is gradually increased until the error estimates or the convergence of the last successive steps indicate that the desired accuracy has been reached. Original Gaussian quadratures were lacking such a property and the calculations performed in the previous steps were useless for the next ones. This is the reason that in many professional computational routines, special forms of Gaussian quadratures are used that are adaptive: Gauss-Kronrod quadratures, Clenshaw-Curtis quadrature to mention a few [124].

The DE rule (5.16), if descretized properly, can be enhanced to perform as an adaptive quadrature. If in each step the sampling distance h is halved, then at level N, the DE quadrature rule is written as:

$$I(h) = \sum_{k=-n_1}^{n_1} \frac{\frac{\pi}{2} h \cosh(kh)}{\cosh^2(\frac{\pi}{2}\sinh(kh))} f(\tanh(\frac{\pi}{2}\sinh(kh))) \tag{5.21}$$

At the next level $N+1$, the sampling distance is $0.5h$:

$$I(0.5h) = \frac{1}{2}I(h) + \sum_{k_{odd}=-n_2}^{n_2} \frac{\frac{\pi}{2}\frac{h}{2}\cosh(k\frac{h}{2})}{\cosh^2(\frac{\pi}{2}\sinh(k\frac{h}{2}))} f(\tanh(\frac{\pi}{2}\sinh(k\frac{h}{2}))) \tag{5.22}$$

where the result of the previous step (5.21) has been reused in (5.22) and approximately only half of the quadrature points have to be calculated for the level $N+1$. This results in almost halving the computational time when increasing the order of the DE quadrature rule. This property is visualized in Fig. 5.10, where for each new level of the DE rule, only the red points have to be calculated [131].

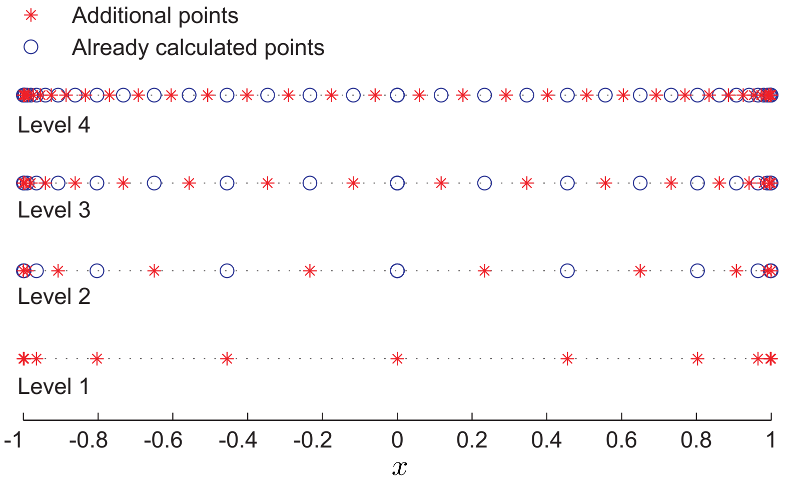

Figure 5.10: Additional (stars) and already evaluated (circles) points of a DE rule if the DE rule is implemented in an adaptive way.

5.3.3 DE quadratures for other types of integrals

The DE rule (5.13) has been developed for efficient integration of integrands that have singularities at both endpoints $x=1$ and $x=-1$, as the $\tanh-\sinh$ transformation decays double exponentially in both endpoints. If some more specific details about the integrand are known a priori, e.g. asymmetric decay in one endpoint, semi-infinite initial integration domain etc, specialized DE rules can be built by choosing the appropriate transformation $\phi(t)$ whose derivative $\phi'(t)$ decays double exponentially for $|t| \to \infty$. The different choices and relevant transformations are shown in Table 5.2 [132].

Of course, the transformations of Table 5.2 can be cascaded until the desired property of the double exponentially decay of the derivative $\phi'(t)$ is achieved. As an example, if the integrand has endpoint singularities at both edges of the finite integration domain, then the proper combination is first a tanh transformation to transform the finite integration domain

Interval	Transformation
Finite interval, e.g. $(-1, 1)$	$\phi(t) = \tanh(t)$
Semi-infinite interval, $(0, \infty)$	$\phi(t) = \exp(t)$
Real line, enhance the decay as $t \to \pm\infty$	$\phi(t) = \sinh(t)$
Real line, enhance decay as $t \to +\infty$	$\phi(t) = t + \exp(t)$
Real line, enhance decay as $t \to -\infty$	$\phi(t) = t - \exp(-t)$

Table 5.2: Possible transformation functions and their properties.

to the infinite one and then sinh transformation to accelerate the decay to double exponential tendency as $|t| \to \infty$. This results to the original $\tanh - \sinh$ transformation of (5.14).

If the integrand has only one endpoint singularity at $x = +1$, then according to Table 5.2, the transformations $\tanh(t)$ and $t + \exp(t)$ should be combined resulting in:

$$x = \phi(t) = \tanh(t + \exp(t)) \tag{5.23}$$

Equivalently, if the single endpoint singularity appears at $x = -1$, then the appropriate DE transformation is:

$$x = \phi(t) = \tanh(t - \exp(-t)) \tag{5.24}$$

Additional DE transformations that can be derived through the Table 5.2 and are found in literature [127] include the following integrals:

$$\begin{aligned} I &= \int_0^{\infty} f_1(x)dx \\ & x = \exp(\pi/2 \sinh(t)) \end{aligned} \tag{5.25}$$

$$\begin{aligned} I &= \int_0^{\infty} f_2(x)e^{-x}dx \\ & x = \exp(t - \exp(-t)) \end{aligned} \tag{5.26}$$

$$\begin{aligned} I &= \int_{-\infty}^{\infty} f_3(x)dx \\ & x = \sinh(\pi/2 \sinh(t)) \end{aligned} \tag{5.27}$$

$f_1(x)$ is a slowly decaying function as $x \to \infty$, $f_2(x)$ is also a slowly decaying function as $x \to \infty$, but the integrand is already decaying exponentially and $f_3(x)$ decays slowly at both ends $\pm\infty$. Of course, more combinations can be made in order to derive another variety of

DE quadratures, but we should always be careful that the transformation $\phi(t)$ that we choose doesn't introduce additional singular points close to the real axis. If this is the case, then the $\mathrm{E}^{\mathrm{discr}} = O(e^{-\frac{2\pi d}{h}})$, of the trapezoidal rule will not be anymore small enough and the performance of the DE quadrature will deteriorate. Among them, a DE rule for oscillatory functions over half infinite intervals has been developed [133] and a DE rule for integration over infinite intervals can be found [134].

5.4 Conclusion

The DE rule, a general and very efficient numerical quadrature for integrands with endpoint singularities, has been presented. Its potentiality for the numerical integration of Sommerfeld and MoM reaction integrals becomes clear. The in-depth analysis and understanding of the DE properties that were presented in this chapter, allow us to implement the DE properly and in an adaptive way and to propose new DE rules suitable for each type of integrand with one or two singular endpoints, as the ones shown in (5.23) and (5.24).

6 Numerical Evaluation of Sommerfeld Integrals

A thorough investigation on the spectral domain Green's functions for multilayered structures has been presented in Chapter 4. Moreover, a generalized procedure to derive these Green's function has also been developed and the vector and scalar potential GFs in the spectral domain for multilayered structures with arbitrary number of dielectric layers and conductive sheets are at hand. In order to utilize these results in a MoM code, the spatial domain counterparts need to be calculated through an inverse Fourier transform. It has been demonstrated that the spectral domain GFs can be found analytically, even in case of numerous layers and tensorial conductivity. However, except from very simplified geometries like the radiation of a dipole in a mono-layered structure, i.e. radiation in the free space [65], the transformation from the spectral to the spatial domain cannot be performed analytically. In all the other cases, numerical algorithms have to be developed in order to derive the spatial GFs efficiently and accurately. The calculated spatial GFs will be further used in a numerical scheme in order to calculate the reaction integrals between the discretized patches of the EM problem, as showing in Chapter 7, and then the resulting MoM matrix has to be inverted, most of the times using one of the iterative methods provided by matrix analysis. Due to the bad condition number of these matrices [135], it is obvious that a minor and uncontrollable numerical error in the evaluation of the spatial GF can result in a much stronger variation in the final solution, even in completely erroneous results if at some point a really ill-conditioned integral operator is involved. Under this framework, all the algorithms developed within this chapter and the next ones will focus on controlling the numerical accuracy of the results, that, depending on the computational resources available, can vary from numerically exact results to less accurate but very competitive ones in terms of execution time.

In Section 6.1 the behavior of the integrand of a Sommerfeld integral will be addressed in order to identify the numerical difficulties to be tackled. This is done in the context of the new potential difficutlies introduced by the presence of conductive sheets. Then, the semi-infinite integration domain of the Sommerfeld integral is split between the first part, sometimes also called head of the Sommerfeld Integral, in Section 6.2 and the tail in Section 6.3. For the first part, a novel approach, based on the Double Exponential (DE) quadrature rule presented in Chapter 5, is utilized for calculating numerically the Sommerfeld integrals. Instead of performing a detour in the complex plane to avoid the branch point and surface waves singularities, an on-the-axis integration is performed. Concerning the tail, the well-known weighted average (WA) approach [78] is used in order to integrate the remaining semi-infinite oscillating part of the Sommerfeld integral. In Section 6.4, a very efficient error estimator has been developed for the DE integration, so that the final result is exact up to the predefined accuracy. Finally, Section 6.5 presents numerical results of both simple - in order to prove the concepts - and more complicate structures verifying the validity of the method and its efficiency compared to other state-of-the-art methods.

6.1 Typical behavior of a Sommerfeld Integral

Considering a generic multilayered structure, Sommerfeld integrals can be formulated, as already summarized in Table 4.1, as:

$$S_n\{\tilde{G}(k_\rho; z|z')\} = \frac{1}{2\pi}\int_0^\infty \tilde{G}(k_\rho; z|z')\mathrm{J}_n(k_\rho\rho)k_\rho^{n+1}dk_\rho, \tag{6.1}$$

where $\tilde{G}$ is the spectral domain Green function, J_n is the Bessel function of the first kind of order n, ρ is the horizontal distance between source and field point, while z and z' are the vertical coordinates of the source and field points, respectively. Due to the uniaxial symmetry of the multilayered structure, $\tilde{G}$ is readily available in closed form, as shown in Chapter 4. Its exact representation is the key point for a very accurate numerical solution, provided that the integration in (6.1) is performed carefully.

The numerical evaluation of Sommerfeld integrals becomes non-trivial due to:

- the semi-infinite domain of integration combined with the fast oscillations due to the presence of the Bessel function
- the presence of the branch point, where the higher order derivatives of the integrand are not bounded
- possible surface waves poles, including surface plasmon polaritons, found on the integration path or in its proximity.

These points are clearly illustrated in Fig. 6.1, where a typical integrand of the Sommerfeld integral for a multilayered structure is plotted.

The importance of the Sommerfeld integrals and their computational difficulties have raised the interest of the scientific community and various strategies have been proposed. In general, they can be split in two wide categories: the closed form methods and the methods based on direct numerical integration.

One of the most representative examples of the closed form methods is the Complex Image Method (CIM), where the spectral domain green function is expanded into a series of exponentials. Using appropriate Sommerfeld identities, each term of the series can be integrated analytically avoiding the need of infinite and oscillating integrals. Though the analytical integration that is performed is exact, the numerical error is introduced through the approximation of the spectral domain GF with the exponential series and its unavoidable truncation. One of the biggest drawbacks of this method is that only recently some work towards a reliable error estimation technique has been performed [72]. At the point that this technique becomes mature and stable enough, it will be able to guarantee a bounded level of accuracy for the spacial domain GF.

On the other hand, the direct integration numerical techniques use the exact representation of the spectral domain GF. Integration with classical techniques fails due to the improper nature of the Sommerfeld integral, as described before. Thus, deformation of the integration path, substraction of ill behaved parts of the integrand and appropriate variable transformations are among the techniques that need to be combined together in order to perform the numerical integration. In this case, the integration domain is split in two parts, $\mathcal{S}_n = \mathcal{I}_n + \mathcal{T}_n$, due to the nature of the kernel of the Sommerfled integral. The first part, $\mathcal{I}_n$, includes the branch point and the pole singularities and the second part, $\mathcal{T}_n$ - alternatively called tail of the Sommerfeld integral - comprises the high oscillatory of the remaining singularity-free semi-infinite domain.

$$\mathcal{I}_n \left\{ \tilde{G}(k_\rho; z|z') \right\} = \frac{1}{2\pi} \int\limits_0^{\xi_0} \tilde{G}(k_\rho; z|z') \mathrm{J}_n(k_\rho \rho) k_\rho^{n+1} dk_\rho, \tag{6.2}$$

where the upper limit ξ_0 is chosen such as no singularities are present in the integrand for values $\mathrm{Re}\{k_\rho\} > \xi_0$, and the remaining SI infinite tail:

$$\mathcal{T}_n \left\{ \tilde{G}(k_\rho; z|z') \right\} = \frac{1}{2\pi} \int\limits_{\xi_0}^{\infty} \tilde{G}(k_\rho; z|z') \mathrm{J}_n(k_\rho \rho) k_\rho^{n+1} dk_\rho. \tag{6.3}$$

As the properties of the two parts differ, numerical strategies specially tailored to each part have been developed and discussed in Section 6.2 and 6.3, respectively.

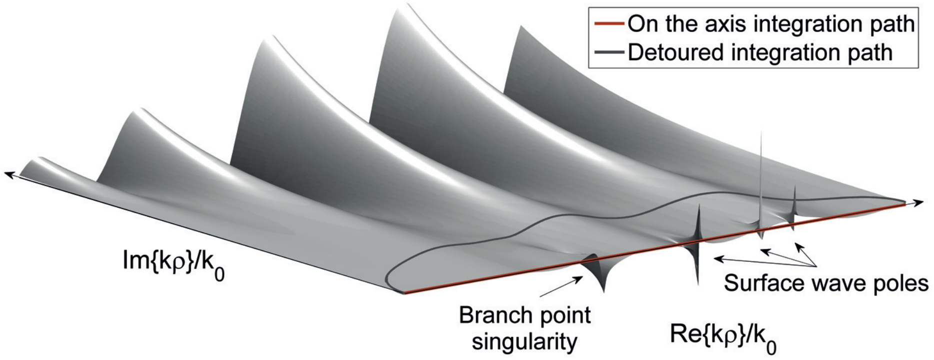

Figure 6.1: Integrand of a typical Sommerfeld integral, with the branch point and three surface waves poles visible. The common detoured path and the proposed on the axis integration path are indicated.

6.2 First part of the Sommerfeld Integral

The integrand of the first part of the SI (6.2) incorporates the product of a fast oscillating Bessel function with a spectral domain GF, $\tilde{G}$. This GF can be analytically derived for multilayered structures that are transversely invariant. According to the configuration of the layers and the working frequency, $\tilde{G}$ shows poles on the real axis for lossless cases or on the fourth quadrant when lossy materials are involved and a $e^{j\omega t}$ time dependence is considered. Moreover, when a ground plane is introduced only at one end of the multilayered structure, a branch point singularity $k_z = \sqrt{k^2 - k_\rho^2}$ is present, k being the wavenumber of the semi-infinite layer for the working frequency, whereas when it radiates on both sides two branch points are involved.

In order to avoid the branch point(s) and the poles of $\tilde{G}$, the integration path is usually deformed into the first quadrant of the complex k_ρ-plane, as shown in Fig. 6.2.

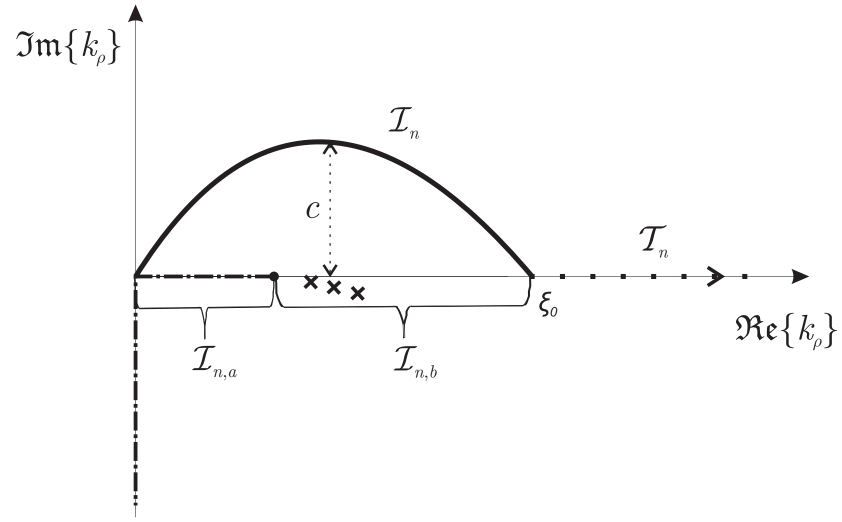

Figure 6.2: Integration path of SIs. Separation between the first part, I_n, and the tail T_n.

The deformed path can be chosen arbitrarily, under the condition that the path remains on the same Riemann sheet. On the one hand, in Fig. 6.1, we can observe that if the integration path is deformed far away from the real axis, then the large values of the bessel function will make the numerical integration more difficult, while on the other hand, remaining close to the real axis, the effect of the poles and the branch point will affect the efficiency of the integration.

Consequently, an optimized path, based on the parameterized contour of an ellipse that is proposed in [75], is quite often chosen as it provides competitive behavior for a wide range of distances ρ and layer configurations. It will be considered as the reference method to compare against for the rest of this work. This path is shown in Fig. 6.1 with a gray line.

As an alternative, integration on the real axis instead of the deformed path would be faster if the poles could be accurately located and the branch point appropriately treated. Such an integration path is indicated in Fig. 6.1 with the red line. The strategies to overcome efficiently the surface wave poles and the branch points are discussed in 6.2.1 and 6.2.2, respectively.

6.2.1 Surface wave poles including plasmons

In order to overcome the numerical obstacles of the surface wave poles, a robust and efficient pole extracting algorithm [77] can be utilized. It locates the poles accurately even if they lie very close to the branch point. Hence, they can be removed from the singular spectral domain GF $\tilde{G}$ and their contribution to the spatial domain GF, G can be taken into account analytically. The surface wave poles are located on the real axis in the case of lossless structures and they migrate to the fourth quadrant of the k_ρ plane if lossy materials are present. Even if the poles are not included in the integration path, still it is strongly recommended to extract them, as the remaining integrals become smoother and easier to be handled numerically. Moreover, the search of the position of the poles is performed only once per frequency sample and is a very small overhead in the total amount of computations required to calculate all the required spatial domain GFs for various horizontal ρ and vertical z distances, respectively.

As the poles $k_{\rho i}$, including surface wave and plasmon ones - i pointing to each one of the N_p poles of the multilayered structure at the operating frequency - appear in pairs in the complex plane, each pair $\pm k_{\rho i}$ should be subtracted. Moreover, another pair of spurious, non existent poles, $\mp jk_{\rho i}$ is subtracted, as it has been shown that such an action improves the convergence of the remaining integrals [136], [137]. Finally, the subtracted part from the spectral domain GF, $\tilde{G}^p$ can be written as:

$$\tilde{G}^p(k_\rho) = \sum_{i=1}^{N_p}\left(\frac{2R_i k_{pi}}{k_\rho^2 - k_{\rho i}^2} - \frac{2R_i k_{pi}}{k_\rho^2 + k_{\rho i}^2}\right) = \sum_{i=1}^{N_p}\frac{4R_i k_{pi}^3}{k_\rho^4 - k_{\rho i}^4} \tag{6.4}$$

The residuals R_i are calculated by integrating in the complex plane the GF $\tilde{G}$ over a closed contour that includes only the corresponding pole $k_{\rho i}$. The integration path is usually chosen to be a circle due to the easiness in its parametrization, therefore the residuals of each pole can be calculated through (6.5) using standard integration routines.

$$R_i = \frac{1}{2\pi}\int_0^{2\pi}\tilde{G}(k_\rho)\alpha e^{j\phi}d\phi \tag{6.5}$$

where $k_\rho = k_{\rho i} + \alpha e^{j\phi}$ and the radius α is chosen so that no other pole is included in the closed integration domain.

Having identified the position of the poles and the values of the residuals, the transformation of (6.4) to the spatial domain can be performed analytically using the identities (6.6) and (6.7), for the generalized Sommerfeld integrals S_0 and S_1, respectively.

$$S_0\{\tilde{G}^p\} = \int_0^\infty \tilde{G}^p(k_\rho)\mathrm{J}_0(k_\rho\rho)k_\rho dk_\rho = -\sum_{i=1}^{N_p} k_{\rho i}R_i(j\pi\mathrm{H}_0^{(2)}(k_{\rho i}\rho) + 2\mathrm{K}_0(k_{\rho i}\rho)) \tag{6.6}$$

$$S_1\{\tilde{G}^p\} = \int_0^\infty \tilde{G}^p(k_\rho)\mathrm{J}_1(k_\rho\rho)k_\rho^2 dk_\rho = -\sum_{i=1}^{N_p} k_{\rho i}^2 R_i(j\pi\mathrm{H}_1^{(2)}(k_{\rho i}\rho) + 2\mathrm{K}_1(k_{\rho i}\rho)) \tag{6.7}$$

where K_n is the modified Bessel function of order n [106]. It should be pointed out that the first two generalized Sommerfeld integrals S_0 and S_1 are enough in order to perform all the transformations from the spectral to spatial domain that are indicated in Table 4.1.

6.2.2 Branch point singularity

The remainder of the GF $\tilde{G}^{np} = \tilde{G} - \tilde{G}^{p}$ does not include any poles, meaning that the pole extraction has already been performed and the remaining branch point irregularity has to be treated. The choice of the seperation point between the first part and the tail of the Sommerfeld integral ξ_0 is not so crucial due to the absence of the poles. However, it should be relatively far away from $k_\rho = k$ so that the effect of the branch point will already be weakened when the integration of the tail begins. On the other hand, especially for large arguments of the horizontal separation ρ, the oscillations of the Bessel function are present even around $k_\rho = k$, in which case it is more efficient to choose ξ_0 closer to the branch point in order to take advantage of the special algorithms for the oscillating integrands.

Focusing on the numerical techniques, the irregular behavior of (6.2) at the branch point $k_\rho = k$ calls for a further split of the integration domain resulting in two integrals, both of them being singular only at their common end-point $k_\rho = k$:

$$\mathcal{I}_n = \mathcal{I}_{n,a} + \mathcal{I}_{n,b} \tag{6.8}$$

where

$$\mathcal{I}_{n,a} = \frac{1}{2\pi} \int\limits_0^k \tilde{G}^{np}(k_\rho) \mathrm{J}_n(k_\rho \rho) k_\rho^{n+1} dk_\rho \tag{6.9}$$

$$\mathcal{I}_{n,b} = \frac{1}{2\pi} \int\limits_k^{\xi_0} \tilde{G}^{np}(k_\rho) \mathrm{J}_n(k_\rho \rho) k_\rho^{n+1} dk_\rho \tag{6.10}$$

It should be pointed out that $\tilde{G}^{np}$ explicitly includes the term $k_z = \sqrt{k^2 - k_\rho^2}$ and can be rewritten as

$$\tilde{G}^{np}(k_\rho) = \tilde{G}^{np}(k_\rho, k_z(k_\rho)) \tag{6.11}$$

The first order derivative of (6.11) is

$$\frac{\partial \tilde{G}^{np}(k_\rho, k_z)}{\partial k_\rho} = \frac{\partial \tilde{G}^{np}(k_\rho, k_z)}{\partial k_z} \frac{\partial k_z}{\partial k_\rho} + \frac{\partial \tilde{G}^{np}(k_\rho, k_z)}{\partial k_\rho} \tag{6.12}$$

which obviously is unbounded for $k_\rho = k$, same for all the higher order ones. This is the reason that special quadrature routines that are able to handle endpoint singularities should be used for the numerical integration of (6.9) and (6.10). The Double Exponential (DE) rule, that has already been discussed in Chapter 5, has been found to be one of the most efficient routines for this purpose.

As most of the quadrature rules, including the DE one, are defined over the $[-1, 1]$ integration domain, a suitable change of variables in $\mathcal{I}_{n,a}$ and $\mathcal{I}_{n,b}$ allows us to rewrite (6.9) and

(6.10) as (6.13) and (6.14), respectively:

$$\mathcal{I}_{n,a} = \frac{1}{2\pi} \int_{-1}^{1} \tilde{G}^{np}(k_{\rho,a}(x), k_{z,a}(x)) \mathrm{J}_n(k_{\rho,a}(x)\rho) \frac{k}{2} k_{\rho,a}^{n+1}(x) dx \tag{6.13}$$

$$\mathcal{I}_{n,b} = \frac{1}{2\pi} \int_{-1}^{1} \tilde{G}^{np}(k_{\rho,b}(x), k_{z,b}(x)) \mathrm{J}_n(k_{\rho,b}(x)\rho) \frac{\xi_0 - k}{2} k_{\rho,b}^{n+1}(x) dx \tag{6.14}$$

where

$$\begin{aligned} k_{\rho,a}(x) &\rightarrow \frac{k}{2}(1+x) && (6.15) \\ k_{z,a}(x) &\rightarrow \frac{k}{2}\sqrt{x+3}\sqrt{-x+1} = \frac{k}{2}\sqrt{x+3}\sqrt{\mathrm{H}} && (6.16) \\ k_{\rho,b}(x) &\rightarrow \frac{\xi_0 - k}{2}(x + \frac{\xi_0 + k}{\xi_0 - k}) && (6.17) \\ k_{z,b}(x) &\rightarrow j\frac{\xi_0 - k}{2}\sqrt{x + \frac{\xi_0 + 3k}{\xi_0 - k}}\sqrt{1+x} = j\frac{\xi_0 - k}{2}\sqrt{x + \frac{\xi_0 + 3k}{\xi_0 - k}}\sqrt{\Xi} && (6.18) \end{aligned}$$

The monomials $\Xi = 1 + x$ and $\mathrm{H} = 1 - x$ have to be identified in (6.16) and (6.18), as they require special numerical treatment as shown in 6.2.3.

All the above developments easily generalize to the cases where two separated branch points are present, like in the case of a graphene sheet separating two different semi-infinite media.

6.2.3 Particularities in the Double Exponential quadrature rule

Throughout this work, a modified version of the DE transformation, almost equivalent to the one discussed in [138], will be utilized. It provides faster convergence to the desired accuracy, compared to the original one, and incorporates the following transformation function $\phi(t)$:

$$x = \phi(t) = \tanh(\sinh(t)) . \tag{6.19}$$

A crucial issue concerning the accuracy is encountered, if $f(x)$ has singularities at the end-points of the form $(1+x)^{-1+\mu}$ or $(1-x)^{-1+\mu}$, where μ is a small positive constant [127]. For values of x very close to -1 and 1, the binomials $\Xi = 1 + x$ and $\mathrm{H} = 1 - x$, respectively, should be identified and precomputed through:

$$\begin{aligned} \Xi &= 1 + x = \frac{\exp(\sinh(t))}{\cosh(\sinh(t))} && (6.20) \\ \mathrm{H} &= 1 - x = \frac{\exp(-\sinh(t))}{\cosh(\sinh(t))} && (6.21) \end{aligned}$$

instead of using directly:

$$\begin{aligned} \Xi &= 1 + x = 1 + \tanh(\sinh(t)) && (6.22) \\ \mathrm{H} &= 1 - x = 1 - \tanh(\sinh(t)). && (6.23) \end{aligned}$$

The reason for this is the ability of the DE rule to concentrate points arbitrarily close to the endpoints -1 and 1, resulting in numerical underflows in terms such as $1 + x$ and $1 - x$. In order to get results up to numerical precision of the computing machine, the DE implementation shown in Chapter 5 has to be slightly enhanced so as the outputs of the rule do not only include the weights and abscissas but also the values of the monomials Ξ and H computed through (6.20) and (6.21), respectively. These additional computations are performed only once and stored next to the weights and abscissas and no additional complexity of the numerical algorithms is further required.

6.3 Tail of the Sommerfeld Integral

Altough the Sommerfeld integral tail (6.3) is free of branch point singularities, its numerical evaluation still remains a very challenging computational task. The integration path extends to infinity and if the observation and source point are at the same vertical distance $z = z'$, then the integrand of (6.3) may even diverge. In this case, the integral (6.3) cannot even be defined in the classical Riemann sense.

Among the numerical techniques proposed, one of the most popular and efficient is the Weighted Averages (WA) method which was formalized in [139] and revisited in [78]. Another recently developed method [79] incorporates a variant of the DE rule [140] presented in Section 5, that competes with the WA one [80].

In the current work the tail of the Sommerfeld integrals is calculated using the new WA method developed in [78] and its implementation will be briefly demonstrated. Let us assume a spectral domain GF $\tilde{G}$ with the following asymptotic behavior as $k_\rho \to \infty$:

$$\tilde{G} \sim \frac{e^{-k_\rho |z-z'|}}{k_\rho^{\mu}} (C + O(k_\rho^{-1})) \tag{6.24}$$

where μ can easily be deduced from simple inspection of $\tilde{G}$ [56], [141]. Then, the partial integrals I_i, $0 \leq i \leq N$, can be defined as:

$$I_i = \int_{\xi_0}^{\xi_{i+1}} \tilde{G} \mathrm{J}_n(k_\rho \rho) k_\rho^{n+1} dk_\rho \tag{6.25}$$

The numerical integration of (6.25) becomes more efficient if ξ_0 is chosen to be a root of the corresponding bessel function J_n. Taking into account (6.24), the integrand of (6.25) behaves as a power k_ρ^q as $k_\rho \to \infty$ [78], where q is:

$$q = n - \mu + 0.5 \tag{6.26}$$

In order to derive simpler formulas for the weights, the following equidistant breakpoints ξ_i are considered if $\rho \neq 0$:

$$\xi_i = \frac{\xi_0}{\rho} + i\frac{\pi}{\rho} \tag{6.27}$$

or in case that $\rho = 0$:

$$\xi_i = \frac{\xi_0}{|z-z'|} + i\frac{\pi}{|z-z'|}. \tag{6.28}$$

Following the choice for the breakpoints ξ_i of (6.27) or (6.28), the weights of the WA method, assuming N partial integrals (6.25), are obtained through:

$$w_i^{(N)} = \binom{N-1}{i-1} e^{\xi_i|z-z'|}\xi_i^{N-2-q} \tag{6.29}$$

Finally, the tail of the Sommerfeld integral (6.3) is calculated through the weighted averages:

$$T_n(N) = \frac{1}{2\pi}\frac{\sum\limits_{i=1}^{N} w_i^{(N)} I_i}{\sum\limits_{i=1}^{N} w_i^{(N)}} \tag{6.30}$$

If higher accuracy is needed, the number of the partial integrals N is increased. Then, as the weights $w_i^{(N)}$ depend on the number of the finite integrals, they need to be recomputed in order to calculate the value of $T_n(N+1)$. A careful investigation of (6.29) and (6.30) shows that results of the previous step $N-1$ can be reused, reducing the computational cost of the additional and more precise iteration [80].

6.4 Error Estimation

Estimation of the numerical error in the approximation of an integral using a numerical quadrature is always advantageous. It can guarantee a predefined level of accuracy by automatically selecting the number of integration points needed for achieving this accuracy. Thus, destructive results due to propagation of unbounded errors can be avoided, while integration points and computational resources are not wasted. Two key points determine the success of such error estimators: their accuracy and the additional computational complexity required for their calculation.

Most of the numerical techniques rely on an ad hoc error estimation, which takes into account the difference between the last two steps of the iterative algorithm. If the difference is smaller than a predefined tolerance, then the iterative loop breaks and the algorithm returns the value of the last iteration as the most accurate one. However, by using this technique, there is no clue what is the order of the actual error; it just provides an indication that the iterative process seems to have converged. Moreover, it is quite common that the tendency of the convergence rate is not monotonous and if some additional iterations are performed, then the difference between the results of two successive iterations increase again.

Additionally, another drawback of such a technique is that a further iteration is needed in order to have an indication if the current iteration provides an accurate enough result. If high precision calculations are required, then the additional iteration could be computationally too expensive or even inaccurate due to the small round off errors that affect the less significant digits of the calculations.

A better practice for developing an efficient error indicator is through mathematical considerations and properties that estimate the error of the current iteration without relying on previous or forward iterations. Obviously, such indicators are difficult to be developed and they are case specific. If it is the case that one fits the current numerical problems, then definitely it should be tried out. Such an error estimator is analyzed in 6.4.1 for the first part of the Sommerfeld integral, while for the tail we rely on more standard ways of controlling the error of the numerical calculations 6.4.2.

6.4.1 Error Estimation for the first part of the Sommerfeld Integral

Recently, a new error estimator has been developed for Euler-Maclaurin based quadrature schemes [142]. The error of the DE rule (5.14), as it is based on a trapezoidal discretization scheme, can indeed be written in terms of the Euler-MacLaurin formula (5.17). Then, the potential of adapting the results of [142] for the DE case and the first part of the Sommerfeld integral becomes evident.

To begin with, the researchers in [142] managed to write the error term $\mathrm{E}^{\mathrm{EMcL}}$ of the Euler-MacLaurin formula (5.18) as:

$$\begin{aligned}\mathrm{E}_1^{\mathrm{EMcL}}(h,m) =& h(-1)^{m-1}(\frac{h}{2\pi})^{2m}\sum_{j=a/h}^{b/h}\mathcal{D}^{2m}f(jh)\\ &+2(-1)^{n-1}(\frac{h}{2\pi})^{2m+2n}\sum_{k=1}^{\infty}(\frac{1}{k^{2n}}+\frac{(-1)^m}{k^{2m+2n}})\int_a^b\cos(2k\pi(t-a)/h)\mathcal{D}^{2m+2n}f(t)dt\end{aligned} \tag{6.31}$$

under the conditions that $f(a)=f(b)=0$, f is at least $2m$ times continuously differentiable on $[a,b]$, $D^kf(a)=D^kf(b)$ for $1\leq k\leq 2m$ and n being an integer such that $n\geq 1$. Surprisingly, all these properties are valid for the DE rule. The only singularities of the integrand are allowed to be at the endpoints, which through the $\tanh-\sinh$ transformation are pushed to infinity. But at infinity, the DE rule decays double exponentially, eliminating the singular behavior of the function and its derivatives at the endpoints.

In [142], it was also demonstrated that the first term of (6.31) is much more significant than the second one, consequently $\mathrm{E}^{\mathrm{EMcL}}$ can be approximated by:

$$\mathrm{E}_2^{\mathrm{EMcL}}(h,m) = h(-1)^{m-1}(\frac{h}{2\pi})^{2m}\sum_{j=a/h}^{b/h}\mathcal{D}^{2m}f(jh). \tag{6.32}$$

Finally, it was observed that (6.32) predicts correctly the order of magnitude of the error even for $m = 1$ for various quadrature rules based on a trapezoidal discretization method. Such an observation greatly simplifies the error estimation formula, and after extensive investigation of the DE rule using different test case, the error estimator of the DE rule can be written as:

$$E^{\mathrm{DE}}(h) = \frac{h^3}{(2\pi)^2} \sum_{k=-n}^{n} \mathcal{D}^2 g(kh) \tag{6.33}$$

where $\mathcal{D}$ denotes the differentiation operator and $g(t) = f(\phi(t))\phi'(t)$ is the transformed integrand as given in (5.11), $\phi(t)$ being the $\tanh - \sinh$ transformation of (6.19).

More explicitly, the differential operator $\mathcal{D}$ can be written as:

$$\begin{aligned} \mathcal{D}^2 g(t) &= \mathcal{D}^2 \left[f(\phi(t))\phi'(t) \right] \\ &= f(\phi(t))\phi_1(t) + f'(\phi(t))\phi_2(t) + f''(\phi(t))\phi_3(t) \end{aligned} \tag{6.34}$$

where

$$\begin{aligned} \phi_1(t) &= \phi'''(t) \\ \phi_2(t) &= 3\phi(t)\phi''(t) \\ \phi_3(t) &= \left[\phi'(t)\right]^3 . \end{aligned} \tag{6.35}$$

The evaluations of (6.35) need to be performed only once, as they solely include the transformation function of the DE rule $\phi(t)$ and its derivatives, which are known a-priori (6.19) and can be stored next to the abscissas and the weights of the DE quadrature rule. The additional computational cost of this error estimator resides only in the calculation of $f'(\phi(t))$ and $f''(\phi(t))$ at the integration points of the DE rule. If the DE rule is implemented in an adaptive way according to Section 5.3.2, then also the error estimator (6.34) inherits this property as not to require evaluation of functions at points different than the ones of the DE rule.

At this point, the formula for an error estimator for the DE rule is at hand (6.34), the success of which will depend on how fast and how accurate this error estimator is. For this purpose, numerical examples will be provided in Section 6.5.

6.4.2 Error Estimation for the tail of the Sommerfeld Integral

The WA technique calls for N finite integrations I_i of smooth functions, which are afterwards properly weighted. Standard GL quadratures are used for these integrations, as the smoothness of the integrands guarantees their efficient evaluation. Studies have shown that a GL quadrature rule with 16 integration points is enough to reach numerically exact results with double precision arithmetics. Since the integrals I_i are precisely calculated, the accuracy of the evaluation of the Sommerfeld tail is improved by performing additional finite integrations I_i for $i > N$. The value of the tail of the Sommerfeld integral for N partial integrals properly weighted [78] is given in (6.30). The simplistic error of two successive steps, $N - 1$ and N, usually is enough:

$$E_1^{WA}(N) = |T_n(N) - T_n(N-1)| \tag{6.36}$$

Targeting high precision results, in some rare cases, the error estimation of two successive steps E_1^{WA} was not enough to guarantee numerical exact values, so an error estimation of three successive steps E_2^{WA} was adopted and used throughout all the calculations shown in the next Section:

$$\begin{aligned} E_2^{WA}(N) &= \max\{E_1^{WA}(N), E_1^{WA}(N-1)\} \\ &= \max\{|T_n(N) - T_n(N-1)|, |T_n(N-1) - T_n(N-2)|\} \end{aligned} \tag{6.37}$$

6.5 Numerical Results

The evaluation of the efficiency of the numerical methods presented in the previous chapters will be performed through certain examples of EM problems. These examples include:

- A radiating dipole in free space electric dipole. An analytical solution based in the Sommerfeld identity exists and is very useful to prove that the concepts presented perform as expected.
- A real-life dielectric slab with losses and surface wave poles which is considered to be computationally challenging [71].
- A recent technological application that includes the excitation of a surface plasmon mode on a graphene sheet [101].

6.5.1 Electric dipole in free space

Validation of the concepts described in the previous sections is presented through some characteristic examples, based on the radiation of an electric dipole in free space. The spectral domain GF for the scalar potential $\tilde{G}_V^x$ of an $\hat{x}$ directed electric dipole is:

$$\tilde{G}_V^x = \frac{1}{2\pi} \frac{\mathrm{e}^{-jk_z|z-z'|}}{jk_z} \tag{6.38}$$

where $k_z = \sqrt{k^2 - k_\rho^2}$ and z, z' are the vertical positions of the observation point and the dipole, respectively.

The spatial domain GF of (6.38) can be written as a Sommerfeld integral based on the transformations of the Table 4.1:

$$G_V^x = S_0[\tilde{G}_V^x] = \frac{1}{2\pi} \int_0^\infty \frac{\mathrm{e}^{-jk_z|z-z'|}}{jk_z} \mathrm{J}_0(k_\rho \rho) k_\rho dk_\rho = \frac{1}{2\pi} \frac{\mathrm{e}^{-jkr}}{r} \tag{6.39}$$

where $r = \sqrt{\rho^2 + z^2}$. Actually, (6.39) is indeed the Sommerfeld identity and due to its closed form solution in the spatial domain, it will form the basis of the examples presented hereafter.

The most challenging situation in evaluating the Sommerfeld integral of (6.38) is met when the vertical distances of the field and the source point coincide, i.e. $z = z'$. Under such conditions, the decay due to the exponential term vanished, resulting in a very slowly decaying oscillating integrand. As expected, no surface wave poles are present in (6.35) and consequently no pole extraction needs to be performed. However, the main obstacle of the branch point $k_z = 0$ is present even in this elementary GF (6.35) due to the radiation condition as $|z| \to \infty$. For demonstration purposes, a free-space wavenumber $k = 1[rad/m]$ is assumed.

Regarding the evaluation of (6.9) for $n = 0$, the following analytical solution can be obtained, which will be considered as a reference:

$$\mathcal{I}_{0,a} = \int_0^k \tilde{G}_V^x \mathrm{J}_0(k_\rho \rho) k_\rho dk_\rho = \frac{1}{2\pi} \frac{\sin(k\rho)}{j\rho}. \tag{6.40}$$

Afterwards, a certain threshold for the accuracy of the numerical evaluation of the integral (6.40) is set. Then the number of points of the DE rule are gradually increased until the estimated error is below the selected threshold, guaranteeing the accuracy of the numerical integration. Fig. 6.3 depicts the behavior of the error estimator for a wide span of horizontal distances ρ and for two different accuracy thresholds, a low one (Error $< 10^{-6}$) and a higher one (Error $< 10^{-14}$).

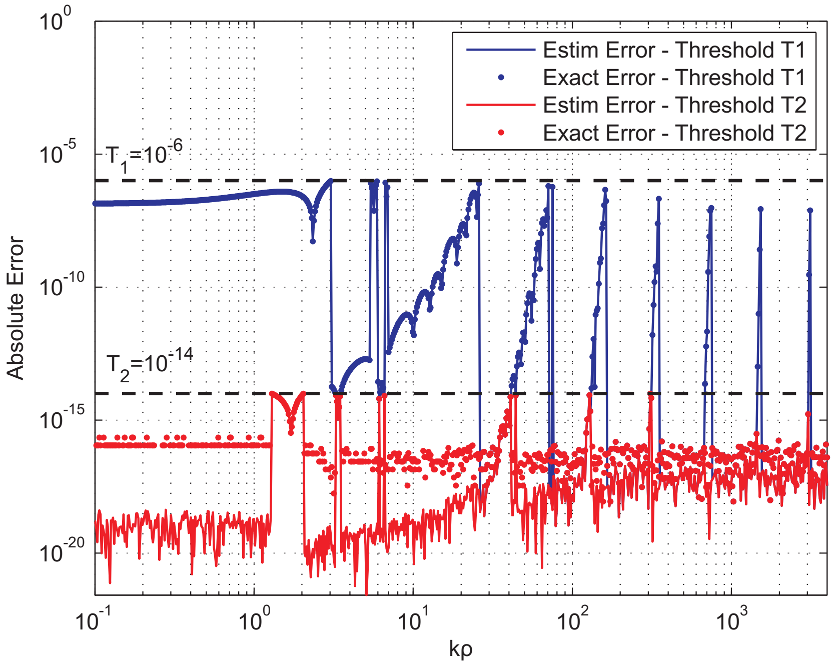

Figure 6.3: Exact and estimated absolute error of $I_{0,a}$ (6.40) for two different thresholds of accuracy.

The exact error is also included in Fig. 6.3. It shows a very accurate performance of the error estimator used, even up to 15 decimal digits, which is very close to the limit of the double precision accuracy of the machine. Below this threshold, the difference between the exact and the estimated error is only due to the limited numerical precision of the machine. Indeed, it has been shown the error estimator performs well even for accuracies up to 400 decimal digits for several numerical test cases [129].

As a second example, $\tilde{G}_V^x$ is used in the evaluation of the integral $\mathcal{I}_{0,b}$ (6.10) and the separation point between the first part and the tail of the Sommerfeld integral ξ_0 is arbitrarily chosen to be $\xi_0 = 2k$:

$$\mathcal{I}_{0,b} = \int_{k}^{2k} \tilde{G}_V^x \mathrm{J}_0(k_\rho \rho) k_\rho dk_\rho \tag{6.41}$$

Lack of an analytical solution forces a numerical evaluation of the integral (6.41) up to machine precision and the resulting values are used as a reference for the calculation of the so-called in this case "exact error".

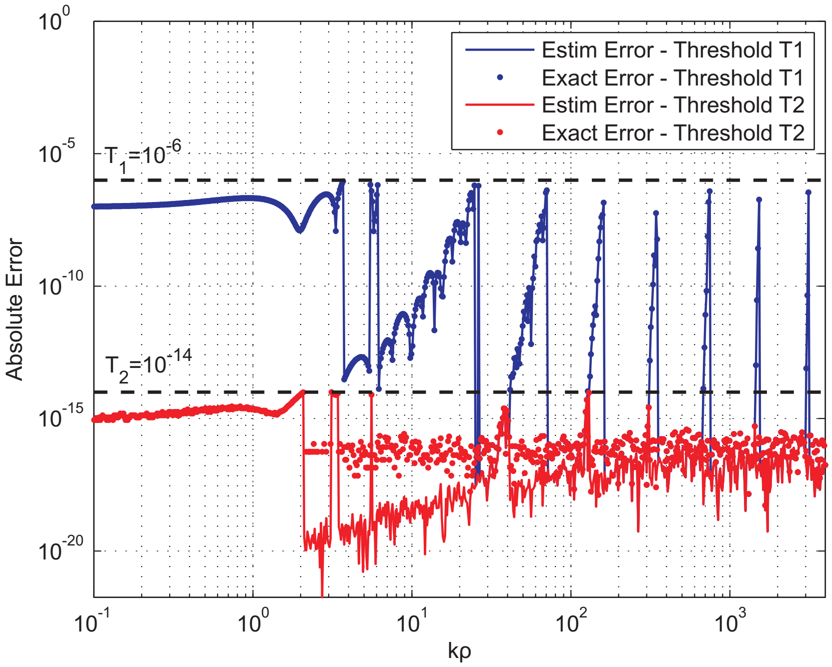

Figure 6.4: Exact and estimated absolute error of $I_{0,b}$ (6.41) for two different thresholds of accuracy.

Similar to the results of Fig. 6.3, the estimation of the error coincides with the exact error as shown in Fig. 6.4, concluding that the DE quadrature rule, accompanied by its error estimator, provides a reliable tool to predict the accuracy of the numerical evaluation of the first part of Sommerfeld integrals.

Finally, as a last example, the ρ derivative of the Sommerfeld identity is used for the computation of the integral $\mathcal{I}_{1,a}$ (6.9). This case respresents the magnetic field H created by an $\hat{x}$ directed electric dipole on the perpendicular plane yz. The spectral domain GF $\tilde{G}_{HJ}^{zx}$ can be written as:

$$\tilde{G}_{HJ}^{zx} = \frac{1}{4\pi} \frac{\mathrm{e}^{-j\sqrt{k^2-k_\rho^2}|z-z'|} k_\rho}{j\sqrt{k^2-k_\rho^2}} \tag{6.42}$$

having an analytical solution for $\mathcal{I}_{1,a}$ if the dipole and the observation position are aligned, i.e. $z = z'$:

$$\mathcal{I}_{1,a} = \int_0^k \tilde{G}_{HJ}^{zx} \mathrm{J}_1(k_\rho \rho) k_\rho dk_\rho = \frac{1}{4\pi} \frac{-k\rho \cos(k\rho) + \sin(k\rho)}{j\rho^2}. \tag{6.43}$$

The performance of the estimated error compared to the exact error is shown in Fig. 6.5, where the two errors coincide almost up to machine precision accuracy.

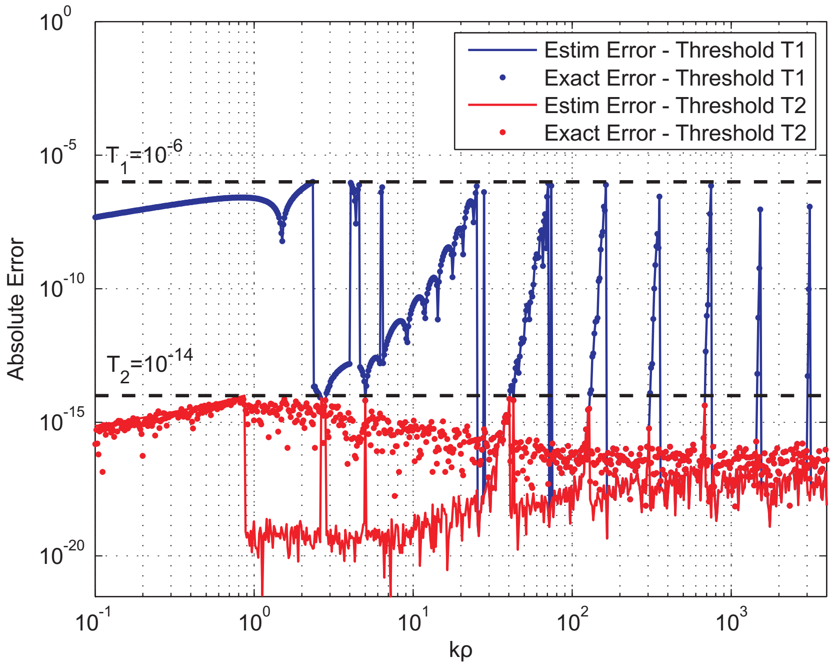

Figure 6.5: Exact and estimated absolute error of $I_{1,a}$ (6.43) for two different thresholds of accuracy.

Although the accuracy of the error estimator has already been depicted through the previous test cases, the computational time acquired to evaluate the value of the integral and its estimated error will determine the potential of the proposed technique.

For this reason, $\mathcal{I}_0$ (6.8), being the sum of (6.40) and (6.41), is computed using the elliptically deformed integration path proposed in [75]. The numerical integration is performed in a single core of a Q9550@2.83GHz processor using the `quadgk` routine of Matlab 7.12.0 (R2011a). `quadgk` is a vectorized adaptive implementation of a Gauss-Kronrod (GK) quadrature and for the considered cases by far the fastest integration routine provided by Matlab [143]. Using the same software and hardware configurations, $\mathcal{I}_0$ is also calculated utilizing the proposed DE rule and its accompanying error estimator. Computation times for different accuracies for the two methods are shown in Fig. 6.6.

For small values of the $k\rho$ product, the convergence to highly precise results is very fast with both methods and thus no significant acceleration is observed. However, as the horizontal distance ρ increases, the proposed method becomes more efficient and an error smaller than 10^{-14} for a value $k\rho = 3000$ is reached 10 times faster than with the reference method. It should be pointed out that the additional time required for the extraction of the poles of the

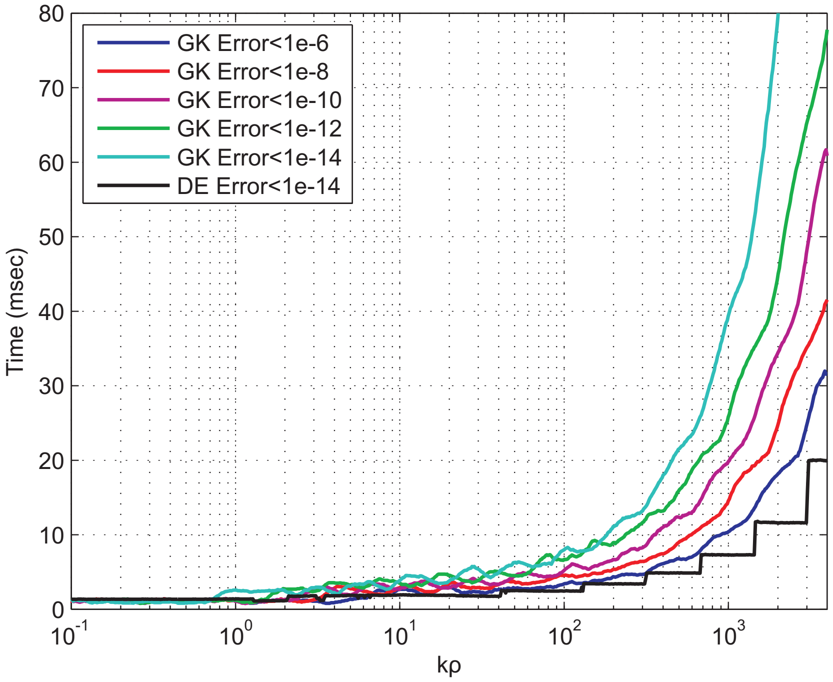

Figure 6.6: Computational times of the first part of the Sommerfeld integral $\mathcal{I}_0$ (6.8) for the GF of the scalar potential of an electric dipole (6.38), using GK and DE methods for different levels of accuracy.

GF $\tilde{G}$ is negligible, an action that is performed only once for all the distances ρ. Moreover, the efficiency of the proposed method can be highlighted even more. Within the time that the reference method needs to reach an accuracy of 10^{-6}, the proposed method has already guaranteed an accuracy lower than 10^{-14}, especially for large values of the $k\rho$ product, as shown in Fig. 6.6.

6.5.2 Dielectric slab

As another benchmark for the proposed method, we choose a multilayered structure that consists of three stacked layers: layer #1 is PEC, layer #2 is a lossy dielectric with $\epsilon_r = 4.4 - j0.352$ and thickness $d = 10$ mm and layer #3 is the semi-infinite free space. The operating frequency of a horizontal source located on the interface between the lossy dielectric and the air is 10 GHz. In this example we focus on the computation of G_A^{xx}, which as already shown in Table 4.12, has only TE poles, if any. The observation point is also placed on the interface as this is the most challenging computational case for Sommerlfeld integrals, as already explained in Section 6.5.1. This certain example has received remarkable attention within the CEM community [71, 144]. It has poles in the complex plane, indeed a TE surface wave pole exists at $k_{\rho 1}^{TE} = (1.7418 - j0.0909)k$. The losses of the dielectric do not permit the assumption that after some wavelengths of horizontal separation between the source and the observer the surface wave pole contribution is the dominant one, as quite fast the losses force a $1/\rho^2$ decay. In [144], the CIM method [145] is combined with an imaginary axis

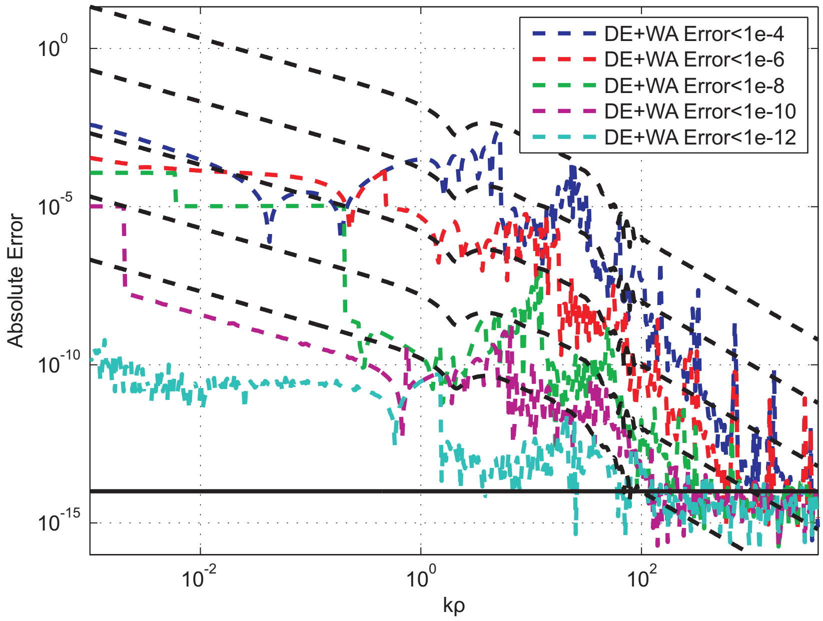

Figure 6.7: Absolute error of G_A^{xx} of the proposed method for the structure of Section 6.5.2 for different levels of predefined relative error.

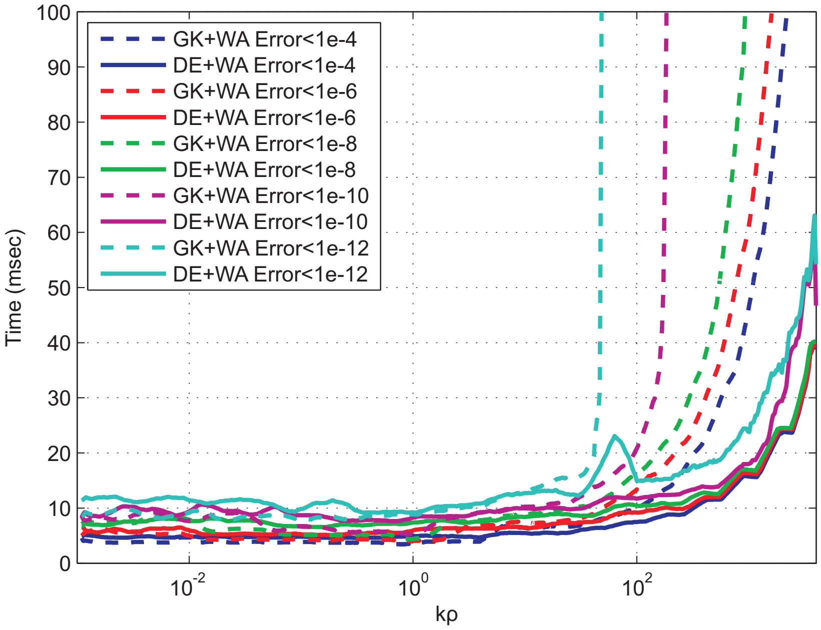

Figure 6.8: Computational times of the proposed DE and WA algorithm (solid lines) and the reference detour and WA method (dashed lines) for different levels of predefined relative error for G_A^{xx} for the structure of Section 6.5.2.

integration of the Sommerfeld integral [76] in order to derive the spatial domain GFs for moderate horizontal distances of some wavelengths. Alternatively, a special three-level DCIM approach was proposed [71] in order to enhance the efficiency of CIM. However, both methods do not guarantee controllable and increased accuracy of the results, an inherent issue of CIM method. The same exactly geometry is solved with the proposed method based on the combination of the DE and WA algorithms for different levels of relative accuracy. The results are shown in Fig. 6.7, where the black dashed lines show the different predefined relative errors in terms of absolute error for different horizontal distances ρ. The colored lines show the true absolute error when compared with a reference solution. The additional black solid line indicates the numerical limit for double precision arithmetics, below which the round off errors and the exactness of the reference solution are under question.

The comparison concerning the computational time of the proposed method against the detoured integration [75] which we use a reference in this chapter is shown in Fig. 6.8. Similar behavior to the simple free space case of Fig. 6.6 is observed in this far more complicated structure. The time shown in Fig. 6.8 includes both the DE and the WA algorithm calculations, thus accounting for the total time to derive the spatial domain GF. For short horizontal separation between the source and the observation points, the two methods perform almost equivalently. As the horizontal distance increases, then the proposed method outperforms the reference one, which for even moderate relative accuracies fails. Finally, the vector potential

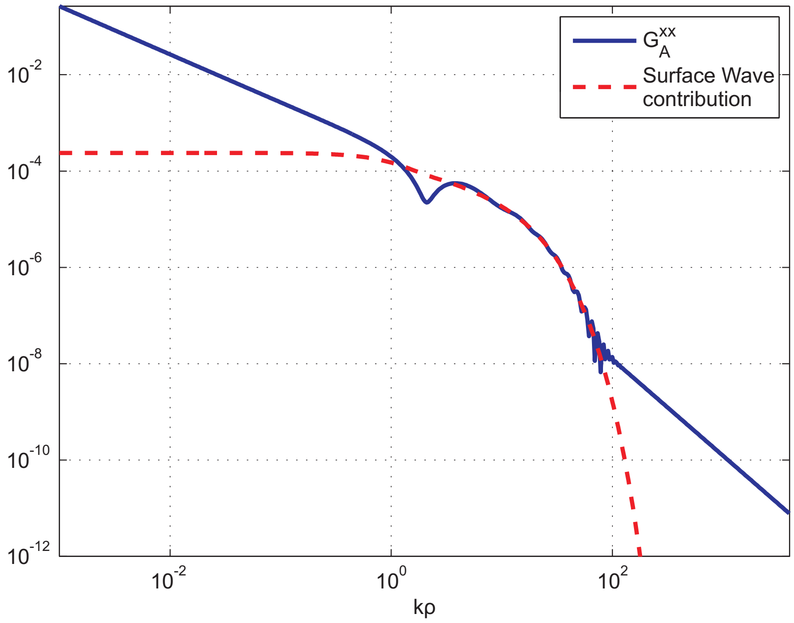

Figure 6.9: Spatial domain G_A^{xx} for the structure of Section 6.5.2. The contribution of the surface wave pole is also indicated.

G_A^{xx} is plotted in Fig. 6.9, alongside with the contribution of the surface wave pole. As already stated in [71], the surface wave contribution will become dominant only within a certain range of horizontal distances. Similar results have been obtained with the three-level DCIM method [71], within shorter computational times but sacrificing the guaranteed numerically accuracy.

6.5.3 Graphene sheet

The last example for the evaluation of the Sommerfeld integrals includes a graphene sheet that is excited by an electric dipole above it, as shown in Fig. 4.14. This example is of high scientific and technological interest as it can support a plasmon mode propagating along the surface of the graphene. The presence of the surface plasmon mode is reflected in the spectral domain GFs of the structure as a surface pole as already discussed in Chapter 4 subsection. There, the various components of the spectral domain GFs for the fields and the potentials have been derived. With this example, their spatial domain counterparts are calculated efficiently using the numerical techniques presented in this Chapter.

The excitation of the structure of Fig. 4.14 by a vertical electric dipole is of extreme interest. In general, the excitation of a plasmon mode on a surface is quite challenging due to the orders of magnitude difference between the wavevectors of the plasmon and the free space one. Recent work found in [113, 146, 147] shows that a very precise placement of a vertical dipole over the graphene layer can efficiently couple the free space radiation to the plasmon. It becomes evident that a fast and accurate computation of the spatial domain GFs is extremely valuable.

Spatial domain GFs of structures that include graphene sheets have already been presented in Chapter 4 in Fig. 4.19 and in Fig. 4.20 for a horizontal and a vertical dipole excitation, respectively and were cross checked with relevant publications. Open question remains how efficiently and how accurately these spatial GFs have been calculated through their respective Sommerfeld integrals.

Assuming a $\hat{z}$ directed dipole, only a TM pole is present in the $\hat{z}$ component of the spectral domain electric field GF $\tilde{G}_{EJ}^{zz}$, as indicated in Table 4.12 combined with (4.95). The position of the pole, for the case that the graphene sheet is floating in the air, i.e. $\epsilon_1 = \epsilon_2 = \epsilon_0$, is readily available in closed form (4.98). If the position of the pole cannot be found analytically, a numerical algorithm for finding the zeros of (4.96a), (4.96b), or even (4.97) in case of tensorial conductivity of the graphene, should be used.

In the current example an operating frequency of 10THz is chosen, while the graphene layer is set at 300K, with a chemical potential of 0.2eV and a relaxation time of 1ps. The model of Kubo formula is used to estimate the macroscopic isotropic graphene conductivity [111], which under these conditions is found to be $\sigma = 8.736\mathrm{e}^{-6} - j3.708\mathrm{e}^{-4}[S]$. Then, according to (4.98), the single TM pole is located at $k_{\rho 1} = (14.333 - j0.336)k$ and $\tilde{G}_{EJ}^{zz}$ is written as:

$$\tilde{G}_{EJ}^{zz} = -\frac{\eta}{2}\frac{k_\rho^2}{k_z}\frac{e^{jk_z(z-z')}}{k + \eta\sigma/2k_z} \tag{6.44}$$

where $\eta = \sqrt{\frac{\mu_0}{\epsilon_0}}$, z' is the vertical position of the source, which is assumed to be above the graphene sheet, and z the vertical position of the observation point, assumed to be below the graphene sheet in the current example [148].

The spatial domain GF G_{EJ}^{zz} is linked through the Sommerfeld integral, based on the Table 4.1:

$$G_{EJ}^{zz} = S_0[\tilde{G}_{EJ}^{zz}]. \tag{6.45}$$

As already mentioned in 6.5.1, the computationally most challenging case in the numerical evaluation of (6.45) is when both the source and the observation point are attached on the graphene, i.e. $z = z'$, in the current example on opposite sites of the sheet.

The integration of (6.45) over a detoured path [75], which joins the real axis at a point $\xi_0 > \text{Re}\{k_{\rho 1}\}$ in order to avoid the pole is chosen to be the reference method for comparison. The implementation details of the reference method coincide with the ones described in 6.5.1. After the integration path joins the real axis, i.e. $k_\rho > \xi_0$ the WA technique discussed in Section 6.3 is used. The computational time for various horizontal distances ρ and predefined levels of accuracy are shown in Fig. 6.10 with blue lines.

The red lines in Fig. 6.10 represent the computational time needed if instead of the detoured method, the TM pole is extracted and the DE of Section 6.2 with its accompanying error estimator 6.4.1 is used. The same breakpoint ξ_0 as the reference method is used, thus the computational time dedicated to the tail of (6.45) is equivalent in both the reference and the proposed methods. Consequently, the gain in time compared to the reference method, as shown in Fig. 6.10, is attributed to the efficiency of the proposed on-the-axis integration.

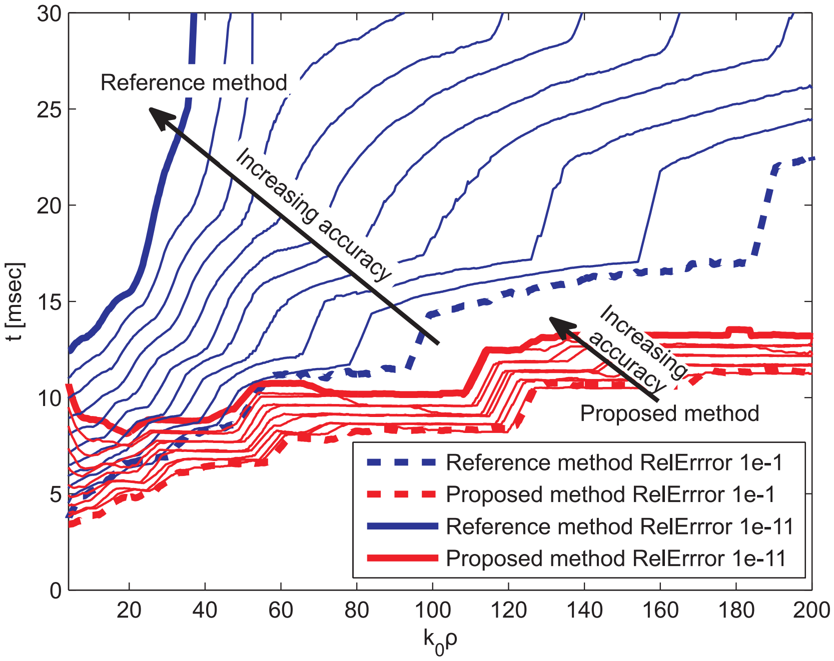

Figure 6.10: Computational time for the Sommerfeld integral of (6.45) using the detoured integration and the WA algorithm for the reference method and the DE and WA algorithms in the proposed method.

Moreover, as shown in Fig. 6.10, the reference method fails completely to provide results with high accuracy even for moderate values of ρ, while the time increase of the proposed method both for increased ρ and high accuracy remains reasonable.

The spatial domain GF (6.45) for the discussed structure has already been included in advance in Fig. 4.20 of Chapter 4. It is repeated here so that a direct link to the performance of its numerical evaluation can be easily made, as shown in Fig. 6.10.

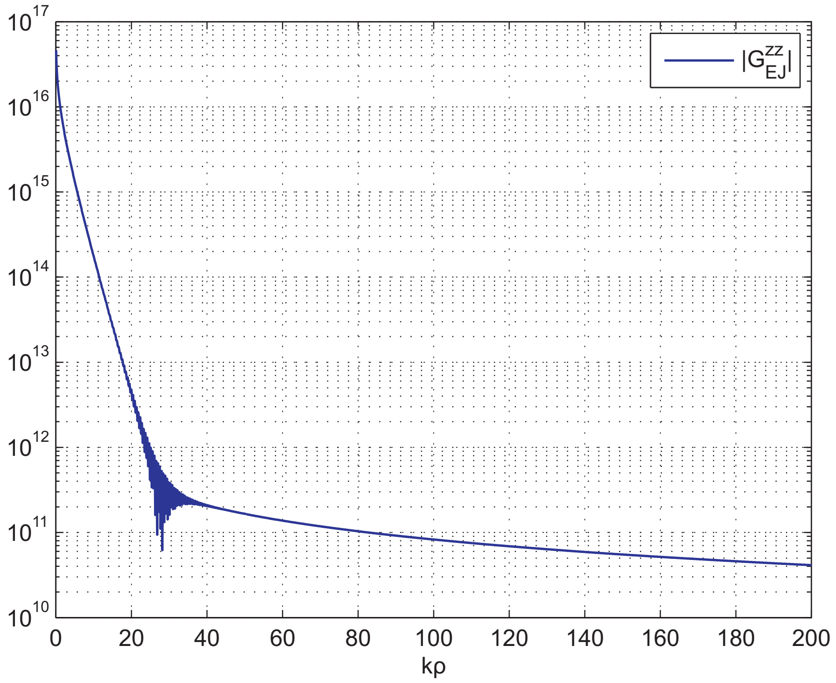

Figure 6.11: Spatial domain G^{zz}_{EJ} for the structure of Section 6.5.3.

The basic reason why the reference method really fails in this example is the position of the surface plasmon pole. As shown in Fig. 4.18, the real part of the pole can be located very far away from the branch point $k_\rho = k$, depending on the frequency and the properties of the graphene, deteriorating the performance of the detoured integration. It should be pointed out, that using the proposed method, where the poles have already been extracted, there is no reason to choose the breakpoint ξ_0 very far away from the branch point and the WA algorithm can improve the total performance of the proposed scheme even more.

6.6 Conclusion

In this Chapter, a novel numerical method for calculating Sommerfeld integrals has been discussed. It uses the DE rule for the first part of the Sommerfeld integral to handle the singularity of the branch point, while the tail is efficiently integrated with the WA method. All the numerical techniques presented in this chapter focus on obtaining fast and highly precise results. Consequently, original techniques have been developed for introducing efficient error estimators that guaranty the predefined accuracy of the results. The efficiency of the method and the details of the implementation have been demonstrated through practical examples.

Improvements of several orders of magnitude have been observed in most cases for the achieved accuracy, while reducing frequently the computation time by at least one order of magnitude. In case, that highly accurate, close to machine precision, results are needed, traditional methods fail completely to provide the result. Even in such cases, the proposed techniques provide almost exact results within reasonable computational time. The techniques presented here remain valid and competitive for all the components of the spatial domain GFs that involve Sommerfeld integrals, even for very complicated multilayered structures combining both finite thickness layers and zero thickness impedance sheets, under the condition that the position of the poles, surface waves or plasmons, can be identified.

7 Reaction Integrals in Surface Integral Equations

In the context of Mixed Potential Integral Equation (MPIE) formulations, efficient ways for deriving the spectral domain GFs of arbitrary multilayered structures including multiple thin dielectric interfaces have been developed in Chapter 4. Their space domain counterparts are derived up to the desired numerical accuracy through the numerical algorithms presented in Chapter 6. Having the spatial domain GFs of the complex medium available, the next step in the IE-MoM code is to evaluate the reaction integrals that fill the MoM matrix. In most MoM implementations like Galerkin, the reaction integrals of the Surface Integral Equations are 4-D, due to the integration of the 2-D source domain on the 2-D observation domain. Only if the source and observation domains are rectangular and strictly in the static case, these 4-D integrals can be calculated analytically. In the dynamic case, this is not any more possible [82]. One of the greatest advantages of MPIE, as discussed in Chapter 2 [2], is the lower order singularities that appear in the kernels of the reaction integrals. Though the weak singularity is much easier to be treated numerically than the stronger singularities of EFIE and CFIE, specialized algorithms still need to be developed to improve the performance and the accuracy of the computation of the reaction integrals in MPIE.

In general, one of the most popular methodologies found in the literature for treating these MoM reaction integrals is based on the separation of the 4-D reaction integral in two cascaded 2-D integrals covered in Section 7.1. The integration of the inner 2-D integral, often called the potential integral, has received extensive attention and various strategies have been proposed to handle the singular kernel [82, 83, 86, 87, 97] and is considered already quite mature. The potential integral remains continuous all over the observation domain, and for this reason standard GL quadrature rules have been used for this integration. But despite the continuity of the potential, its higher order derivatives remain unbounded on the common edges between the source and the integration domain. This explains the poor performance frequently observed in the outer 2-D integration. This difficulty is overcome in Section 7.2, where an original modification of the Double Exponential quadrature rule, described in Chapter 5, is utilized in the current work [130]. An additional improvement of the DE rule that still guarantees numerical exact results but shows faster convergence is also proposed [138, 149]. Finally, in Section 7.3, the advanced performance of the proposed method is validated through numerical examples and compared to reference values that are obtained through alternative numerical techniques like the Direct Evaluation Method [92].

7.1 Weakly Singular Integrals

The Galerkin discretization of MPIE formulations requires efficient and accurate computation of the inner products filling the MoM impedance matrix. In this case, the inner products are 4-D integrals representing interactions between 2-D source and observation domains. If div-conforming basis functions are chosen, these inner products can be decomposed in simpler ones [150], among which we frequently encounter the expression:

$$\mathrm{I} = \int_{E_P} \mathbf{f}_P(\mathbf{r}) \cdot \int_{E_Q} \frac{e^{-jk|\mathbf{r}-\mathbf{r}'|}}{|\mathbf{r}-\mathbf{r}'|} \mathbf{f}_Q(\mathbf{r}')\, dx. \tag{7.1}$$

Obviously, $\mathbf{r} \in E_P$ and $\mathbf{r}' \in E_Q$, E_P and E_Q being the observation and source area, respectively, whereas $\mathbf{f}_P$ and $\mathbf{f}_Q$ are linear scalar or vector basis functions into which the original sources can be decomposed. When the observation and the source domain coincide or share some common points, the kernel of the inner product becomes weakly singular due to the presence of the $1/|\mathbf{r}-\mathbf{r}'|$ term and a special treatment is necessary.

In (7.1) e^{-jkR}/R, $R = |\mathbf{r}-\mathbf{r}'|$, is the free space spatial MPIE GF. Although the actual MPIE GF can have a much more complicated expression, e.g. a Sommerfeld integral as extensively discussed in Chapter 4, the free space GF is also, save for a constant, the singular part of any MPIE GF. Therefore, we will use it in this chapter without loss of generality, while keeping the mathematical details simpler and highlighting the numerical issues and the way they can be overcome.

One very common technique is the separation between the integrations of the source (7.2) and the observation domain (7.3):

$$I_Q^{\text{potential}}(\mathbf{r}) = \int_{E_Q} \mathbf{f}_Q(\mathbf{r}') \frac{e^{-jk|\mathbf{r}-\mathbf{r}'|}}{|\mathbf{r}-\mathbf{r}'|}\, dA_Q, \tag{7.2}$$

$$I = \int_{E_P} \mathbf{f}_P(\mathbf{r}) I_Q^{\text{potential}}(\mathbf{r})\, dA_P. \tag{7.3}$$

Many methods have been developed for tackling the potential integral (7.2), the most popular ones being the singularity cancelation and singularity subtraction techniques. The singularity cancelation technique is based on a suitable transformation of variables that through its Jacobian cancels exactly the singularity $1/|\mathbf{r}-\mathbf{r}'|$. Classical choices are the polar coordinates [81] and the Duffy [151] transformation. More sophisticated choices include transformations that map the original domain to a rectangular domain which is more suitable for 2D quadrature rules [82, 83]. Singularity substraction techniques include the splitting of the singular integrand in two different functions. The first one includes the singularity and can be analytically integrated and the second one is the remainder that is treated numerically using standard integration techniques due to its smooth behavior [150, 152].

It should be mentioned that both singularity cancelation and subtraction techniques end up with integrals that can either be computed analytically or they are smooth and consequently interpolatory GL quadratures can be used very efficiently.

While the inner integral (7.2) has been studied in detail and efficient methods are at hand to compute it, the outer integral (7.3) received less attention. Regarding its numerical integration, since it is not singular any more, it is traditionally treated applying standard GL rules. However, it has already been pointed out by researchers that the higher order derivatives of the potential $I_Q^{\text{potential}}$ are not bound on the common edges between the source and the observation domain [85]. This characteristic is shown in Fig. 7.1, where the real part (the imaginary part is smooth) of the potential integral $I_Q^{\text{potential}}(\mathbf{r})$ for a constant distribution over the triangular source domain E_Q is plotted for different positions $\mathbf{r}$ of the observation point. The observation point $\mathbf{r}$ can lie inside or outside the source domain E_Q, spanning the observation domain E_P.

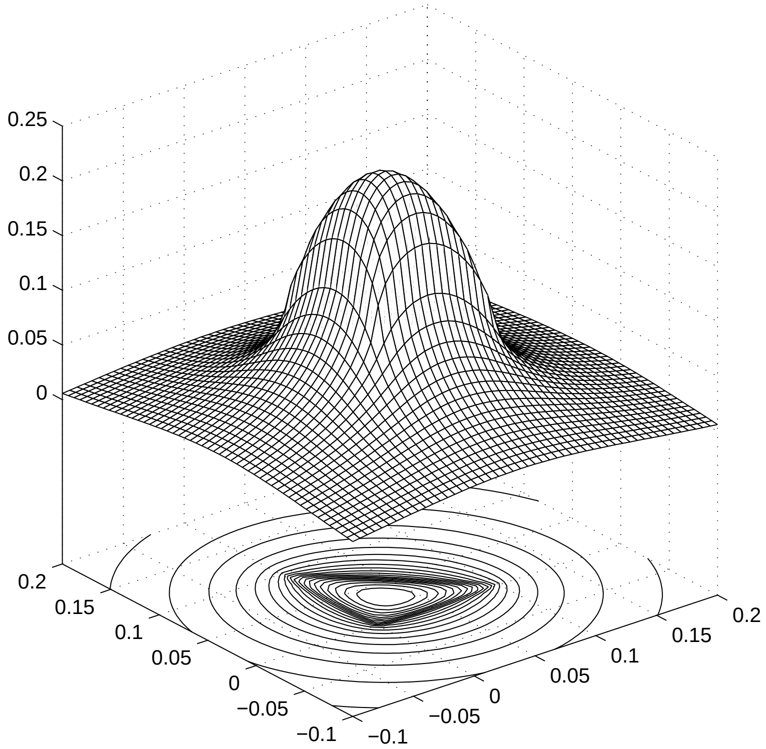

Figure 7.1: Real part of the potential integral (7.2) for a triangle with vertices $\mathbf{r_1} = [0,0,0]$, $\mathbf{r_2} = [0.1,0,0]$, $\mathbf{r_3} = [0,0.1,0]$ and for $\lambda = 1[m]$. The basis function $\mathbf{f}_Q(\mathbf{r}')$ is taken as constant over the source domain E_Q.

Thus, the efficiency of the GL quadratures, which are exact for integrating polynomial functions, is deteriorated and special care should be taken so as to boost the performance of these calculations.

For this reason, specialized quadratures for the outer integral (7.3) are elaborated, with the DE quadrature rule, discussed in Chapter 5, being one of the most promising candidates.

7.2 Outer Integral

In the current work we focus on the efficient integration of the outer 2-D integral (7.3). Referring to Fig. 7.1, the potential integral (7.2) remains continuous, though higher order derivatives become unbounded on the edges of the source domain. Moreover, depending on the relative position between the integration domain E_P and he source domain E_Q, the unbounded derivatives will be present on all the edges of the integration domain in the case of the self term. If E_P and E_Q are edge adjacent domains, the irregularity will remain only on the common edge and finally in the case of vertex adjacent, it shrinks to just one point. Not to mention the near singular case, when source and observation domain do not share any common points but they are very close one to the other, so that the derivatives of (7.3), though bounded in the strict numerical sense, they may get very high values and consequently downgrade the behavior of GL quadratures according to (5.5) and the discussion in Section 5.2. This is a situation like to appear in graphene and solar cell related technology, where the two sides of a thin layer are metallized. Another potential application is in the EM analysis of suspended stripline components if the dielectric substrate is very thin as in [153].

The Double Exponential (DE), already utilized in Chapter 6 for the efficient numerical integration of Sommerfeld integrals, could be useful for the outer integration of the 4-D reaction integrals presented in this Chapter. However, the integration domain is now a surface and therefore 2-D DE quadratures based on the 1-D of (5.16) have to be developed, as discussed in the following sections.

7.2.1 Cartesian Product Rules

Building a 2-D or even a 3-D integration rule is not always a straightforward procedure. If the integration domain is rectangular, then a Cartesian product of two 1-D integration rules provides a satisfactory distribution of integration points over the surface to be integrated. Following this procedure, 2-D quadrature rules are shown in Fig. 7.2 (a) and (b) based on 1-D GL and DE rules, respectively. Quite often, the integration domain is chosen to be triangular, a very common approach in modern EM meshing tools due to the better approximation of the geometry with triangles rather than with rectangles. In this case, an optimized quadrature rule is in general difficult to be found. For GL quadratures, such a rule has been developed in [154] and provides the performance of the Cartesian product GL rule but with less integration points.

Based on the philosophy of [154], 2-D DE quadratures originally tailored to triangular domains were developed in [155] and [156]. The integration interval is divided into subdomains and through a specific search pattern the abscissas and the weights of the rule are found. The disadvantage of these methods is that the search algorithm is kernel specific, so for each triangle the integration rule has to be rather redeveloped than just scaling and shifting a predefined set of points. For this reason, Cartesian product rules are used in the current work to develop 2-D DE rules, although suboptimal in terms of distribution of integration points over the triangular domain. The distribution of the points of such a rule, alongside with the GL ones are shown in Figs. 7.3 (a) and (b), respectively. For the rest of this work, only triangular elements for the source and the observation domain will be considered and

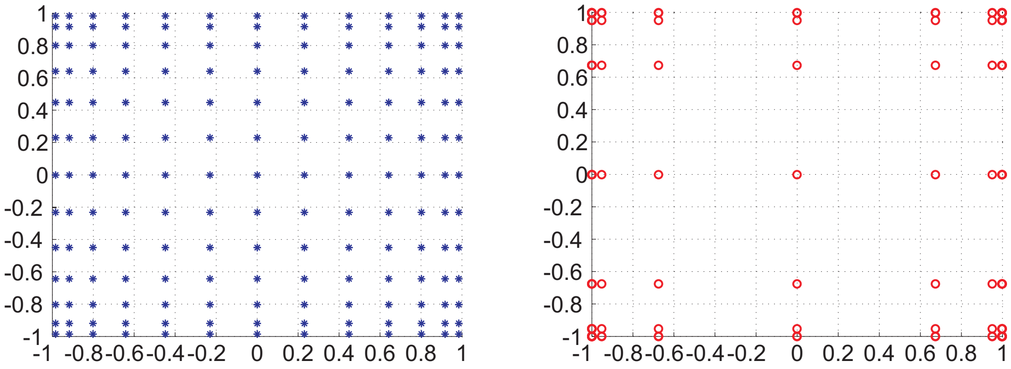

(a) 169 points GL rule.

(b) 169 points DE rule.

Figure 7.2: 2-D quadrature rules based on Cartesian products.

the conclusions can be straight-forwardly applied to rectangular domains if necessary.

7.2.2 DE performance

The triangular source domain with a constant distribution as shown in Fig. 7.1 will be considered as the reference test case for developing an efficient integration method for the outer integration (7.3) of the reaction integrals in MPIE. Some preliminary results on squared patches for static and dynamic cases can be found in [91, 130]. The usual choice of the GL quadratures will show a poor performance due to the unbounded derivatives of the integrand on the edges of the integration domain as clearly shown through the contour lines of Fig. 7.1.

A reference result for the 4-D reaction integral of the selfterm of this triangle is calculated through the Direct Evaluation method [92], an alternative method based on the re-ordering of the integrals and a very specific decomposition. Having available the reference solution, the comparison of the accuracy for different number of integration points for GL and DE results is shown in Fig. 7.4. GL rules show a very slow convergence which barely reaches single precision accuracy if a lot of integration points are used. On the other hand, the DE rule is able to get numerically exact results, up to the double precision arithmetic of the machine that the computations were performed. Quite similar behavior of the GL and the DE 2-D rules is found for a variety of cases, including normal and stretched triangular domains, self terms and edge adjacent interactions as shown in Figs. 7.7, 7.8, 7.9 and 7.10. It can be safely concluded that the proposed DE rules are able to numerically handle the outer integration of the reaction integrals and retrieve very precise numerical results.

In the never-ending campaign for efficient and accurate numerical algorithms, any improvement of the already developed methods is of outmost importance. As such, the numerical integration of the outer triangles of the reaction integrals based on the Cartesian products of DE rules can be accelerated, if the original DE rule of (5.16) is modified as proposed in the Section 7.2.3. The basic motivation is to accelerate the convergence of the DE rule in

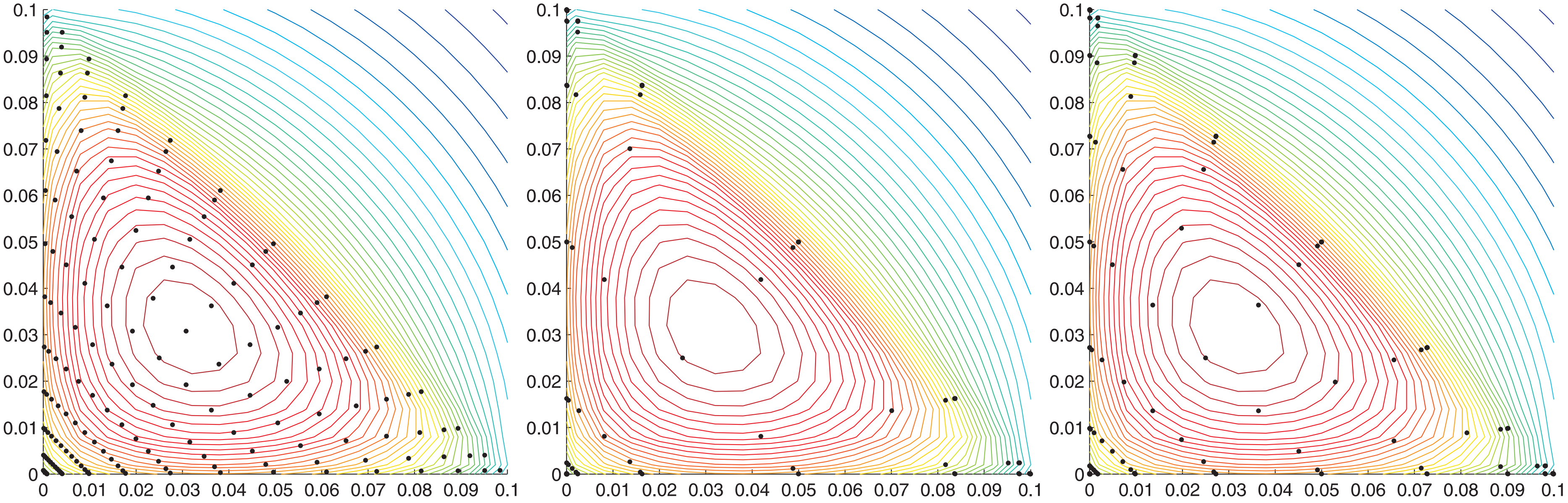

(a) 169 points GL rule. **(b)** 169 points DE rule with $\alpha = 0.5\pi$ (original DE). **(c)** 169 points DE rule with $\alpha = 0.3\pi$ (modified DE).

Figure 7.3: Sampling points of (7.3) using 2D Cartesian product rules of GL, original DE and modified DE quadratures (from right to left).

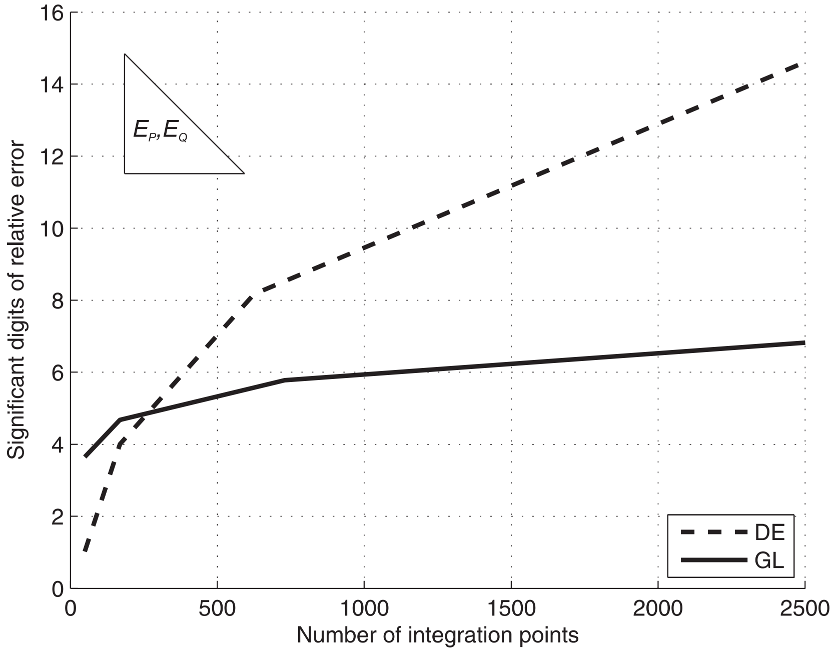

Figure 7.4: Real part of (7.3) using Cartesian product rules of DE and GL quadratures and employing [82] up to numerically exact results for the inner quadrature (7.2). The integration domains E_P and E_Q coincide with the triangle shown in Fig. 7.1.

cases where the computationally expensive double precision results are sacrificed in terms of performance.

7.2.3 Improvements in DE quadratures

The trapezoidal formula is proven to act as a very fast convergent rule for integrals of analytic functions over $(-\infty, \infty)$ and it contributes to the advanced performance of the DE quadrature rule [126]. However, if only a few sampling points are evaluated - although these samples can be arbitrarily close to the irregular areas - the discretization error in the smooth areas of the integration domain is increased. In Fig. 7.3 the real part of the potential integral is represented with isolines (the source domain is the triangle of Fig. 7.1) while the sampling points of the observation domain, being the same as the source domain, are marked with dots. The points of the GL rule in Fig. 7.3 (a) cover the surface of the observation area in a quite satisfactory way, though they do not approach closely enough the irregular edges of the domain. On the other hand, in Fig. 7.3 (b) the original DE rule concentrates points arbitrarily close to the problematic edges, while the smooth area in the middle of the observation domain remains under-sampled. A transformation that concentrates more points in the smooth areas of the integration domain but keeps at the same time the DE convergence of its first derivative (5.15) could serve as an efficient replacement of the original DE rule.

One suitable approach is the modification of the basic DE transformation (5.14) allowing the introduction of the parameter α (originally $\alpha = \frac{\pi}{2}$) in the following way:

$$x = \phi(t) = \tanh\left(\alpha \sinh(t)\right) \tag{7.4}$$

and

$$\phi'(t) = \frac{\alpha \cosh(t)}{\cosh^2\left(\alpha \sinh(t)\right)}. \tag{7.5}$$

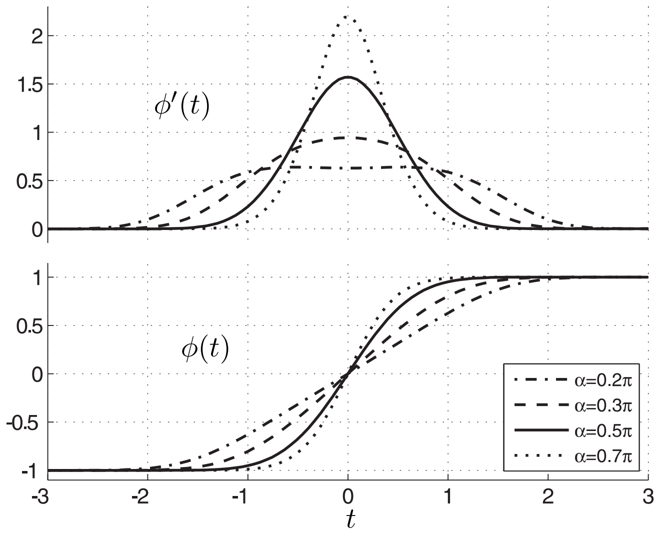

Figure 7.5: Modified DE transformation (7.4) and its accompanying derivative (7.5) for different values of the parameter α.

It is obvious from transformation (7.4) that for values $\alpha > \frac{\pi}{2}$, sampling points are even more concentrated close to the non smooth edges, deteriorating further the approximation of the smooth area in the center of the triangle. On the other hand, for $\alpha < \frac{\pi}{2}$ the smooth areas are not so sparsely sampled any more, while there are still samples very close to the irregular edges. Thus, choices of $\alpha < \frac{\pi}{2}$ are expected to improve the behavior of the cubature. In Fig. 7.3 (b) and (c), one can observe the comparison of the sampling points between the original DE rule with $\alpha = 0.5\pi$ and the modified one with $\alpha = 0.3\pi$ where the trend previously described can easily be noticed. However, if α becomes too small, then the sampling rate in the irregular edges of the triangle is not dense enough and the efficiency of the DE quadratures is expected to deteriorate.

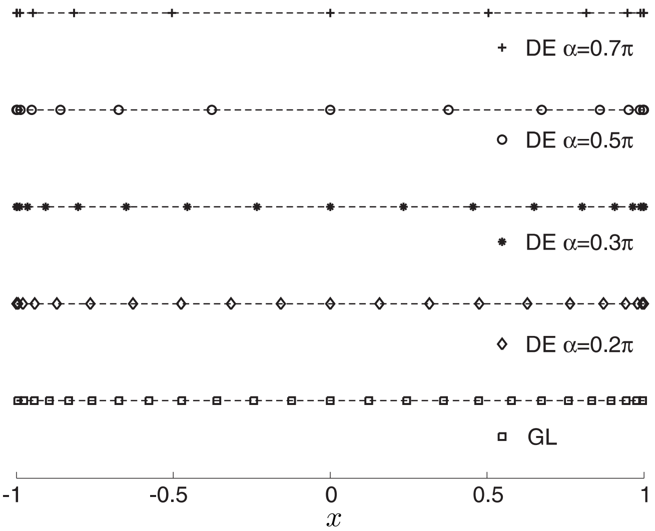

Figure 7.6: Distribution of integration points over the reference domain $[-1, 1]$ for the modified DE rule for different values of the parameter α. For comparison purposed, the abscissas of a GL rule with the same number of integration points as the DE rule with $\alpha = 0.5\pi$ is also shown.

M	0	1	2	3	4	5	6	7
h	1	1/2	1/4	1/8	1/16	1/32	1/64	1/128
N $\alpha = 0.2\pi$	9	17	33	65	131	261	521	1043
N $\alpha = 0.3\pi$	7	15	29	59	117	235	469	939
N $\alpha = 0.5\pi$	7	13	25	51	101	203	405	809
N $\alpha = 0.7\pi$	5	11	23	45	91	181	361	723

Table 7.1: Number of integration points N for the level M of the proposed DE rule (7.4) where the discretization step is h. These values are valid for double precision arithmetic units and they serve as an extension of the Table 5.1 for the original DE rule.

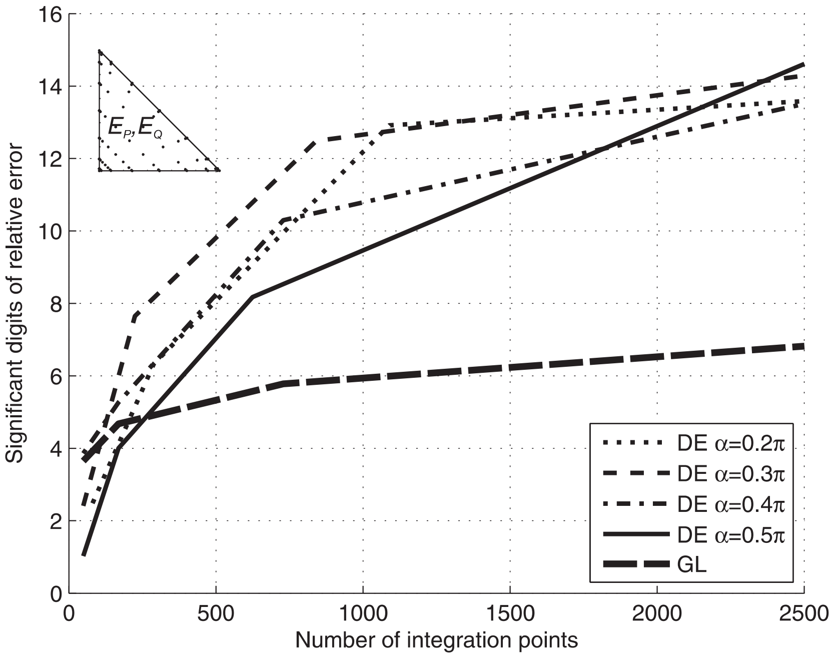

Figure 7.7: Number of correct digits of the real part of the self term of (7.3) for a triangle with vertices $\mathbf{r_1} = [0, 0, 0]$, $\mathbf{r_2} = [0.1, 0, 0]$, $\mathbf{r_3} = [0, 0.1, 0]$ and for $\lambda = 1[m]$.

Regarding this trade-off, the choice of the value of the parameter α strongly depends on the integrand $f(x)$ and consequently on its transformed form $f(\phi(t))$. For the weakly singular integrals (7.1) discussed in this work and since triangles of different shapes are considered in Section 7.3, both in the self-term and the edge-adjacent case, the choice of $\alpha = 0.3\pi$, a numerical value not far from unity, seems to combine the preferred characteristics in a quite universal way, allowing the safe choice of this value for all the triangles produced by modern surface meshers.

7.3 Numerical Results

Since the present work focuses on the computation of the observation domain integral (7.3), the need for a machine precision evaluation of (7.2) $\forall \mathbf{r} \in E_P$ arises. For demonstration reasons, a singularity cancelation scheme is chosen, like the one proposed in [82], assuring that the quadratures used to compute (7.2) provide a highly accurate result. The 4-D weakly singular integrals were calculated to machine precision with the Direct Evaluation method [93] which was used as a reference for the evaluation of the proposed quadrature rule. In all considered cases, the parameter α is varied between 0.2π and 0.5π and the significant digits for different levels of the DE rule or equivalently for different number of integration points are plotted. Moreover, for all experiments, the test and basis functions $\mathbf{f}_P$ and $\mathbf{f}_Q$, respectively, are chosen to be constant unless explicitly specified.

Regarding the self-term, the performance of the parameterized DE rule is considered in two cases. The first one involves the right-angled triangle of Section 7.2.2, with vertices $\mathbf{r_1} = [0, 0, 0]$, $\mathbf{r_2} = [0.1, 0, 0]$, $\mathbf{r_3} = [0, 0.1, 0]$ and for $\lambda = 1[m]$ with the results included in Fig. 7.7, whereas the second case concerns the stretched triangle with vertices $\mathbf{r_1} = [0, 0, 0]$, $\mathbf{r_2} = [0.1, 0, 0]$, $\mathbf{r_3} = [-0.05, 0.087, 0]$ and for $\lambda = 1[m]$ given in Fig. 7.8. In general, the performance of quadrature rules deteriorates when the quality factor of the triangle diminishes, thus stretched triangles like the one in Fig. 7.8 should always be considered when studying or developing quadrature rules.

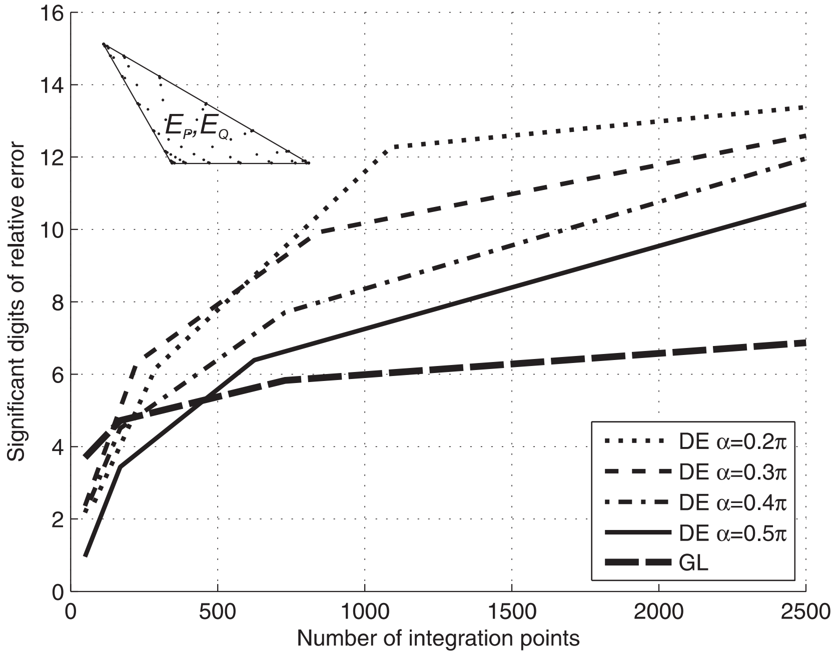

Figure 7.8: Number of correct digits of the self term of (7.3) for a triangle with vertices $\mathbf{r_1} = [0, 0, 0]$, $\mathbf{r_2} = [0.1, 0, 0]$, $\mathbf{r_3} = [-0.05, 0.087, 0]$ and for $\lambda = 1[m]$.

For both triangles, the parameterized DE with $\alpha = 0.3\pi$ achieves the fastest convergence for less than 300 integration points. It outperforms the GL rules by achieving 1 to 3 extra correct digits for the same number of sampling points, depending on the quality factor of the triangle. If extra computational resources are available, then for around 800 integration points, the improvement lies between 4 to 7 significant digits.

It is worth mentioning that there are also some other values for the parameter α close to the chosen value of 0.3π which can achieve optimum performance for some range of quality factors and number of sampling points, e.g. $\alpha = 0.2\pi$ for the triangle of Fig. 7.8. However, in terms of a general purpose choice for all the weakly singular integrals appearing in MPIE formulations $\alpha = 0.3\pi$ remains the promoted choice.

As far as the edge adjacent case is concerned, the non-smooth area includes the common edge between the two adjacent triangles. For illustrative purposes, an example involving two stretched triangles is chosen, where the source triangle is formed by the vertices $\mathbf{r_1} = [0, 0, 0]$,

$\mathbf{r_2} = [0.1, 0, 0]$, $\mathbf{r_3} = [-0.05, 0.087, 0]$ and the observation triangle by $\mathbf{r_1} = [0, 0, 0]$, $\mathbf{r_2} = [0.1, 0, 0]$, $\mathbf{r_3} = [-0.05, -0.087, 0]$, while $\lambda = 1[m]$. The behavior of the proposed rule is shown in Fig. 7.9.

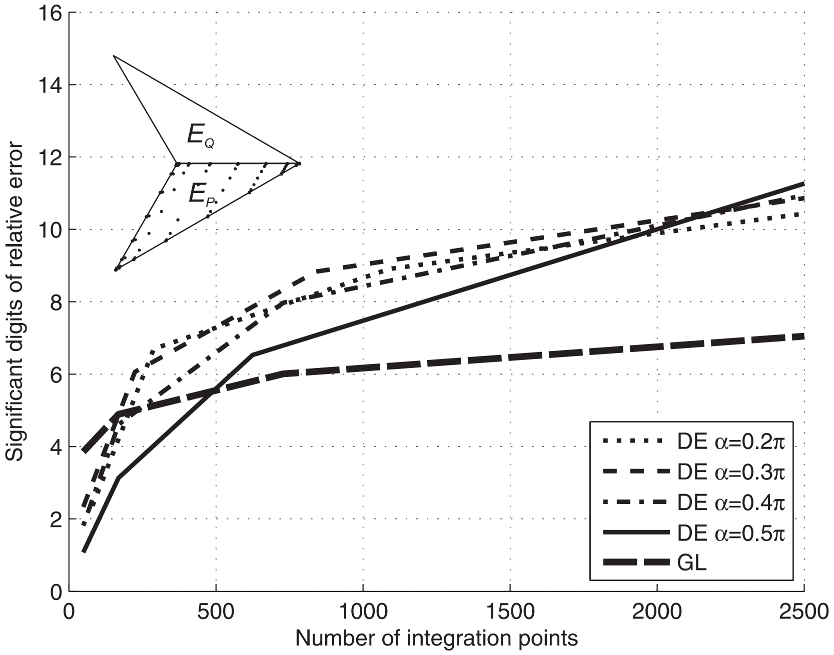

Figure 7.9: Number of correct digits of the edge adjacent case of (7.3) for triangles with vertices $\mathbf{r_1} = [0, 0, 0]$, $\mathbf{r_2} = [0.1, 0, 0]$, $\mathbf{r_3} = [-0.05, 0.087, 0]$ and $\mathbf{r_1} = [0, 0, 0]$, $\mathbf{r_2} = [0.1, 0, 0]$, $\mathbf{r_3} = [-0.05, -0.087, 0]$ for $\lambda = 1[m]$.

Finally, another edge adjacent case is shown in Fig. 7.10, where the source triangle is formed by the vertices $\mathbf{r_1} = [0, 0, 0]$, $\mathbf{r_2} = [0.1, 0, 0]$, $\mathbf{r_3} = [-0.05, 0.087, 0]$ and the observation triangle by $\mathbf{r_1} = [0, 0, 0]$, $\mathbf{r_2} = [0.1, 0, 0]$, $\mathbf{r_3} = [0, 0.1, 0]$, while $\lambda = 1[m]$. Linear basis and test functions are considered, i.e. $\mathbf{f}_P = \zeta'_{r2}\hat{u}$ and $\mathbf{f}_Q = \zeta_{r2}\hat{u}$, ζ_{r2} being the associated barycentric coordinate to the vertex $\mathbf{r_2} = [0.1, 0, 0]$.

Regarding the results of the edge adjacent case, depending on the quality factors of the involved triangles, an improvement of 1 to 3 significant digits is achieved compared to GL rules, as shown in Fig. 7.9. Moreover, comparing the parameterized DE with $\alpha = 0.3\pi$ to the original DE, the improvement in accuracy for a few sampling points is more than 3 digits. It should be noted that equivalently to the self term case discussed before, values like $\alpha = 0.2\pi$ provide a behavior as good as the chosen $\alpha = 0.3\pi$, but for uniformness reasons $\alpha = 0.3\pi$ is considered as an appropriate choice.

Summarizing the numerical results, in all the cases presented in Figs. 7.7, 7.8 and 7.9 the same trend is followed. There is an acceleration in the convergence when only a few integration points are considered as the parameter α is reduced from its original value of $\alpha = 0.5\pi$ to lower values. As soon as the approximate threshold of $\alpha = 0.3\pi$ is reached, convergence starts to deteriorate again as expected. Since different triangles for the self-term and the edge-adjacent

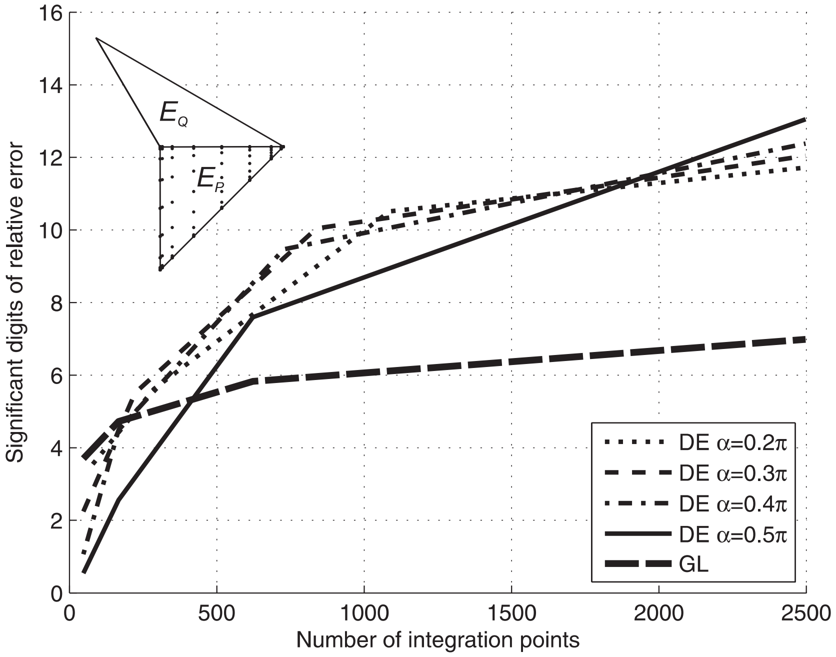

Figure 7.10: Number of correct digits of the edge adjacent case of (7.3) for triangles with vertices $\mathbf{r_1} = [0,0,0]$, $\mathbf{r_2} = [0.1,0,0]$, $\mathbf{r_3} = [-0.05, 0.087, 0]$ and $\mathbf{r_1} = [0,0,0]$, $\mathbf{r_2} = [0.1,0,0]$, $\mathbf{r_3} = [0,-0.1,0]$ for $\lambda = 1[m]$. Linear basis and test functions are considered, i.e. $\mathbf{f}_P = \zeta'_{r2}$ and $\mathbf{f}_Q = \zeta_{r2}\hat{u}$, $\zeta_{r2}\hat{u}$ being the associated barycentric coordinate to the vertex $\mathbf{r_2} = [0.1,0,0]$.

case were considered, the proposed threshold of $\alpha = 0.3\pi$ seems to be quite universal for this type of integrals and the weights and abscissas of the proposed rule can be computed a priori. Thus, the modified DE quadrature can replace the GL as well as the original DE rules used for the computation of the observation integrals (7.3).

7.4 Conclusion

In the present work, the efficient integration of the reaction integrals has been considered. Specifically, attention was given to the integration of the observation integral, since the lack of dedicated numerical algorithms combined with the unbounded derivatives of the source integral lead to poor numerical results. In order to overcome this issue, 2-D quadratures based on the DE rules have been initially developed for rectangular domains and now extended for triangular ones. It is now possible to obtain exact numerical results for the reaction integrals. In an attempt to accelerate even more the efficiency of the proposed method, a modification in the DE quadrature rule is introduced resulting in enhanced performance in the computation of the observation domain of these weakly singular integrals. The new rule clearly outperforms its counterparts, the original DE and the GL rules. Indeed, for a small number of evaluation points of such integrals, the proposed modified DE rule beats clearly the GL rule, which was regarded as the most efficient until now, while for a large number of sampling points the excellent behavior of the DE rule is maintained. Thus, the modified DE rule, developed in this thesis, can be safely used instead of the GL or even the original DE rule, providing improved accuracy without any additional computational effort.

8 Conclusions and Future Work

8.1 Thesis assessment

Planar stratified media serve as the basic structure for a plethora of RF, microwave and recently THz components. One of the most suitable and efficient numerical methods for their EM analysis is the Integral Equation method combined with the Method of Moments discretization technique. Among the different Integral Equation formulations, Mixed Potential Integral Equations (MPIE) serve as one of the most competitive due to the lower order singularities that appear in the kernels of the integrals.

The target of this thesis was to provide a general framework for developing the appropriate Green Functions (GFs) for each multilayered structure. Although this is a classical CEM problem where many researchers have already faced most of the difficulties, new designs that include very thin conductive sheets have to be accommodated. Recent technological advances in the area of thin conductive sheets, like the fabrication of the one atom thick graphene, have provided a platform for new EM devices, especially in the area of THz. Properties like plasmon propagation at the THz range or field amplification enhance the scientific interest.

The extremely small thickness, up to molecular scale for the case of graphene, deteriorates the performance of the current methods. For this reason, a general method based on the propagator matrix technique, enhanced so as to include the conductive sheets, is provided in Chapter 4. Even arbitrary tensorial conductivity, a very challenging situation that comes under the simultaneous electric and magnetic bias of graphene, can be taken into account with this approach. GFs in the spectral domain for the EM fields and the scalar and vector potentials have been obtained for cases with high scientific and technological interest. The validity of the results, especially the position of the TM and TE poles, that can be derived with alternative techniques, has been verified for the cases a literature reference exists. Finally, the spectral domain mixed potential GFs serve as the first necessary step in order to employ the efficient MPIE method in such problems.

The spatial domain counterparts of these GFs have to be calculated efficiently and in an error-controllable manner through the Sommerfeld integrals. Novel techniques based on specialized Double Exponential (DE) quadrature rules and the Weighted Averages (WA) algorithm have been presented in Chapter 6. The DE rule has been revisited in order to account for adaptivity and efficient error estimation as discussed in Chapters 5 and 6. The algorithm outperforms in terms of speed the reference method, that is the detour of the integration path of the Sommerfeld integral. It manages to provide accurate results up to the predefined accuracy level. If average accuracy is enough for certain applications, a very fast result can be provided, while at the cost of relatively increased computational resources, even numerically exact results can be available. It should always be mentioned that the proposed method does not require a detour of the integration path into the complex plane to recover the real axis only after all the singularities have been bypassed. This is a very important property for devices which support plasmon modes, as the position of the surface plasmon pole is not bounded.

Finally, a novel optimized technique, based also on the DE quadrature rule, for the numerical evaluation of the reaction integrals of the MoM matrix was presented in Chapter 7. It manages to evaluate even at machine precision levels, if required, the integration over the observation patch. It performs satisfactory well even for distorted triangular domains, or for observation domains that are arbitrarily close to the source domains.

Combining all the contributions together, a framework that allows the efficient and very accurate numerical modeling of multilayered structures with conductive sheets has been developed. Upon expanding the sources on a certain set of basis functions and inverting the MoM matrix, the EM fields everywhere inside the multilayered structure become available.

8.2 Perspectives

As already said, in order to build a complete EM solver dedicated to multilayered structures with conductive sheets, a discretization of the sources and the solution of the MoM equations are required. Both steps are included in all the IE-MoMs implementations and they are not going to be influenced by the peculiarities of the conductive sheets as they have already been absorbed within the spatial domain GFs and the evaluation of the reaction integrals. However, a complete EM solver will be able to provide EM fields inside multilayered structures excited by real life sources and not only δ excitations or plane waves. This will allow the more sophisticated design of modern microwave and THz devices.

Throughout the chapters of this thesis, there are several obvious issues that need to be addressed further or improved. One of the most important is the efficient location of the surface plasmon pole, required in Chapter 6. It is not any more bounded as it used to be in the classical multilayered structures, and consequently the pole extraction algorithms already developed have to be revisited.

In Chapter 7, Cartesian products were used in order to build the 2-D DE quadrature rule over triangular domains. It is known that the Cartesian products for triangles are suboptimal in the sense that an alternative distribution of integration points may result in the same accuracy with fewer function evaluations. Consequently, a 2-D rule exclusively developed for integration over triangles should be built. Such an idea, developed for Gauss Legendre quadrature rules, can be found in [154].

The DE rule presented in Chapter 7 is expected to perform equally well even in cases where the integrand is not strictly weakly singular. This can open the door for its utilization not only in the MPIE methods but also in other IEs like EFIE with higher order singularities. Premise for this is the development of an efficient and accurate technique for the integration of the inner integral over the source domain for arbitrary positions of the observation point. There exist already some successful ideas to begin with [157].

Bibliography

[1] K. F. Lee and K. M. Luk, *Microstrip patch antennas.* World Scientific, 2010.

[2] J. R. Mosig, R. C. Hall, and F. E. Gardiol, *Numerical analysis of microstrip patch antennas.* in Handbook of Microstrip Antennas, James and Hall, Eds. London: IEE-Peter Peregrinus, 1989.

[3] S. Vaccaro, J. R. Mosig, and P. de Maagt, “Two advanced solar antenna ”solant” designs for satellite and terrestrial communications,” *Antennas and Propagation, IEEE Transactions on*, vol. 51, no. 8, pp. 2028–2034, 2003.

[4] K. S. Novoselov, A. K. Geim, S. V. Morozov, D. Jiang, Y. Zhang, S. V. Dubonos, I. V. Grigorieva, and A. A. Firsov, “Electric field effect in atomically thin carbon films,” *Science*, vol. 306, no. 5696, pp. 666–669, 2004.

[5] A. Vakil and N. Engheta, “Transformation optics using graphene,” *Science*, vol. 332, no. 6035, pp. 1291–1294, 2011.

[6] L. Novotny and B. Hecht, *Principles of nano-optics.* Cambridge university press, 2012.

[7] Y. Shao, J. Wang, H. Wu, J. Liu, I. A. Aksay, and Y. Lin, “Graphene based electrochemical sensors and biosensors: a review,” *Electroanalysis*, vol. 22, no. 10, pp. 1027–1036, 2010.

[8] J. Wu, H. A. Becerril, Z. Bao, Z. Liu, Y. Chen, and P. Peumans, “Organic solar cells with solution-processed graphene transparent electrodes,” *Applied Physics Letters*, vol. 92, no. 26, 2008.

[9] J. R. Miller, R. A. Outlaw, and B. C. Holloway, “Graphene double-layer capacitor with ac line-filtering performance,” *Science*, vol. 329, no. 5999, pp. 1637–1639, 2010.

[10] M. Tamagnone, J. S. Gómez-Díaz, J. R. Mosig, and J. Perruisseau-Carrier, “Reconfigurable THz Plasmonic Antenna Concept Using a Graphene Stack,” *Applied Physics Letters*, vol. 101, p. 214102, 2012.

[11] E. Carrasco, M. Tamagnone, and J. Perruisseau-Carrier, “Tunable graphene reflective cells for THz reflectarrays and generalized law of reflection,” *Applied Physics Letters*, vol. 102, no. 10, 2013.

[12] G. Mur, “A finite difference method for the solution of electromagnetic waveguide discontinuity problems,” *Microwave Theory and Techniques, IEEE Transactions on*, vol. 22, no. 1, pp. 54–57, 1974.

[13] R. Luebbers, F. Hunsberger, K. S. Kunz, R. Standler, and M. Schneider, "A frequency-dependent finite-difference time-domain formulation for dispersive materials," *Electromagnetic Compatibility, IEEE Transactions on*, vol. 32, no. 3, pp. 222–227, 1990.

[14] Y. Hao and R. Mittra, *FDTD modeling of metamaterials.* Artech house, 2009.

[15] D. M. Sullivan, *Electromagnetic simulation using the FDTD method.* Wiley-IEEE Press, 2013.

[16] S. E. Krakiwsky, L. E. Turner, and M. M. Okoniewski, "Acceleration of finite-difference time-domain (FDTD) using graphics processor units (GPU)," in *Microwave Symposium Digest, 2004 IEEE MTT-S International*, vol. 2. IEEE, 2004, pp. 1033–1036.

[17] D. S. Katz, E. T. Thiele, and A. Taflove, "Validation and extension to three dimensions of the berenger pml absorbing boundary condition for fd-td meshes," *Microwave and Guided Wave Letters, IEEE*, vol. 4, no. 8, pp. 268–270, 1994.

[18] G. D. Smith, *Numerical solution of partial differential equations: finite difference methods.* Oxford University Press, 1985.

[19] Y. Hao and C. J. Railton, "Analyzing electromagnetic structures with curved boundaries on cartesian fdtd meshes," *Microwave Theory and Techniques, IEEE Transactions on*, vol. 46, no. 1, pp. 82–88, 1998.

[20] R. Courant, "Variational methods for the solution of problems of equilibrium and vibrations," *Bull. Amer. Math. Soc*, vol. 49, no. 1, p. 23, 1943.

[21] R. Coccioli, T. Itoh, G. Pelosi, and P. Silvester, "Finite-element methods in microwaves: a selected bibliography," *Antennas and Propagation Magazine, IEEE*, vol. 38, no. 6, pp. 34–48, 1996.

[22] J.-M. Jin, *The Finite Element Method in Electromagnetics.* Wiley-Interscience, 2002.

[23] W. B. Zimmerman, "Multiphysics modeling with finite element methods," *Series On Stability, Vibration And Control Of Systems*, 2006.

[24] D. Arnold, F. Brezzi, B. Cockburn, and L. Marini, "Unified analysis of discontinuous galerkin methods for elliptic problems," *SIAM Journal on Numerical Analysis*, vol. 39, no. 5, pp. 1749–1779, 2002.

[25] S.-C. Lee, M. N. Vouvakis, and J.-F. Lee, "A non-overlapping domain decomposition method with non-matching grids for modeling large finite antenna arrays," *Journal of Computational Physics*, vol. 203, no. 1, pp. 1–21, 2005.

[26] A. Quarteroni, *Numerical Models for Differential Problems.* Springer-Verlag, 2009.

[27] G. B. Arfken, H.-J. Weber, and L. Ruby, *Mathematical methods for physicists.* Academic press New York, 1985, vol. 6.

[28] R. F. Harrington, *Field computation by moment methods.* New York: Macmillan, FL, Krieger, 1983.

[29] J. A. Kong, “Theory of electromagnetic waves,” *New York, Wiley-Interscience*, 1975.

[30] J. R. Mosig, “Integral equation techniques for three-dimensional microstrip structures,” *Review of Radio Science*, vol. 1992, pp. 127–152, 1990.

[31] W. C. Chew, *Waves and fields in inhomogenous media.* IEEE press New York, 1995.

[32] D. B. Davidson, *Computational electromagnetics for RF and microwave engineering.* Cambridge University Press, 2005.

[33] J. R. Mautz, “H-field, e-field, and combined-field solutions for conducting bodies of revolution,” *Arch. Elekron. Ubertragungstech (AEU)*, vol. 32, no. 4, pp. 157–164, 1978.

[34] A. J. Poggio and E. K. Miller, “Integral equation solutions of three-dimensional scattering problems,” *Computer techniques for electromagnetics. Oxford and New York, Pergamon Press, 1973,*, pp. 159–264, 1973.

[35] A. D. Yaghjian, “Augmented electric-and magnetic-field integral equations,” *Radio Science*, vol. 16, no. 6, pp. 987–1001, 1981.

[36] A. Glisson and D. Wilton, “Simple and efficient numerical methods for problems of electromagnetic radiation and scattering from surfaces,” *Antennas and Propagation, IEEE Transactions on*, vol. 28, no. 5, pp. 593–603, 1980.

[37] J. R. Mosig, “Arbitrarily shaped microstrip structures and their analysis with a mixed potential integral equation,” *Microwave Theory and Techniques, IEEE Transactions on*, vol. 36, no. 2, pp. 314–323, 1988.

[38] K. Michalski and D. Zheng, “Electromagnetic scattering and radiation by surfaces of arbitrary shape in layered media. i. theory,” *Antennas and Propagation, IEEE Transactions on*, vol. 38, no. 3, pp. 335–344, 1990.

[39] R. Coifman, V. Rokhlin, and S. Wandzura, “The fast multipole method for the wave equation: A pedestrian prescription,” *Antennas and Propagation Magazine, IEEE*, vol. 35, no. 3, pp. 7–12, 1993.

[40] J. Song and W. C. Chew, “Multilevel fast-multipole algorithm for solving combined field integral equations of electromagnetic scattering,” *Microwave and Optical Technology Letters*, vol. 10, no. 1, pp. 14–19, 1995.

[41] J. Song, C.-C. Lu, and W. C. Chew, “Multilevel fast multipole algorithm for electromagnetic scattering by large complex objects,” *Antennas and Propagation, IEEE Transactions on*, vol. 45, no. 10, pp. 1488–1493, 1997.

[42] E. Bleszynski, M. Bleszynski, and T. Jaroszewicz, "AIM: Adaptive integral method for solving large-scale electromagnetic scattering and radiation problems," *Radio Science*, vol. 31, no. 5, pp. 1225–1251, 1996.

[43] J. Phillips and J. White, "A precorrected-fft method for electrostatic analysis of complicated 3-d structures," *Computer-Aided Design of Integrated Circuits and Systems, IEEE Transactions on*, vol. 16, no. 10, pp. 1059–1072, 1997.

[44] S. Tissari and J. Rahola, "A precorrected-fft method to accelerate the solution of the forward problem in magnetoencephalography," *Physics in Medicine and Biology*, vol. 48, no. 4, p. 523, 2003.

[45] J. Markkanen, P. Yla-Oijala, and A. Sihvola, "Discretization of volume integral equation formulations for extremely anisotropic materials," *Antennas and Propagation, IEEE Transactions on*, vol. 60, no. 11, pp. 5195–5202, 2012.

[46] A. G. Polimeridis, J. F. Villena, L. Daniel, and J. K. White, "Stable FFT-JVIE solvers for fast analysis of highly inhomogeneous dielectric objects," *Journal of Computational Physics*, under review.

[47] L. Matekovits, G. Vecchi, G. Dassano, and M. Orefice, "Synthetic function analysis of large printed structures: the solution space sampling approach," in *Antennas and Propagation Society International Symposium, 2001. IEEE*, vol. 2. IEEE, 2001, pp. 568–571.

[48] J. Yeo, V. Prakash, and R. Mittra, "Efficient analysis of a class of microstrip antennas using the characteristic basis function method (CBFM)," *Microwave and Optical Technology Letters*, vol. 39, no. 6, pp. 456–464, 2003.

[49] I. Stevanović and J. R. Mosig, "Efficient evaluation of macro-basis-function reaction terms in the subdomain multilevel approach," *Microwave and Optical Technology Letters*, vol. 42, no. 2, pp. 138–143, 2004.

[50] F. Schwierz, "Graphene transistors," *Nature nanotechnology*, vol. 5, no. 7, pp. 487–496, 2010.

[51] F. Bonaccorso, Z. Sun, T. Hasan, and A. Ferrari, "Graphene photonics and optoelectronics," *Nature Photonics*, vol. 4, no. 9, pp. 611–622, 2010.

[52] P. Tassin, T. Koschny, and C. M. Soukoulis, "Graphene for terahertz applications," *Science*, vol. 341, no. 6146, pp. 620–621, 2013.

[53] "Graphene is not alone," *Nature Nanotechnology*, vol. 7, no. 11, pp. 683–683, 2012.

[54] S. Schelkunoff, "Conversion of Maxwell's equations into generalized telegraphist's equations," *Bell Syst. Tech. J*, vol. 34, no. 5, pp. 995–1043, 1955.

[55] W. J. R. Hoefer, "The transmission-line matrix method–theory and applications," *Microwave Theory and Techniques, IEEE Transactions on*, vol. 33, no. 10, pp. 882–893, 1985.

[56] K. A. Michalski and J. R. Mosig, "Multilayered media Green's functions in integral equation formulations," *Antennas and Propagation, IEEE Transactions on*, vol. 45, no. 3, pp. 508 –519, Mar. 1997.

[57] S.-G. Pan and I. Wolff, "Scalarization of dyadic spectral green's functions and network formalism for three-dimensional full-wave analysis of planar lines and antennas," *Microwave Theory and Techniques, IEEE Transactions on*, vol. 42, no. 11, pp. 2118–2127, 1994.

[58] P. Crespo-Valero, M. Mattes, I. Stevanović, and J. R. Mosig, "A numerically stable transmission line model for multilayered green's functions," in *Antennas and Propagation Society International Symposium, 2005 IEEE*, vol. 3A, 2005, pp. 200–203 vol. 3A.

[59] M. Guglielmi and D. Jackson, "Low-frequency location of the leaky-wave poles for a dielectric layer," *Microwave Theory and Techniques, IEEE Transactions on*, vol. 38, no. 11, pp. 1743–1746, 1990.

[60] J. Gomez Tornero and A. Álvarez Melcón, "Leaky and surface waves in multilayered laterally-shielded microstrip transmission lines," *Microwave and Optical Technology Letters*, vol. 37, no. 2, pp. 88–93, 2003.

[61] M. Jablan, H. Buljan, and M. Soljačić, "Plasmonics in graphene at infrared frequencies," *Physical review B*, vol. 80, no. 24, p. 245435, 2009.

[62] G. Lovat, "Equivalent circuit for electromagnetic interaction and transmission through graphene sheets," *Electromagnetic Compatibility, IEEE Transactions on*, vol. 54, no. 1, pp. 101–109, 2012.

[63] G. Lovat, P. Burghignoli, and R. Araneo, "Low-frequency dominant-mode propagation in spatially dispersive graphene nanowaveguides," *Electromagnetic Compatibility, IEEE Transactions on*, vol. 55, no. 2, pp. 328–333, 2013.

[64] A. Fallahi and J. Perruisseau-Carrier, "Design of tunable biperiodic graphene metasurfaces," *Phys. Rev. B*, vol. 86, p. 195408, Nov 2012.

[65] A. Sommerfeld, *Partial Differential Equations in Physics.* Academic Press, 1949.

[66] Y. L. Chow, J. Yang, D. Fang, and G. Howard, "A closed-form spatial green's function for the thick microstrip substrate," *Microwave Theory and Techniques, IEEE Transactions on*, vol. 39, no. 3, pp. 588–592, 1991.

[67] G. Dural and M. I. Aksun, "Closed-form Green's functions for general sources and stratified media," *Microwave Theory and Techniques, IEEE Transactions on*, vol. 43, no. 7, pp. 1545–1552, 1995.

[68] K. A. Michalski and J. R. Mosig, “Discrete complex image mixed-potential integral equation analysis of microstrip patch antennas with vertical probe feeds,” *Electromagnetics*, vol. 15, no. 4, pp. 377–392, 1995.

[69] N. Kinayman and M. I. Aksun, “Efficient use of closed-form Green’s functions for the analysis of planar geometries with vertical connections,” *Microwave Theory and Techniques, IEEE Transactions on*, vol. 45, no. 5, pp. 593–603, 1997.

[70] Y. P. Chen, W. C. Chew, and L. Jiang, “A novel implementation of discrete complex image method for layered medium green’s function,” *Antennas and Wireless Propagation Letters, IEEE*, vol. 10, pp. 419–422, 2011.

[71] A. Alparslan, M. I. Aksun, and K. A. Michalski, “Closed-Form Green’s Functions in Planar Layered Media for All Ranges and Materials,” *Microwave Theory and Techniques, IEEE Transactions on*, vol. 58, no. 3, pp. 602 –613, Mar. 2010.

[72] E. Karabulut, A. T. Erdogan, and M. Aksun, “Discrete complex image method with spatial error criterion,” *Microwave Theory and Techniques, IEEE Transactions on*, vol. 59, no. 4, pp. 793–802, 2011.

[73] J. R. Mosig and F. E. Gardiol, “Analytical and numerical techniques in the Green’s function treatment of microstrip antennas and scatterers,” in *IEE Proceedings H (Microwaves, Optics and Antennas)*, vol. 130, no. 2. IET, 1983, pp. 175–182.

[74] J. R. Mosig and T. K. Sarkar, “Comparison of quasi-static and exact electromagnetic fields from a horizontal electric dipole above a lossy dielectric backed by an imperfect ground plane,” *Microwave Theory and Techniques, IEEE Transactions on*, vol. 34, no. 4, pp. 379–387, 1986.

[75] P. Gay-Balmaz and J. R. Mosig, “Three-dimensional planar radiating structures in stratified media,” *International Journal of Microwave and Millimeter-Wave Computer-Aided Engineering*, vol. 7, no. 5, pp. 330–343, 1997.

[76] J. R. Mosig and A. Álvarez-Melcón, “Green’s functions in lossy layered media: Integration along the imaginary axis and asymptotic behavior,” *Antennas and Propagation, IEEE Transactions on*, vol. 51, no. 12, pp. 3200–3208, 2003.

[77] A. G. Polimeridis, T. V. Yioultsis, and T. D. Tsiboukis, “An Efficient Pole Extraction Technique for the Computation of Green’s Functions in Stratified Media Using a Sine Transformation,” *Antennas and Propagation, IEEE Transactions on*, vol. 55, no. 1, pp. 227 –229, Jan. 2007.

[78] J. R. Mosig, “The weighted averages algorithm revisited,” *Antennas and Propagation, IEEE Transactions on*, vol. 60, no. 4, pp. 2011 –2018, Apr. 2012.

[79] R. Golubović-Nićiforović, A. G. Polimeridis, and J. R. Mosig, “Fast Computation of Sommerfeld Integral Tails via Direct Integration Based on Double Exponential-Type

Quadrature Formulas," *Antennas and Propagation, IEEE Transactions on*, vol. 59, no. 2, pp. 694 –699, Feb. 2011.

[80] R. Golubović, A. G. Polimeridis, and J. R. Mosig, "Efficient algorithms for computing sommerfeld integral tails," *Antennas and Propagation, IEEE Transactions on*, vol. 60, no. 5, pp. 2409–2417, 2012.

[81] L. Rossi and P. J. Cullen, "On the fully numerical evaluation of the linear-shape function times the 3-D Green"s function on a plane triangle," *Microwave Theory and Techniques, IEEE Transactions on*, vol. 47, no. 4, pp. 398–402, Apr. 1999.

[82] M. A. Khayat and D. R. Wilton, "Numerical evaluation of singular and near-singular potential integrals," *Antennas and Propagation, IEEE Transactions on*, vol. 53, no. 10, pp. 3180–3190, Oct. 2005.

[83] M. A. Khayat, D. R. Wilton, and P. W. Fink, "An improved transformation and optimized sampling scheme for the numerical evaluation of singular and near-sigular potentials," *IEEE Antennas Wireless Propag. Lett.*, vol. 7, pp. 377–380, 2008.

[84] P. W. Fink, D. R. Wilton, and M. A. Khayat, "Simple and efficient numerical evaluation of near-hypersingular integrals," *IEEE Antennas Wireless Propag. Lett.*, vol. 7, pp. 469–472, 2008.

[85] R. D. Graglia and G. Lombardi, "Machine precision evaluation of singular and nearly singular potential integrals by use of Gauss quadrature formulas for rational functions," *Antennas and Propagation, IEEE Transactions on*, vol. 56, no. 4, pp. 981–998, Apr. 2008.

[86] D. R. Wilton, S. M. Rao, A. W. Glisson, D. H. Schaubert, O. M. AL-Bundak, and C. M. Butler, "Potential integrals for uniform and linear source distributions on polygonal and polyhedral domains," *Antennas and Propagation, IEEE Transactions on*, vol. 32, no. 3, pp. 276–281, Mar. 1984.

[87] R. D. Graglia, "On the numerical integration of the linear shape functions times the 3-D Green's function or its gradient on a plane triangle," *Antennas and Propagation, IEEE Transactions on*, vol. 41, no. 10, pp. 1448–1455, Oct. 1993.

[88] T. F. Eibert and V. Hansen, "On the calculation of potential integrals for linear source distributions on triangular domains," *Antennas and Propagation, IEEE Transactions on*, vol. 43, no. 12, pp. 1499–1502, Dec. 1995.

[89] P. Arcioni, M. Bressan, and L. Perregrini, "On the evaluation of the double surface integrals arising in the application of the boundary integral method to 3-D problems," *Microwave Theory and Techniques, IEEE Transactions on*, vol. 45, no. 3, pp. 436–439, Mar. 1997.

[90] I. Ismatullah and T. F. Eibert, "Adaptive singularity cancellation for efficient treatment of near-singular and near-hypersingular integrals in surface integral equation formulations," *Antennas and Propagation, IEEE Transactions on*, vol. 56, no. 1, pp. 274–278, Jan. 2008.

[91] S. López-Peña and J. R. Mosig, "Analytical evaluation of the quadruple static potential integrals on rectangular domains to solve 3-D electromagnetic problems," *IEEE Trans. Magn.*, vol. 54, no. 3, pp. 1320–1323, Mar. 2009.

[92] A. G. Polimeridis and T. V. Yioultsis, "On the direct evaluation of weakly singular integrals in Galerkin mixed potential integral equation formulations," *Antennas and Propagation, IEEE Transactions on*, vol. 56, no. 9, pp. 3011–3019, Jul. 2008.

[93] A. G. Polimeridis and J. R. Mosig, "Complete semi-analytical treatment of weakly singular integrals on planar triangles via the direct evaluation method," *International journal for numerical methods in engineering*, vol. 83, no. 12, pp. 1625–1650, 2010.

[94] R. Harrington, *Time-Harmonic Electromagnetic Fields.* McGraw-Hill, New York, 1961.

[95] J. D. Jackson, *Classical Electrodynamics*, 3rd ed. John Wiley & Sons: New York, 1998.

[96] L. Lorenz, "On the identity of the vibrations of light with electrical currents," *The London, Edinburgh, and Dublin Philosophical Magazine and Journal of Science*, vol. 34, no. 230, pp. 287–301, 1867.

[97] S. M. Rao, D. R. Wilton, and A. W. Glisson, "Electromagnetic scattering by surfaces of arbitrary shape," *Antennas and Propagation, IEEE Transactions on*, vol. 30, no. 5, pp. 409–418, May 1982.

[98] L. B. Felsen and N. Marcuvitz, *Radiation and scattering of waves.* IEEE Press, 1994.

[99] J. S. Gómez-Díaz and J. Perruisseau-Carrier, "Propagation of hybrid transverse magnetic-transverse electric plasmons on magnetically biased graphene sheets," *Journal of Applied Physics*, vol. 112, no. 12, pp. 124 906–124 906, 2012.

[100] G. W. Hanson, "Dyadic Green's functions and guided surface waves for a surface conductivity model of graphene," *Journal of Applied Physics*, vol. 103, no. 6, 2008.

[101] A. Nikitin, F. Garcia-Vidal, and L. Martin-Moreno, "Analytical expressions for the electromagnetic dyadic green's function in graphene and thin layers," *Selected Topics in Quantum Electronics, IEEE Journal of*, vol. PP, no. 99, p. 1, 2012.

[102] E. Anemogiannis and E. N. Glytsis, "Multilayer waveguides: efficient numerical analysis of general structures," *Lightwave Technology, Journal of*, vol. 10, no. 10, pp. 1344–1351, 1992.

[103] A. Álvarez-Melcón, "Application of the integral equation technique to the analysis and synthesis of multilayered printed shielded microwave circuits and cavity backed antennas," Ph.D. dissertation, École Polytechnique Fédérale de Lausanne, Switzerland, Thèse No 1901, 1998.

[104] T. Grzegorczyk, "Integrated 3D antennas for millimeter-wave applications: Theoretical study and technological reallzatlon," Ph.D. dissertation, École Polytechnique Fédérale de Lausanne, Switzerland, Thèse No 2299, 2000.

[105] M. Abramowitz and I. Stegun, *Handbook of Mathematical Functions.* Dover Publications, 1965.

[106] I. S. Gradshteyn and I. M. Ryzhik, *Table of Integrals, Series, and Products*, 7th ed., A. Jeffrey and D. Zwillinger, Eds. Elsevier, 2007.

[107] P. Gay-Balmaz, "Structures 3-d planaires en milieux stratifiés: fonctions de green et application à des antennes incluant des parois verticales," Ph.D. dissertation, École Polytechnique Fédérale de Lausanne, Switzerland, Thèse No 1569, 1996.

[108] A. Cottey, "The electrical conductivity of thin metal films with very smooth surfaces," *Thin Solid Films*, vol. 1, no. 4, pp. 297 – 307, 1968.

[109] K. Fuchs, "The conductivity of thin metallic films according to the electron theory of metals," *Math. Proc. Cambridge Philos. Soc.*, vol. 34, pp. 100–108, 1938.

[110] E. H. Sondheimer, "The mean free path of electrons in metals," *Advances in Physics*, vol. 1, pp. 1–42, 1952.

[111] L. A. Falkovsky, "Optical properties of graphene," *Journal of Physics: Conference Series*, vol. 129, no. 1, p. 012004, 2008.

[112] I. D. Koufogiannis, M. Mattes and J. R. Mosig, "Mixed potentials for planar multilayered structures including conductive interfaces," in *Antennas and Propagation (EuCAP), 2014 8th European Conference on*, Accepted, pp. 1–3.

[113] F. H. L. Koppens, D. E. Chang, and F. J. Garcia de Abajo, "Graphene plasmonics: A platform for strong light-matter interactions," *Nano Letters*, vol. 11, no. 8, pp. 3370–3377, 2011.

[114] G. W. Hanson, E. Forati, W. Linz, and A. B. Yakovlev, "Excitation of terahertz surface plasmons on graphene surfaces by an elementary dipole and quantum emitter: Strong electrodynamic effect of dielectric support," *Phys. Rev. B*, vol. 86, p. 235440, Dec 2012.

[115] R. E. Collin, *Field theory of guided waves*, ser. IEEE/OUP series on electromagnetic wave theory. New York: IEEE Press, 1991.

[116] S. Vaccaro, P. Torres, J. R. Mosig, A. Shah, J.-F. Zürcher, A. Skrivervik, F. Gardiol, P. de Maagt, and L. Gerlach, "Integrated solar panel antennas," *Electronics Letters*, vol. 36, no. 5, pp. 390–391, 2000.

[117] M. Esquius-Morote, J. S. Gómez-Díaz, and J. Perruisseau-Carrier, "Sinusoidally-modulated graphene leaky-wave antenna for electronic beamscanning at THz," *Terahertz Science and Technology, IEEE Transactions on*, vol. 4, no. 1, pp. 116–122, Jan 2014.

[118] G. W. Hanson, "Quasi-transverse electromagnetic modes supported by a graphene parallel-plate waveguide," *Journal of Applied Physics*, vol. 104, no. 8, 2008.

[119] A. Malekabadi, S. A. Charlebois, and D. Deslandes, "Parallel plate waveguide with anisotropic graphene plates: Effect of electric and magnetic biases," *Journal of Applied Physics*, vol. 113, no. 11, 2013.

[120] J. S. Gómez-Díaz, J. R. Mosig, and J. Perruisseau-Carrier, "Effect of spatial dispersion on surface waves propagating along graphene sheets," *Antennas and Propagation, IEEE Transactions on*, vol. 61, no. 7, pp. 3589–3596, July 2013.

[121] D. Correas-Serrano, J. S. Gómez-Díaz, J. Perruisseau-Carrier, and A. Álvarez-Melcón, "Spatially dispersive graphene single and parallel plate waveguides: Analysis and circuit model," *Microwave Theory and Techniques, IEEE Transactions on*, vol. 61, no. 12, pp. 4333–4344, 2013.

[122] H. Takahasi and M. Mori, "Double Exponential formulas for numerical integration," *Publ. RIMS, Kyoto Univ.*, no. 9, pp. 721–741, 1974.

[123] P. J. Davis and P. Rabinowitz, *Methods of numerical integration.* Academic Press New York, 1975, vol. 1.

[124] J. Stoer and R. Bulirsch, *Introduction to numerical analysis*, 3rd ed. Springer, 2002, vol. 12.

[125] D. Kahaner, C. Moler, and S. Nash, *Numerical Methods and Software*, 1989.

[126] H. Takahasi and M. Mori, "Error estimation in the numerical integration of analytic functions," *Report Computer Centre University of Tokyo*, no. 3, pp. 41–108, 1970.

[127] M. Mori, "The discovery of the Double Exponential transformation and its developments," *Publ. RIMS, Kyoto Univ.*, no. 41, pp. 897–935, 2005.

[128] A. R. Krommer and C. W. Ueberhuber, *Computational integration.* SIAM, 1998.

[129] D. H. Bailey, K. Jeyabalan, and X. S. Li, "A comparison of three high-precision quadrature schemes," *Experimental Mathematics*, vol. 3, no. 14, pp. 317–329, 2005.

[130] A. G. Polimeridis and J. R. Mosig, "Evaluation of weakly singular integrals via generalized Cartesian product rules based on the double exponential formula," *Antennas and Propagation, IEEE Transactions on*, vol. 58, no. 6, pp. 3011–3019, Jun. 2010.

[131] I. D. Koufogiannis, A. G. Polimeridis, M. Mattes, and J. R. Mosig, “Real axis integration of sommerfeld integrals with error estimation,” in *Antennas and Propagation (EUCAP), 2012 6th European Conference on*, Mar. 2012, pp. 719 –723.

[132] J. Waldvogel, “Towards a general error theory of the trapezoidal rule,” in *Approximation and Computation*, ser. Springer Optimization and Its Applications, W. Gautschi, G. Mastroianni, and T. M. Rassias, Eds. Springer New York, 2011, vol. 42, pp. 267–282.

[133] T. Ooura and M. Mori, “The Double Exponential formula for oscillatory functions over the half infinite interval,” *Journal of Computational and Applied Mathematics*, vol. 38, pp. 353–360, 1991.

[134] M. Muhammad and M. Mori, “Double exponential formulas for numerical indefinite integration,” *Journal of Computational and Applied Mathematics*, vol. 161, pp. 431–448, 2003.

[135] F. Andriulli, A. Tabacco, and G. Vecchi, “A multiresolution approach to the Electric Field Integral Equation in antenna problems,” *SIAM Journal on Scientific Computing*, vol. 29, no. 1, pp. 1–21, 2007.

[136] F. Demuynck, G. Vandenbosch, and A. Van de Capelle, “The expansion wave concept. I. Efficient calculation of spatial green’s functions in a stratified dielectric medium,” *Antennas and Propagation, IEEE Transactions on*, vol. 46, no. 3, pp. 397–406, 1998.

[137] A. K. Abdelmageed and A. A. K. Mohsen, “An accurate computation of Green’s functions for multilayered media in the near-field region,” *Microwave and Optical Technology Letters*, vol. 29, no. 2, pp. 130–131, 2001.

[138] I. D. Koufogiannis, A. G. Polimeridis, M. Mattes, and J. R. Mosig, “A parametric study of the Double Exponential algorithm utilized in weakly singular integrals,” in *Antennas and Propagation (EUCAP), Proceedings of the 5th European Conference on*, Apr. 2011, pp. 2147 –2151.

[139] K. A. Michalski, “Extrapolation methods for Sommerfeld integral tails,” *Antennas and Propagation, IEEE Transactions on*, vol. 46, no. 10, pp. 1405 –1418, Oct. 1998.

[140] H. Ogata and M. Sugihara, “Quadrature formulae for oscilaltory infinite integrals involving the Bessel functions (in japanese),” *Trans. Japan Soc. Ind. Appl. Math.*, vol. 8, no. 2, pp. 223–256, 1998.

[141] K. A. Michalski, “Application of the complex image method to electromagnetic field computation in planar uniaxial multilayers,” in *Workshop in Integral Techniques for Electromagnetics (INTELECT)*, Lausanne, Switzerland 2007.

[142] D. H. Bailey and J. M. Borwein, “Effective Error Bounds in Euler-Maclaurin-Based Quadrature Schemes,” in *Proc. Conference on High-Performance Computing Systems, IEEE Computer Society*, 2006.

[143] L. F. Shampine, “Vectorized adaptive quadrature in Matlab,” *Journal of Computational and Applied Mathematics*, vol. 211, Feb. 2008.

[144] N. Shuley, R. Boix, F. Medina, and M. Horno, “On the fast approximation of Green’s functions in MPIE formulations for planar layered media,” *Microwave Theory and Techniques, IEEE Transactions on*, vol. 50, no. 9, pp. 2185–2192, 2002.

[145] M. Aksun, “A robust approach for the derivation of closed-form green’s functions,” *Microwave Theory and Techniques, IEEE Transactions on*, vol. 44, no. 5, pp. 651–658, 1996.

[146] A. Y. Nikitin, F. Guinea, F. J. Garcia-Vidal, and L. Martin-Moreno, “Fields radiated by a nanoemitter in a graphene sheet,” *Phys. Rev. B*, vol. 84, p. 195446, Nov 2011.

[147] J. N. Chen, M. Badioli, P. Alonso-Gonzalez, S. Thongrattanasiri, F. Huth, J. Osmond, M. Spasenovic, A. Centeno, A. Pesquera, P. Godignon, A. Z. Elorza, N. Camara, F. J. G. de Abajo, R. Hillenbrand, and F. H. L. Koppens, “Optical nano-imaging of gate-tunable graphene plasmons,” *Nature*, 2012.

[148] I. D. Koufogiannis, A. G. Polimeridis, J. S. Gómez-Díaz, M. Mattes, and J. R. Mosig, “Dyadic Green’s functions of a graphene layer and their efficient calculation,” in *Antennas and Propagation Society International Symposium (APSURSI), 2013 IEEE*, 2013, pp. 1–4.

[149] A. G. Polimeridis, I. D. Koufogiannis, M. Mattes and J. R. Mosig, “Considerations on Double Exponential-based cubatures for the computation of weakly singular galerkin inner products,” *Antennas and Propagation, IEEE Transactions on*, vol. 60, no. 5, pp. 2579–2582, 2012.

[150] P. Yla-Oijala and M. Taskinen, “Calculation of CFIE impedance matrix elements with RWG and nxRWG functions,” *Antennas and Propagation, IEEE Transactions on*, vol. 51, no. 8, pp. 1837 – 1846, Aug. 2003.

[151] M. G. Duffy, “Quadrature over a pyramid or cube of integrands with a singularity at a vertex,” *SIAM. J. Numer. Anal.*, vol. 19, no. 6, pp. 1260–1262, 1982.

[152] S. Jarvenpaa, M. Taskinen, and P. Yla-Oijala, “Singularity subtraction technique for high-order polynomial vector basis functions on planar triangles,” *Antennas and Propagation, IEEE Transactions on*, vol. 54, no. 1, pp. 42–49, Jan 2006.

[153] J.-F. Zürcher, R. Glogowski, and J. R. Mosig, “A new power divider architecture for suspended strip line,” in *Antennas and Propagation (EUCAP), 2012 6th European Conference on*, 2012, pp. 418–422.

[154] D. Dunavant, “High degree efficient symmetrical gaussian quadrature rules for the triangle,” *International journal for numerical methods in engineering*, vol. 21, no. 6, pp. 1129–1148, 1985.

[155] V. U. Aihie and G. A. Evans, “The tanh transformation for double integrals with singularities - a progressive rule,” *J. Comput. Appl. Math.*, no. 24, pp. 349–354, 1988.

[156] ——, “A comparison of the error function and the tanh transformation as progressive rules for double and triple singular integrals,” *J. Comput. Appl. Math.*, no. 30, pp. 145–154, 1990.

[157] F. Vipiana and D. R. Wilton, “Numerical evaluation via singularity cancellation schemes of near-singular integrals involving the gradient of Helmholtz-type potentials,” *Antennas and Propagation, IEEE Transactions on*, vol. 61, no. 3, pp. 1255–1265, 2013.

List of Figures

1.1 Thesis's contents and original contributions (in red) in a nutshell. 4

4.1 Rotated coordinate system in the spectral domain. 21
4.2 General multilayered structure with dielectric layers and conductive interfaces. 25
4.3 Propagation through a dielectric layer without sources. 26
4.4 Propagation through an interface between two dielectric layers. 27
4.5 Radiation from the upper semi-infinite medium. 27
4.6 Radiation from the lower semi-infinite medium. 28
4.7 Surface impedance boundary condition on the lower layer. 29
4.8 Surface impedance boundary condition on the upper layer. 29
4.9 Dielectric layer with excitation. 30
4.10 Interface with scalar conductivity. 32
4.11 Interface with tensorial conductivity. 33
4.12 A dielectric layer with bulky conductivity σ_{3D} and thickness d_2 (a) and its limiting case of a conductive sheet with σ_{2D} when $d_2 \to 0$ (b). 35
4.13 Interface with mixed potentials 37
4.14 A conductive layer (in this case a graphene sheet) seperating two semi-infinite spaces. 41
4.15 A conductive layer (in this case a graphene sheet) separating two semi-infinite spaces. 49
4.16 Real (blue line) and imaginary (red line) part of σ of a graphene sheet at 300K, at a chemical potential of 0.2eV and of relaxation time of 1ps using Kubo formula [111]. 51
4.17 Real and imaginary part of the SPP propagating along a graphene sheet as indicated in (4.98). The graphene is set at 300^{o}K with a chemical potential of 0.2eV and a relaxation time of 1ps. The Kubo formula [111] was used for the conductivity of the graphene sheet. 51
4.18 Position of the pole of the plasmon mode on the complex plane for a graphene layer floating in the air according to (4.98). The graphene is set at 300^{o}K with a chemical potential of 0.2eV and a relaxation time of 1ps. The Kubo formula [111] was used for the conductivity of the graphene sheet. 52
4.19 G_{EJ}^{zx} for different horizontal separations ρ between the source and the observation point. The horizontal source is placed on the upper side of the graphene sheet and the field is calculated on the lower side of the sheet. The GF is calculated both directly and through the mixed potentials yielding identical results. 53

4.20 G_{EJ}^{zz} for different horizontal separations ρ between the source and the observation point. The vertical source is placed on the upper side of the graphene sheet and the field is calculated on the lower side of the sheet. The GF is calculated both directly and trough the mixed potentials yielding identical results. 54
4.21 G_V^{ρ} of floating graphene sheet for different horizontal distances ρ and frequencies. The source and observation are located on the graphene sheet but on different sides. 55
4.22 G_A^{zx} of floating graphene sheet for different horizontal distances ρ and frequencies. The source and observation are located on the graphene sheet but on different sides. 55
4.23 G_A^{zz} of floating graphene sheet for different horizontal distances ρ and frequencies. The source and observation are located on the graphene sheet but on different sides. 56
4.24 Grounded dielectric slab topped by a conductive sheet. 57
4.25 G_A^{zz} of the grounded slab of Fig. 4.24 with $\epsilon_2 = 5$ and thickness $h = \lambda$ at 1 THz topped by a sheet with a conductivity varying from 0 to very large values. Source and observation are placed on the top of the conductive sheet. 58

5.1 Plot of $f(x) = x \log x$, its first and second derivatives over the domain $x \in (0,1)$. The surface of the shaded area is 0.25, corresponding to the value of the integral of $f(x)$ over the predefined domain (5.6). 64
5.2 Gauss Legendre (GL) performance for the integration of the sample function $x \log x$. The ideal behavior of a quadrature rule is also shown for comparison purposes. 65
5.3 The function $\cos(t)$ is multiplied with a single exponentially (blue), double exponentially (red) or triple exponentially (green) decaying function. The solid lines represent the continuous functions, while the dashed line the sampled ones through the trapezoidal rule. 66
5.4 Truncation error $\mathrm{E}^{\mathrm{trunc}}$ (a) and discretization error $\mathrm{E}^{\mathrm{discr}}$ (b) for the function $\cos(t)$ of Fig. 5.3 when a single (blue), double (red) or triple (green) exponential decay is applied. The solid lines represent the continuous functions, while the dashed line the sampled ones through the trapezoidal rule as in Fig. 5.3. 67
5.5 Double Exponential or $\tanh - \sinh$ transformation and its corresponding derivative. 68
5.6 GL and DE abscissas for rules comprising 25 integration points over the reference domain $(-1,1)$ 69
5.7 Performance of GL and DE quadrature rules integrating the function $f(x) = x \log x$ for $x \in (0,1)$. 70
5.8 Original integrand (5.19) (dashed line) with singularities at the endpoints $x = \pm 1$ and transformed integrand (5.20) (continuous line) where the singularities have been moved to $t = \pm\infty$ and sufficiently decayed. The area under both curves is the same. 71
5.9 Performance of GL and DE quadrature rules integrating the function $f(x) = 1/\sqrt{1-x^2}$ for $x \in (-1,1)$. 72

5.10 Additional (stars) and already evaluated (circles) points of a DE rule if the DE rule is implemented in an adaptive way. 73

6.1 Integrand of a typical Sommerfeld integral, with the branch point and three surface waves poles visible. The common detoured path and the proposed on the axis integration path are indicated. 79
6.2 Integration path of SIs. Separation between the first part, I_n, and the tail T_n. . 80
6.3 Exact and estimated absolute error of $I_{0,a}$ (6.40) for two different thresholds of accuracy. 89
6.4 Exact and estimated absolute error of $I_{0,b}$ (6.41) for two different thresholds of accuracy. 90
6.5 Exact and estimated absolute error of $I_{1,a}$ (6.43) for two different thresholds of accuracy. 91
6.6 Computational times of the first part of the Sommerfeld integral $\mathcal{I}_0$ (6.8) for the GF of the scalar potential of an electric dipole (6.38), using GK and DE methods for different levels of accuracy. 92
6.7 Absolute error of G_A^{xx} of the proposed method for the structure of Section 6.5.2 for different levels of predefined relative error. 93
6.8 Computational times of the proposed DE and WA algorithm (solid lines) and the reference detour and WA method (dashed lines) for different levels of predefined relative error for G_A^{xx} for the structure of Section 6.5.2. 93
6.9 Spatial domain G_A^{xx} for the structure of Section 6.5.2. The contribution of the surface wave pole is also indicated. 94
6.10 Computational time for the Sommerfeld integral of (6.45) using the detoured integration and the WA algorithm for the reference method and the DE and WA algorithms in the proposed method. 96
6.11 Spatial domain G_{EJ}^{zz} for the structure of Section 6.5.3. 97

7.1 Real part of the potential integral (7.2) for a triangle with vertices $\mathbf{r_1} = [0, 0, 0]$, $\mathbf{r_2} = [0.1, 0, 0]$, $\mathbf{r_3} = [0, 0.1, 0]$ and for $\lambda = 1[m]$. The basis function $\mathbf{f}_Q(\mathbf{r}')$ is taken as constant over the source domain E_Q. 101
7.2 2-D quadrature rules based on Cartesian products. 103
7.3 Sampling points of (7.3) using 2D Cartesian product rules of GL, original DE and modified DE quadratures (from right to left). 104
7.4 Real part of (7.3) using Cartesian product rules of DE and GL quadratures and employing [82] up to numerically exact results for the inner quadrature (7.2). The integration domains E_P and E_Q coincide with the triangle shown in Fig. 7.1. 105
7.5 Modified DE transformation (7.4) and its accompanying derivative (7.5) for different values of the parameter α. 106
7.6 Distribution of integration points over the reference domain $[-1, 1]$ for the modified DE rule for different values of the parameter α. For comparison purposed, the abscissas of a GL rule with the same number of integration points as the DE rule with $\alpha = 0.5\pi$ is also shown. 107

7.7 Number of correct digits of the real part of the self term of (7.3) for a triangle with vertices $\mathbf{r_1} = [0, 0, 0]$, $\mathbf{r_2} = [0.1, 0, 0]$, $\mathbf{r_3} = [0, 0.1, 0]$ and for $\lambda = 1[m]$. 108

7.8 Number of correct digits of the self term of (7.3) for a triangle with vertices $\mathbf{r_1} = [0, 0, 0]$, $\mathbf{r_2} = [0.1, 0, 0]$, $\mathbf{r_3} = [-0.05, 0.087, 0]$ and for $\lambda = 1[m]$. 109

7.9 Number of correct digits of the edge adjacent case of (7.3) for triangles with vertices $\mathbf{r_1} = [0, 0, 0]$, $\mathbf{r_2} = [0.1, 0, 0]$, $\mathbf{r_3} = [-0.05, 0.087, 0]$ and $\mathbf{r_1} = [0, 0, 0]$, $\mathbf{r_2} = [0.1, 0, 0]$, $\mathbf{r_3} = [-0.05, -0.087, 0]$ for $\lambda = 1[m]$. 110

7.10 Number of correct digits of the edge adjacent case of (7.3) for triangles with vertices $\mathbf{r_1} = [0, 0, 0]$, $\mathbf{r_2} = [0.1, 0, 0]$, $\mathbf{r_3} = [-0.05, 0.087, 0]$ and $\mathbf{r_1} = [0, 0, 0]$, $\mathbf{r_2} = [0.1, 0, 0]$, $\mathbf{r_3} = [0, -0.1, 0]$ for $\lambda = 1[m]$. Linear basis and test functions are considered, i.e. $\mathbf{f}_P = \zeta'_{r2}$ and $\mathbf{f}_Q = \zeta_{r2}\hat{u}$, $\zeta_{r2}\hat{u}$ being the associated barycentric coordinate to the vertex $\mathbf{r_2} = [0.1, 0, 0]$. 111

List of Tables

4.1 Transformations between the spectral and the spatial domain for various expressions of $\tilde{G}$. $\tilde{A}$ is assumed to have radial symmetry, i.e. dependency only on k_ρ and not on k_x or k_y. The generalized Sommerfeld integral S_n is defined in (4.14). 20
4.2 Free space spectral domain GFs of an electric current $\mathbf{J}$. 23
4.3 Free space spectral domain GFs of a magnetic current $\mathbf{M}$. 23
4.4 Continuity properties of the mixed potentials as the observer crossed an interface. 39
4.5 Closed-form expressions of $\tilde{G}_A^{xx}$ for a conductive sheet separating two semi-infinite media. 42
4.6 Closed-form expressions of $\tilde{G}_A^{zx}$ for a conductive sheet separating two semi-infinite media. 43
4.7 Closed-form expressions of $\tilde{G}_A^{zz}$ for a conductive sheet separating two semi-infinite media. 44
4.8 Closed-form expressions of $\tilde{G}_V^{x}$ for a conductive sheet separating two semi-infinite media. 45
4.9 Closed-form expressions of $\tilde{G}_V^{z}$ for a conductive sheet separating two semi-infinite media. 46
4.10 Closed-form expressions of $\tilde{G}_A^{xx}$ for a conductive sheet separating two semi-infinite media with tensorial conductivity $\bar{\bar{\sigma}}$. 47
4.11 Closed-form expressions of $\tilde{G}_V^{z}$ for a conductive sheet separating two semi-infinite media with tensorial conductivity $\bar{\bar{\sigma}}$. 48
4.12 Contribution of TM and TE poles in multilayered structures with embedded sheets of scalar or tensorial conductivity. 50

5.1 Number of integration points N for the level M of the DE rule where the discretization step is h. These values are valid for double precision arithmetic units. 70
5.2 Possible transformation functions and their properties. 74

7.1 Number of integration points N for the level M of the proposed DE rule (7.4) where the discretization step is h. These values are valid for double precision arithmetic units and they serve as an extension of the Table 5.1 for the original DE rule. 107

Ioannis Koufogiannis

Contact Details
✉ ioannis.koufogiannis@epfl.ch
ioannis.koufogiannis@gmail.com

Date and Place of Birth
03.07.1986, Thessaloniki, Greece

EDUCATION

Ecole Polytechnique Fédérale de Lausanne (EPFL) 11.2009 - 01.2014
DOCTORATE (PH.D) Lausanne, Switzerland

Doctoral School of Electrical Engineering
Laboratory of Electromagnetics and Acoustics (LEMA)
THESIS TITLE: The Mixed Potential Integral Equation for New Multilayered Structures Including Conductive Sheets: Analytical and Numerical Techniques

Aristotle University of Thessaloniki (AUTH) 09.2004 - 07.2009
DIPLOMA (DIPL.-ING.) Thessaloniki, Greece

Department of Electrical and Computer Engineering, Faculty of Engineering
THESIS TITLE: Study of a radio interferometer with infinite and finite focusing capabilities
GPA: 9.33/10.0 - 2nd in graduation rank out of 345 students (top 1%)

PROFESSIONAL EXPERIENCE

Ecole Polytechnique Fédérale de Lausanne (EPFL) Phase 1: 11.2009 - 07.2012
Phase 2: 08.2012 - 08.2013
TECHNICAL RESEARCHER Lausanne, Switzerland

PROJECT: Lightweight RF Power Cable with High Phase Stability (22589/09/NL/GLC)
OBJECTIVE: Design, manufacture and test of a new generation of ultra-light RF cables for aerospace applications with excellent phase stability and a 30% to 40% reduction in overall weight compared to currently available cables
FOUNDED BY: European Space Agency (ESA)
PARTNERS: Huber+Suhner AG, LEMA EPFL, IMES ETHZ
Scientific responsible for:

- WP1021 RF low power and EMC analysis
- WP1022 Phase stability analysis
- WP1023 Thermal analysis
- WP1025 High power corona breakdown analysis

Ecole Polytechnique Fédérale de Lausanne (EPFL) 09.2010 - 08.2012
TECHNICAL RESEARCHER Lausanne, Switzerland

PROJECT: POSEIDON (CTI 11568.1 PFIW-IW)
OBJECTIVE: The SEMCAD simulation platform is enhanced with next generation algorithms to allow the analysis, synthesis and optimization of the new micro- and millimeterwave used in aerospace, wireless communications and health care industries
FOUNDED BY: Swiss Commission for Technology and Innovation (CTI)
PARTNERS: SPEAG AG, LEMA EPFL, IT'IS foundation ETHZ
Scientific responsible for:

- WP110 FEM solver with straight elements
- WP120 FEM solver with curvilinear elements
- WP130 Connection to Integral Equation tecnhique

Akebono Brake Industry Co., Ltd. 08.2008 - 10.2008
INTERN Hanyu City, Saitama, Japan

PROJECT: AiSYS Project within ITIO Department
OBJECTIVE: Examination of current industry trends towards the IPPhone and its development within Akebono Brake Industry Co., Ltd.
ADDITIONAL ACTIVITIES:

- Certification for Akebono Production System (APS) with grade ”Excellent”
- Certification on Japanese Business Manners

Technical University of Łodz 07.2007 - 09.2007
INTERN Łodz, Poland

Computer Engineering Department
PROJECT: Implementation of a C++ Software for Designing Digital Filters

ACADEMIC EXPERIENCE

Teaching Assistant

- Electromagnetics I (SEL-EPFL) 2011-2013
- Electromagnetics II (SEL-EPFL) 2011-2013
- Antennas and Radiation (SEL-EPFL) 2010-2011

Students Projects Supervisor

- Integration Techniques with CUDA Spring 2012
- Modeling of Corona Discharges in Satellite Systems Spring 2013
- Parallelizing a VIE Method using CUDA Spring 2013

AWARDS AND DISTINCTIONS

Distinctions

Greek State Scholarship Foundation's Award due to top university notes 2004-2008

35th International Physics Olympiad (IPhO), Pohang, Korea 07.2004
Member of the Greek team

National Physics Olympiad, Athens, Greece 2003-2004
3rd prize

National Chemistry Olympiad, Athens, Greece 2003-2004
2nd praise

17th – 20th National Mathematical Olympiads (Archimedes), Athens, Greece 1999-2003
Ranked among best 50 students (No 17 in 2000-2001)

Awarded Invitations

EADS @Paris AirShow, Le Bourget, France 06.2009
Workshop on Defence & Security: ”System engineering in UAV (drone) systems and Fighter A/C system”

PUBLICATIONS

Refereed Journal Papers

1. **I. Koufogiannis**, E. Sorolla, and M. Mattes, "Microwave gas breakdown in elliptical waveguides," *Physics of Plasmas (1994-present)*, vol. 21, no. 1, 2014.
2. A.G. Polimeridis, **I. Koufogiannis**, M. Mattes and J.R. Mosig, "Considerations on double exponential-based cubatures for the computation of weakly singular galerkin inner products," *Antennas and Propagation, IEEE Transactions on*, vol. 60, no. 5, pp. 2579–2582, 2012.

Refereed Conference Papers

1. **I. Koufogiannis**, M. Mattes and J.R. Mosig, "On the development and evaluation of spatial domain Green Functions for multilayered structures with conductive sheets," in *Numerical Electromagnetic Modeling and Optimization for RF, Microwave and Terahertz Applications (NEMO), 2014 IEEE International Conference on*, Submitted.
2. **I. Koufogiannis**, M. Mattes and J.R. Mosig, "Mixed potentials for planar multilayered structures including conductive interfaces," in *Antennas and Propagation (EuCAP), 2014 8th European Conference on*, Accepted.
3. **I. Koufogiannis**, A.G. Polimeridis, J.S. Gomez-Diaz, M. Mattes and J.R. Mosig, "Dyadic Greens functions of a graphene layer and their efficient calculation," in *Antennas and Propagation Society International Symposium (APSURSI), IEEE*, pp. 1–4, 2013.
4. **I. Koufogiannis**, A.G. Polimeridis, M. Mattes and J.R. Mosig, "On the numerical evaluation of Green functions for structures with graphene layers," in *IX Iberian Meeting on Computational Electromagnetics (EIEC)*, Denia, Spain, 2013.
5. **I. Koufogiannis**, E. Sorolla, J.R. Mosig and M. Mattes, "Analyzing corona breakdown with a finite element-based electromagnetic solver," in *Antennas and Propagation (EuCAP), Proceedings of the 7th European Conference on*, pp. 2312–2314, 2013.
6. **I. Koufogiannis**, A.G. Polimeridis, M. Mattes and J.R. Mosig, "Real axis integration of Sommerfeld integrals with error estimation," in *Antennas and Propagation (EUCAP), Proceedings of the 6th European Conference on*, pp. 719 –723, 2012.
7. E. Sorolla, **I. Koufogiannis** and M. Mattes, "Corona breakdown in open structures: A comparison of several ionization rate models," in *Antennas and Propagation (EUCAP), 6th European Conference on*, pp. 1227 –1230, 2012.
8. **I. Koufogiannis**, A.G. Polimeridis, M. Mattes and J.R. Mosig, "A parametric study of the Double Exponential algorithm utilized in weakly singular integrals," in *Antennas and Propagation (EUCAP), Proceedings of the 5th European Conference on*, pp. 2147 –2151, 2011.
9. **I. Koufogiannis**, A.G. Polimeridis, M. Mattes and J.R. Mosig, "Optimized machine precision double exponential quadratures applicable in weakly singular integrals," in *VIII Iberian Meeting on Computational Electromagnetics (EIEC)*, Sesimbra, Portugal, 2011.

Workshop Presentations

1. H. Karstensen, **I. Koufogiannis**, E. Sorolla, G. Kress, M. Mattes, M. Rupflin, J. Fuchs and K. Wettstein, "Phase stable RF-cable for space applications," in *Space Passive Component Days, 1st International Symposium*, ESA/ESTEC, Noordwijk, The Netherlands, 2013.
2. **I. Koufogiannis**, A.G. Polimeridis, M. Mattes and J.R. Mosig "Greens functions for multilayered structures including conductive interfaces and graphene sheets: development and novel numerical evaluation," in *COST IC1102 'VISTA', 4^{th} WG Meeting & Technical Workshop*, Thessaloniki, Greece, 2013.
3. **I. Koufogiannis**, A.G. Polimeridis, M. Mattes and J.R. Mosig, "A parametric study of the Double Exponential algorithm utilized in weakly singular integrals," in *COST IC0803 'RFCSET', 6^{th} WG Meeting & Technical Workshop*, Perugia, Italy, 2011.
4. E. Sorolla, **I. Koufogiannis** and M. Mattes, "Ionization rates: a comparative study to predict corona breakdown," in *International Workshop on Multipactor, Corona and Passive Intermodulation (MULCOPIM) '11*, Valencia, Spain, 2011.

5. A.G. Polimeridis, **I. Koufogiannis**, M. Mattes and J.R. Mosig, “Efficient Double Exponential based cubatures for the computation of weakly singular Galerkin inner products,” in *IV Workshop on Integral Techniques for Electromagnetics (INTELECT)*, Les Diablerets, Switzerland, 2010.